Self-Assembled Single Stranded DNA-Amphiphiles for Targeted Drug Delivery

A Thesis
SUBMITTED TO THE FACULTY OF THE
UNIVERSITY OF MINNESOTA
BY

Michael Harris

IN PARTIAL FULFILLMENT OF THE REQUIREMENTS
FOR THE DEGREE OF
DOCTOR OF PHILOSOPHY

Advised by: Efrosini Kokkoli

June 2018

Acknowledgements

My experience at the University of Minnesota has been both rewarding and challenging. Over the last five years I have grown as both a researcher and person. I must acknowledge the enormous contribution made by my advisor, Efie, who has brought constant support, motivation, and guidance to my research. Thank you for making me a better researcher and teaching me how to sell a story. During my research, I used several University of Minnesota resources including the Characterization Facility, the Histology and Research Laboratory, the University Imaging Centers, the University Flow Cytometry Resource, and I received help from the University Informatics Institute. I would like to thank each of the individuals who provided training, technical expertise, and scientific analysis from each of those resources.

It has been a pleasure working with, learning from, teaching, and enjoying my time with the Kokkoli group members of the last five years. I would specifically like to acknowledge Tim, Rachel, Carolyn, Frankie, Abby, Huihui, Jun, and Tugba for their stimulating scientific ideas and the enjoyable conversations we have shared. I could not have completed this research without the help I received from other groups in the department and I would like to thank the Hu lab, Azarin lab, and Hackel lab for their support and use of their equipment. Finally, I would like to thank my friends and family for their support throughout the good and bad of graduate school and especially my wife Beth, for her unwavering love and commitment through the entirety of my graduate research.

For my Wife and Son, to whom I give all my love.

Abstract

The use of targeted drug delivery has significantly improved the field of medicine in the last 30 years. At the same time, the field of DNA nanotechnology has allowed for the design nanoparticles with exact nanoscale precision. This thesis combines the two fields by using single-stranded DNA amphiphiles, a novel class of biomaterials, to create new targeted drug delivery vehicles.

DNA aptamers are a sub-class of single stranded DNA molecules whose three-dimensional structure allows them to bind to one molecule with high affinity. ssDNA-amphiphile micelles were created from a ssDNA aptamer sequence to create a targeted ssDNA micelle for cancer therapies. These targeted micelles were shown to internalize only to cells expressing the aptamer target and release into the cytosol over 24 h. *In vivo* studies showed that although tumor accumulation of ssDNA-amphiphile micelles is independent of their targeting capability, internalization of the micelles requires the aptamer sequence.

DNA-amphiphiles have also been shown to form nanotubes when in aqueous solution, dependent on the exact DNA sequence and lipid tail structure used. One ssDNA-amphiphile that forms nanotubes was used for delivery to mouse glioblastoma cells. The nanotubes were shown to internalize to the glioblastoma cells, but not to healthy mouse astrocytes. When delivered directly to both hemispheres of the brains of mice with tumors in the right hemisphere, retention was observed only in the tumor hemisphere and not in the healthy hemisphere. This observation was conserved when the nanotubes were delivered systemically.

The nanotubes were then used for an initial *in vitro* chemotherapy experiment. When mixed with the chemotherapeutic doxorubicin, the nanotubes released little chemotherapeutic over the course of two weeks, with no significant change in the nanotube structure over this time. When delivered to mouse glioblastoma cells, the doxorubicin – nanotube mixture showed better cell toxicity compared to free doxorubicin. This is a promising result for chemotherapeutic delivery of the nanotubes.

Contents

List of Tables

List of Figures

1 Introduction

The evolution of nanotechnology in the field of medicine has contributed greatly to the improved survivability and quality of life for many types of disease. Over the past thirty years, this field of medicine has grown extensively, with an industry estimated worth in 2016 of 138.8 Billion USD and an estimated to worth of over 350 Billion USD by 2025.[1] The field of nanomedicine is centered around improving the efficacy of delivered drugs. This can be done by improving the percentage of drug that reaches certain regions of interest or by increasing the overall lifetime of the drug in the body.

Improvements in nanotechnology have led to the introduction of targeted drug delivery therapies, whereby unique regions of the body, such as tumors, can be specifically targeted based on the characteristics of the drug delivery vehicle. This increases the amount of drug delivered to the region of interest, while decreasing delivery to unintended regions. The enhanced permeability and retention (EPR) effect is a characteristic of many tumors that passively leads to higher accumulation of nanoparticles in tumors compared to healthy tissue.[2] Active targeting can also be used by incorporating specific molecules into the drug delivery vehicle that bind to target molecules expressed only in the region of interest. This is commonly achieved by the incorporation of antibodies, using ligands for specific receptors, using pH-responsive materials, or using aptamers.[3-5] The introduction of poly(ethylene glycol) (PEG) coatings in nanomedicine helped to significantly increase the circulation lifetime of liposomes, a self-assembled nanoparticle that can act as a drug carrier.[6] These liposomes have come to be termed “stealth liposomes”, as they increase circulation lifetime by evading clearance by the body’s immune system. This approach has

been used by chemotherapeutics such as Doxil, a PEGylated liposomal form of doxorubicin, to increase the circulation time of the drug.[7]

This thesis discusses the use of nanostructures composed of self-assembled single-stranded DNA (ssDNA)-amphiphiles and their use in targeted drug delivery applications. The use and characterization of ssDNA-amphiphiles is relatively new, but these molecules hold significant promise in the field of nanomedicine. In order to understand how ssDNA-amphiphiles can be used in the field of nanomedicine, it is first important to understand amphiphilic molecules and their self-assembled structures, how nanoparticles in general can be targeted to certain regions of interest, such as cancer, and what types of therapeutic molecules are commonly delivered. This chapter will cover each of these topics while the remaining chapters of this thesis will discuss how ssDNA amphiphiles can be utilized as targeted delivery vehicles.

1.1 Amphiphiles

1.1.1 Amphiphile Structure

The word amphiphile comes from the Greek *amphi*, meaning both, and *philia*, meaning love, together describing molecules that interact well with both water-based and oil-based solvents. Amphiphiles generally consist of a hydrophilic (water-loving) and lipophilic (fat-loving) or hydrophobic (water-hating) portion as shown in Figure 1.1.

Commonly, these regions of an amphiphile are referred to as the “headgroup”, for the hydrophilic region, and the “tail”, for the hydrophobic region, as many common amphiphile structures consist of a tail-like hydrocarbon chain and a bulky, sometimes

charged hydrophilic region that can be taken as a sphere. The unique structural characteristic of amphiphiles, molecules composed of both hydrophilic and hydrophobic regions, allows them to interact with each other and aggregate into larger, more complex structures. This process is driven by a complex set of interactions between the amphiphile molecules interacting with themselves and interacting with the surrounding solvents. The remainder of this thesis will only consider aqueous solutions for amphiphilic interactions, but the general forces that drive amphiphilic self-assembly can be interpreted for any type of solvent.

Figure 1.1 Basic structure of an amphiphile, with the hydrophilic (water-loving) circular headgroup, and the hydrophobic (water-hating) tail.

1.1.2 Driving Force for Self-Assembly and Packing Considerations

The driving force for self-assembly of amphiphiles can be broken down into two main parts: interactions between the amphiphile and the solvent, and interactions between the amphiphile and other amphiphiles. The overall combination of these forces influences the size and shape of the resulting self-assembled structure; therefore, changing the strength of each of these interactions is essentially the same as controlling what types of structures each amphiphile will form.

The classical force driving the self-assembly of amphiphilic molecules is known as the "hydrophobic effect". This interaction is driven by the hydrophobic regions of the amphiphile aggregating together to minimize contact with the solvent. Despite this seemingly simple attractive description of what appears to occur, this aggregation is actually the result of interactions between the amphiphile and the solvent molecules.[8-10] If the hydrophobic region of the amphiphile is exposed to water, the surrounding water molecules have very low entropy, as they are forced into a specific conformation to solvate the tail. However, as the hydrophobic tails aggregate together, the water molecules are no longer trapped in a specific conformation, as there are no exposed tails to solvate. This leads to an overall increase in entropy of the system, which makes the aggregated amphiphile state the lowest energy state of the system.

Interactions between individual amphiphiles include Van der Waals interactions, which describe the interactions between the electron clouds of atoms. These interactions can be attractive or repulsive in nature, and are often strong relative to other intermolecular forces.[11] Electrostatic forces, commonly associated with the headgroup of the amphiphile, can directly affect self-assembly. Although these forces are typically repulsive, as individual amphiphiles of the same type will have the same charge on their headgroup, combining two different amphiphiles with oppositely charged headgroups can lead to attractive interactions.[12] The strength of electrostatic interactions can be changed by adjusting environmental parameters such as the type of solvent, the pH of the solution, and the amount of dissolved electrolyte in solution.[8, 13-17] Additionally, hydrogen bonds can

allow for significant interactions between amphiphile molecules, allowing for drastic changes in the types of self-assembled structures that are formed.[18, 19]

The analysis of self-assembled structures formed from amphiphilic aggregation was pioneered in the 1970's by Tanford and Isrealachvili. Tanford developed a mathematical formulation describing amphiphilic self-assembly based on the sum of two forces: repulsive forces between amphiphiles based on electrostatic and steric repulsion, and attractive forces dominated by the hydrophobic force.[9, 10] From this analysis, Israelachvili developed the concept of the packing parameter of an amphiphile, a single parameter which is able to describe the self-assembled structure of a wide variety of amphiphiles.[11]

The packing parameter considers three geometric parameters of the amphiphile to describe the shape of the amphiphile, and thereby the shape of the self-assembled structure when the amphiphile is close-packed in 3-dimensional space. The first parameter is the occupied surface area of a single amphiphile's headgroup on the superstructure surface, called the optimal headgroup area, a_o. The second parameter is the volume occupied by the tail of a single amphiphile, v. The third parameter is the length of the amphiphile's hydrophobic tail, l_c. The packing parameter, P, is then defined as $v/(a_o \cdot l_c)$. Another interpretation of this dimensionless parameter is the ratio of the effective area of the hydrophobic tail, as represented by v/l_c, and the optimal headgroup area, a_o. For simple amphiphiles, the value of the packing parameter defines the types of self-assembled structures that are formed, as shown by the cartoon in Figure 1.2.

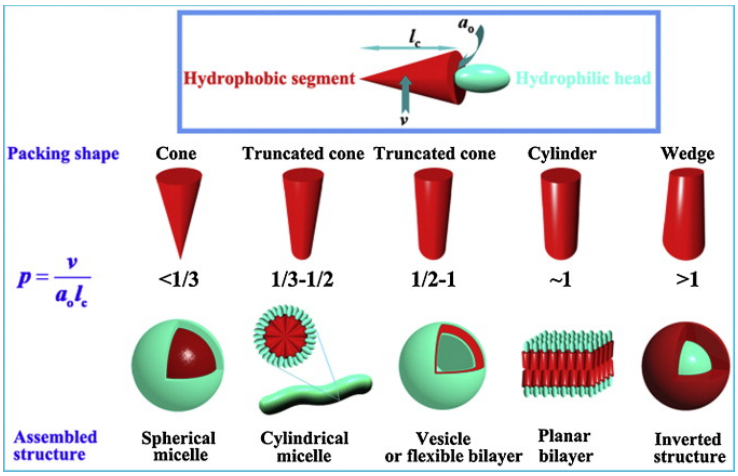

Figure 1.2 A cartoon representation of the shape of different amphiphiles, the packing parameter associated with each shape, and the types of self-assembled structures those amphiphiles form. Reprinted with Permission from Zhang *et al.*[20]

For values of the packing parameter less than 1/3, spherical micelles are formed; for values between 1/3 and 1/2, cylindrical micelles are formed; for values between 1/2 and 1, liposomes or vesicles are formed; for values approximately equal to 1, bilayers are formed. The basis for Israelachvili's analysis was Tanford's model of the energetic contributions driving self-assembly of the amphiphiles. Notably, Tanford created two simple linear equations that would describe the length of a fully extended hydrocarbon chain and the volume of that chain. When the length of the chain is greater than approximately eight carbons, the ratio of v/l_c was approximately constant.[10] Therefore, from Israelachvili's analysis, the dominating factor that controls the packing parameter for this analysis is the optimal headgroup area, a_o.

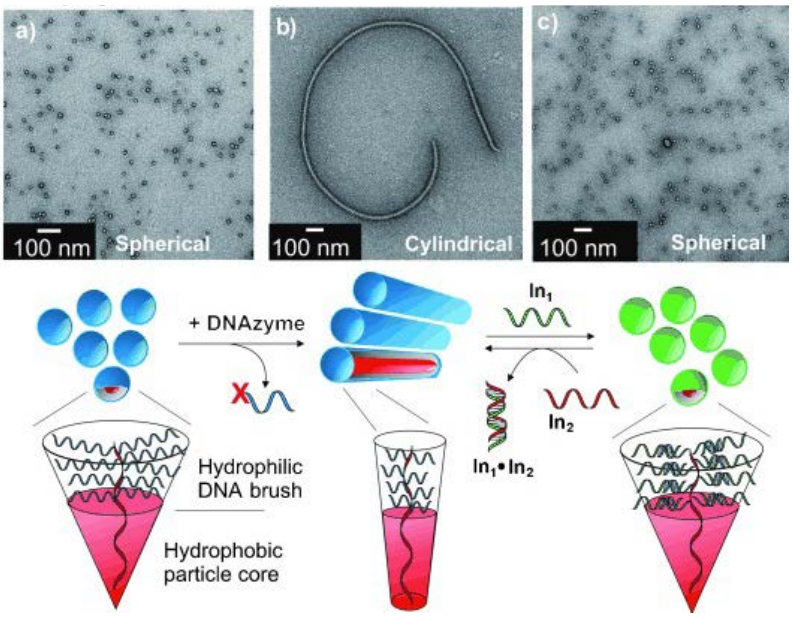

Figure 1.3 Schematic showing the change in self-assembled structure based on the size of the amphiphilic headgroup, as visualized by cryogenic transmission electron microscopy. Reprinted with permission from Chien *et al.*[21]

A well-defined example of the role of the packing parameter and the effect of the optimal headgroup area can be seen in Figure 1.3.[21] In the work by Chien *et al.*, amphiphiles were formed from a hydrophobic tail coupled to a DNA brush layer. This created a large headgroup area that led to the assembly of spherical micelles. Through the addition of enzymes that degrade the DNA, the headgroup area was reduced. This changed the packing parameter and allowed for the assembly of cylindrical micelles. Upon the addition of a complementary DNA sequence (ln_1) that bound to the DNA headgroup, the headgroup area increased, thereby reforming the spherical micelles expected for a small packing parameter. This could then be reversed back to the cylindrical micelles by removing the complementary DNA sequence (ln_1) through the addition of a competing DNA sequence (ln_2). Thus, the packing parameter analysis proposed by Israelachvili is a powerful tool in predicting aggregated amphiphile structures.

1.1.3 ssDNA-Amphiphile Self-Assembled Structures

Much of the amphiphile literature focuses on the use of small molecule headgroups or oligopeptide headgroups. The Kokkoli research group has previously developed single-stranded DNA (ssDNA)-amphiphiles that are composed of three main building blocks. The hydrophilic headgroup is composed of a ssDNA molecule instead of the typical small molecule or peptide. This ssDNA molecule can have any sequence of nucleotides and is usually between 10 and 40 nucleotides in length. The hydrophobic tail of the amphiphile is typically composed of two hydrocarbon chains. The third optional component of the amphiphile is a spacer region that acts to separate the ssDNA headgroup from the hydrophobic tail. The chemical nature of this spacer component can be changed as desired to increase the effective size of the hydrophilic headgroup or hydrophobic tail.

Based on the packing parameter analysis for amphiphiles, it would be expected that these ssDNA-amphiphiles should form only spherical micelles, as they are composed of a bulky hydrophilic ssDNA headgroup that typically weighs between 4 and 15 kDa and they only have a small hydrocarbon tail that typically weighs less than 1 kDa. Indeed, cryogenic transmission electron microscopy (cryo-TEM) imaging shows that micelles are commonly formed from ssDNA-amphiphiles in aqueous solutions.[22-24] However, it was also observed that some ssDNA-amphiphiles formed flat nanotapes, twisted nanotapes, helical nanotapes, and nanotubes,[22-24] with the growth of nanotubes progressing through each of these structures over time.[24]

This alone is a surprising result, as the packing parameter analysis developed from Tanford and Israelachvili's formulations suggest that these types of structures should not be observed. From the packing parameter analysis, the effective area of the hydrophilic headgroup should be the dominating parameter that controls the self-assembled structures that are formed. However, the definition of the headgroup area as the physical size of the headgroup leads to an incomplete analysis of the packing parameter, as this definition ignores thermodynamic considerations such as temperature, salt concentrations, pH, and intermolecular interactions. All of these thermodynamic considerations can affect the packing dynamics of the amphiphiles. It has been shown in the literature that headgroup interactions that are not accounted for by the packing parameter analysis can lead to self-assembled structure that otherwise would not be predicted.[18, 19] While interactions between amphiphilic headgroups should not be ignored, numerical analysis in the literature has also shown that the role of the hydrophobic tail should not be ignored as it is in Israelachvili's analysis.[25] Together, this indicates that the packing parameter can be used as a guide for what types of structures are likely to form, but correct conclusions can only be drawn from experimental observation. Indeed, the nanotape and nanotube structures observed by ssDNA-amphiphiles in the Kokkoli group are not unique to the literature, as these structures have been seen extensively in the peptide-amphiphile literature.[26-31] However, to our knowledge, these are the first such structures observed from ssDNA-amphiphiles.

1.1.4 Headgroup and Spacer Effects on Structure

Previous work in the Kokkoli group has shown that both the sequence of the ssDNA headgroup and the type of spacer used between the headgroup and tail have an effect on

the self-assembled structures observed. A common secondary structure observed in the ssDNA headgroup of these amphiphiles is a g-quadruplex. G-quadruplexes are formed from guanine-rich sequences of DNA through the stacking of three or more g-tetrads, where four guanines interact through hydrogen bonds in a circular fashion. The canonical Watson-Crick face of a guanine is capable of hydrogen bonding with the Hoogsteen face of an adjacent guanine. A schematic of this interaction is shown in Figure 1.4. Work done by the Kokkoli group has demonstrated that the presence of g-quadruplexes in the ssDNA headgroup of ssDNA-amphiphiles is beneficial for the formation of the nanotape and nanotube structures, however they are not necessary for nanotape or nanotube formation.[22-24] Additionally, the use of a hydrocarbon chain as a spacer between the ssDNA headgroup and the dialkyl tail helps to promote nanotube development.[22-24]

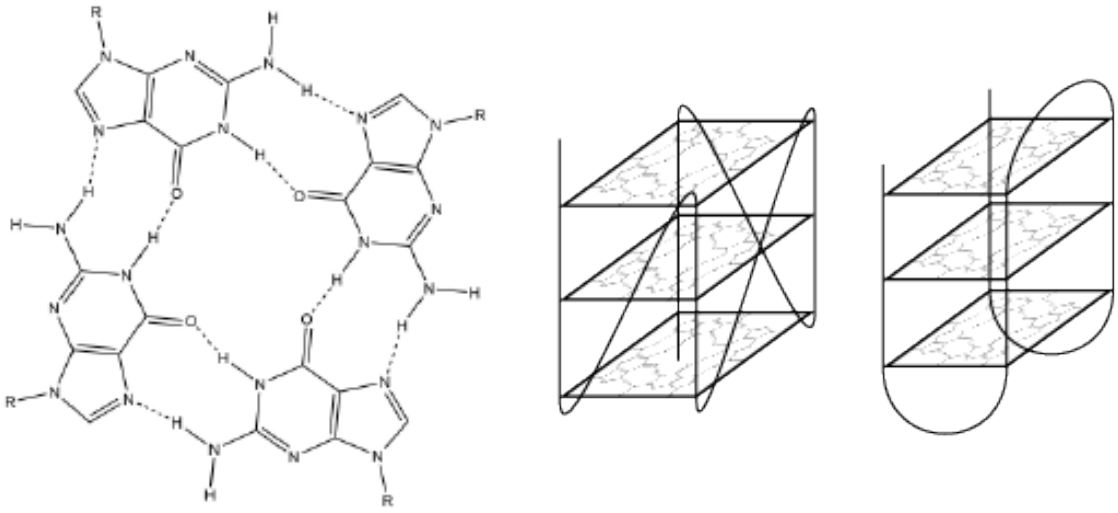

Figure 1.4 Left is a schematic of a g-tetrad, with hydrogen bonds between the Watson-Crick and Hoogsteen faces of adjacent guanines. Middle is an intramolecular parallel g-quadruplex. Right is an intramolecular anti-parallel g-quadruplex.

G-quadruplexes have been shown to form from a single DNA strand that folds upon itself (as depicted in Figure 1.5), two DNA strands that interact together, or four individual DNA strands.[32-35] G-quadruplexes can also be classified as parallel or anti-parallel based on the direction of the DNA strands that form the quadruplex. The differences between parallel and anti-parallel g-quadruplexes can be determined by the Circular Dichroism spectra of the molecule, where parallel structures have a strong positive peak between 258 and 265 nm, and anti-parallel structures have a negative peak at 260 nm and a positive peak at 290 nm.[36, 37] This allows for the identification and characterization of g-quadruplexes formed from new, unique DNA sequences.

1.2 Cancer Targeting

Cancer is a unique tissue in the body as it is considered a disease, but is entirely made from the body's own cells. Cancer is believed to have six to eight hallmark characteristics: "sustaining proliferative signaling, evading growth suppressors, resisting cell death, enabling replicative immortality, inducing angiogenesis, and activating invasion and metastasis,"[38, 39] as well as "the reprogramming of energy metabolism, and evading the immune system."[39] Researchers have developed ideas and methods for targeting and killing cancer based on the framework of these hallmarks. Cancer targeting can be achieved through passive targeting and through active targeting. Passive targeting is commonly defined as delivery of the therapeutic agent to the tumor based entirely on the therapeutic physical characteristics and the environmental physical characteristics, with no specific interactions occurring between the delivered agent and its target.[40] Active targeting is

commonly defined as delivery of the therapeutic agent to the tumor based on the attachment of specific ligands to the tumor tissue.[40]

1.2.1 Passive Targeting and the Enhanced Permeation and Retention Effect

Passive targeting of therapeutics to tumors is often described through the enhanced permeation and retention (EPR) effect. The EPR effect is the explanation for the observation that nanoparticles and macromolecules of a specific size tend to accumulate in tumor tissues more than healthy tissues when delivered systemically.[2, 41, 42] One of the hallmarks of cancer is the induction of angiogenesis, whereby fast-growing tumor tissue needs access to many blood vessels to receive the nutrients to sustain rapid growth. During this growth, new blood vessels are often irregular in structure, which often leads to porous vessel walls compared to those found in healthy tissues. This porous structure allows nanoparticles and macromolecules to extravasate from the blood vessels and accumulate in the tumor tissue.

Though the EPR effect can improve the delivery of therapeutic nanoparticles to the tumor tissue, there is a counterbalancing force that prevents accumulation: the clearance of nanoparticles from the bloodstream by the reticuloendothelial system (RES). It has been shown that the overall success of a passively-targeted therapeutic nanoparticle is directly related to its blood circulation lifetime.[43] As the nanoparticle increases its circulation lifetime, there is a higher chance of passing through blood vessels adjacent to the tumor, which would allow for accumulation into the tumor via the EPR effect. Therefore, increasing the circulation lifetime of a drug will directly increase its efficacy when

passively targeted. The most common method of increasing circulation lifetime of a nanoparticle is by adding poly(ethylene glycol) (PEG) to the exterior.[6, 44-46] The addition of a PEG outer layer helps to create steric repulsion between the nanoparticle and the macrophages that would act to clear the nanoparticles from the bloodstream. The use of nanoparticles that fall within the specific size range of 10 nm and 100 nm leads to the best overall utilization of the EPR effect,[47-51] as clearance by the kidney occurs for nanoparticles smaller than 10 nm[51, 52] and clearance by the liver occurs for nanoparticles larger than 100 nm.[51]

1.2.2 Direct Targeting

Direct targeting of tumors involves the incorporation or direct use of ligands that are specific to molecules expressed by the tumor tissue. Many ligands used in tumor targeting are specific to molecules associated with one of the hallmarks of cancer. For example, vascular endothelial growth factor (VEGF) is an excreted protein that induces the formation of new blood vessels.[53-55] As tumors are constantly creating new blood vessels to sustain their fast growth rate, VEGF is widely expressed in the tumor tissue. The benefit of targeting a protein involved in the hallmarks of cancer, such as VEGF, is that the protein is likely to be present in the tumor tissue, allowing for binding of the nanoparticle.[56, 57] However, a more general goal is to target molecules that are expressed in much higher amounts in the tumor tissue as compared to the healthy tissue, with the ultimate goal of finding molecular targets that are expressed only in the tumor tissue. Doing so would help to prevent off-targeting that can lead to side effects when delivering toxic therapeutics designed to kill tumor tissue. As an example of potential healthy tissue off-targeting, VEGF

is also known to be expressed in embryonic tissues or areas of the body that require new blood vessels after injury.[53] Therefore, the use of VEGF-targeting therapeutics has led to some adverse effects when used as a cancer targeting therapy.[58]

Several classes of ligands have been utilized to target tumors in the literature. Antibodies are the only class of macromolecules that are currently approved by the FDA for targeted therapies in clinical use. Antibodies are the immune system's natural method of targeting specific molecules and antibodies are typically specific to one antigen. Due to the specificity offered by antibodies, several therapies have been developed utilizing antibodies over the last 15 years.[59-64] The basis for an antibody's specific binding is a short peptide sequence known as the complementarity determining region, and generally consists only of a few amino acids of the entire antibody structure. The three-dimensional conformation as well as the actual sequence of the amino acids is what determines the specificity of the antibody. Therefore, it is easy to imagine that specific binding can be observed for any short sequence oligopeptide sequence, even if the oligopeptide is not attached to the large carriers like the antibody heavy and light chains. Many small-molecule peptides have been developed that are specific to certain tumor targets,[65-67] and research is ongoing to utilize these small molecules as targeting moieties for therapeutic nanoparticles.

The specific binding to a target of interest due to chemical sequence and three-dimensional conformation is not a unique property of amino acids. DNA aptamers are nucleic acids that have the same binding properties as amino acids based on the chemical sequence, secondary structure, and tertiary structure. DNA aptamers are often selected through a

process known as the systematic evolution of ligands by exponential enrichment (SELEX), whereby a large library of unique oligonucleotide sequences is exposed to the desired target and enriched over many cycles to identify only the few sequences that bind strongly to the target.[68, 69] This process allows for the identification of DNA aptamers that are capable of binding to any desired target. The Kokkoli group has previously used this process to identify the FKN-S2 aptamer,[70] which targets the chemokine fractalkine.

1.2.3 Effect of Shape on Targeting

The effect of nanoparticle shape must be considered when designing targeted drug delivery vehicles. Spherical nanoparticles are often the most utilized nanoparticles as they are readily formed from a wide variety of materials and can be synthesized in many different sizes. Examples include spherical micelles from amphiphilic molecules, liposomes from amphiphilic molecules or natural origins such as vesicles, and metallic nanoparticles such as gold nanoparticles.

In an article written by Kolhar *et al.*, it was shown that antibody-coated rod-shaped nanoparticles are capable of internalizing to a much higher degree than spherical nanoparticles with the same antibody coating and of similar volume.[71] This effect was observed both *in vitro* in microfluidic devices simulating the vasculature, as well as *in vivo* when displaying antibodies targeted against the lung and the brain. The authors suggested that the high aspect ratio of the rod-shaped nanoparticles allowed a larger percentage of their surface area to come into contact with the target, thereby allowing a larger fraction of

the antibody coating to bind with the target. Additionally, shear alignment of elongated particles in fluid flow likely helps to ensure a large contact area with the vessel wall.

In addition to the increased binding available for high aspect ratio molecules, different types of cells have been shown to have different preferences for nanoparticle internalization.[72] Agarwal *et al*. demonstrated that after controlling for volume, charge, and material composition, mammalian cells preferentially internalize nanoparticles of different shapes. It was shown that epithelial cells and immune cells preferentially internalize disc-shaped nanoparticles as compared to rod-shaped nanoparticles. Additionally, the internalization pathways vary between cell types. An example of preferential internalization based on shape and cell type can be seen in Figure 1.5.

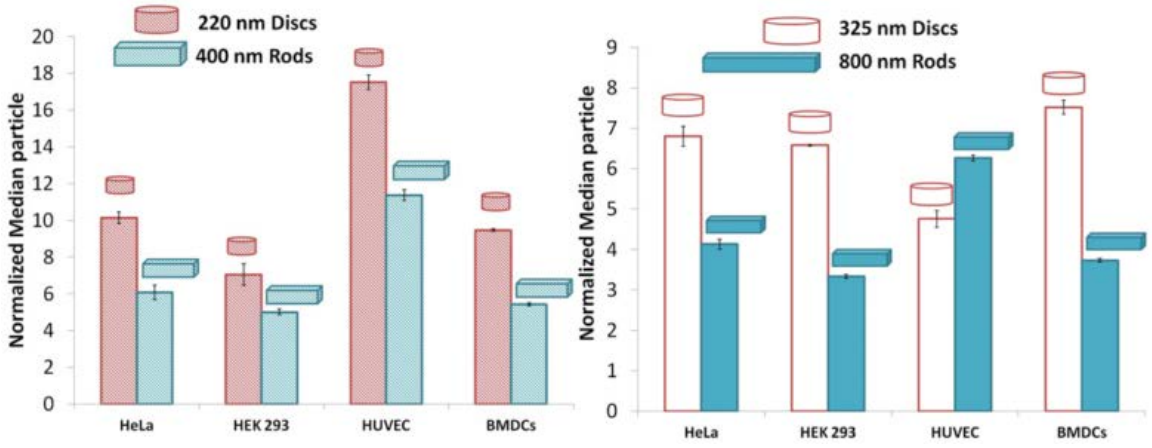

Figure 1.5. Differences in nanoparticle uptake as a function of cell type, nanoparticle size, and nanoparticle aspect ratio. Reprinted with permission from Agarwal *et al*.[72]

The authors proposed in this work that the shape-dependent internalization is dependent on the contact area between the nanoparticle and the cell, the energy required to deform the cell membrane, and the localized concentration of nanoparticles on the cell membrane.[72] It

is therefore difficult to predict how nanoparticles will interact with various cell types *a priori*, and experiments to evaluate cellular interaction and internalization should be performed for new types of nanoparticles.

1.3 Chemotherapeutics

1.3.1 Chemotherapeutic Methods of Action

The term "chemotherapeutic" has come to describe small molecule drugs that non-specifically internalize to cells and prevent mitosis. A general descriptor of cancer is that it reproduces uncontrollably; therefore, preventing mitosis is one of the most effective ways of stopping the spread of cancer cells. Many classes of chemotherapeutics exist that act to prevent mitosis.[73]

Alkylating agents were one of the first classes of chemotherapeutics to be used clinically,[74] and act by covalently binding to the DNA strand, which can lead to DNA strand breakage during DNA replication or transcription.[73, 75] Anthracyclines such as doxorubicin, daunorubicin, and their derivatives are some of the most commonly used and most effective chemotherapeutics.[76, 77] These molecules have a number of cytotoxic mechanisms, which include intercalation into nucleic DNA strands to prevent DNA replication, the generation of free radicals, and the inhibition of topoisomerase. Antimicrotubule agents, such as paclitaxel and docetaxel, act by inhibiting the function of microtubules during the cell division process.[78] Paclitaxel specifically stabilizes the microtubule, preventing its degradation during mitosis, eventually leading to cell death.

The common theme among all chemotherapeutics is that rapidly dividing cells are affected by the chemotherapeutic more than slowly dividing cells, as a smaller fraction of slowly dividing cells are undergoing mitosis while the chemotherapeutic is in blood circulation. However, healthy cells that divide quickly are indistinguishable from cancer cells during treatment, as the chemotherapeutics themselves are not targeted. This is the basis for many of the side effects observed after chemotherapy regimens. The death of fast-dividing cells, such as the bone marrow, the stomach lining, and hair follicles, lead to common chemotherapy side effects: weakened immune system, nausea and vomiting, and loss of hair, respectively. These are among the top-rated side effects in terms of severity, as reported by chemotherapy patients in the clinic.[79] It is therefore important to develop targeted delivery mechanisms to help alleviate the side effects associated with chemotherapeutic regimens.

A wide variety of chemotherapeutics have been developed for clinical use. Many chemotherapeutics are simple formulations of the small-molecule drugs that create the therapeutic effect. However, derivatives of these drugs are also utilized in the clinic, where some aspect of drug delivery, such as blood circulation lifetime, is improved over the basic formulation. Over 100 chemotherapeutics are used on their own or in combination with other chemotherapeutics to treat cancer. Therefore, an exhaustive list of clinically used treatments is beyond the scope of this thesis. However, several reviews of clinical research give an overview of treatments used for different types of cancer.[80-84]

1.3.2 Doxorubicin

Doxorubicin one of the most widely used chemotherapeutics,[76, 77] having first been approved for use in the United States in the 1970's. It is currently on the list of the World Health Organization's "Essential Medicines" and is specifically cited by the World Health Organization as a cytotoxic medicine for the treatment of five types of lymphoma, three types of sarcoma, and both early-stage and metastatic breast cancer.[85] However, doxorubicin is also used to treat bladder, stomach, lung, ovarian, and thyroid cancers. Doxorubicin was first isolated from the bacteria *Streptomyces peucetius* along with daunorubicin, a chemotherapeutic that differs from doxorubicin by the lack of a single hydroxyl group.[86]

Doxorubicin, and other similar anthracyclines, interact with DNA by intercalating into the DNA structure.[86-89] This intercalation is known to prevent the action of DNA and RNA polymerase, which leads to the cessation of DNA replication and RNA transcription. Doxorubicin is also capable of stabilizing topoisomerases during the coiling and un-coiling process of the nuclear DNA. This stabilization of the topoisomerase system prevents re-sealing of the DNA helix after it has been broken for coiling or uncoiling, and eventually leads to cell death.[90] Additionally, it has been shown that doxorubicin can lead to the increased production of reactive oxygen species such as hydroxyl radicals, which can lead to further DNA damage and inhibition of macromolecule production.[91] There is evidence to suggest that each mechanism of doxorubicin cytotoxicity occurs at different doxorubicin concentrations, with sub-micromolar concentrations leading to interference of DNA replication and RNA transcription, with concentrations between 2 and 4 μM leading to free

radical production, and concentrations near peak plasma concentration immediately after injection leading to topoisomerase stabilization and inhibition.[92]

Doxorubicin is available in several formulations for different clinical applications. The original formulation consisted of solely doxorubicin delivered intravenously. This formulation is sold under the trade name Adriamycin and is commonly delivered as part of a chemotherapeutic cocktail with other chemotherapeutics such as paclitaxel, or its synthetic derivative docetaxel. In 2005, a PEGylated liposomal form of doxorubicin was approved by the FDA for use in the United States.[7] The PEG coating of the liposomal form helps to increase the of blood circulation lifetime of doxorubicin, thereby increasing its efficacy through the EPR effect. The incorporation of targeting molecules into the delivery mechanisms of doxorubicin should lead to significant increase in efficacy and decrease in side-effects.

2 Aptamer Micelles Targeting Fractalkine-Expressing Cancer Cells *In Vitro* and *In Vivo*

* Adapted with permission from *Harris, Pearce et al.* Copyright 2017 Elsevier.[93]

2.1 Summary

In this work we hypothesized that the chemokine fractalkine can serve as a cancer molecular target. We engineered aptamer micelles functionalized with an outer PEG corona and investigated the extent and efficacy of using them as a targeting tool against fractalkine-expressing colon adenocarcinoma cells. *In vitro* cell binding results showed that aptamer micelles bound and internalized to fractalkine-expressing cancer cells with the majority of the micelles found free in the cytoplasm. Minimal surface binding was observed by healthy cells. Even though partial PEGylation did not prevent serum adsorption, micelles were highly resistant to endonuclease and exonuclease degradation. *In vivo* biodistribution studies and confocal studies demonstrated that even though both aptamer and control micelles showed tumor accumulation, only the aptamer micelles internalized into fractalkine-expressing cancer cells, thus demonstrating the potential of the approach and showing that fractalkine may serve as a specific target for nanoparticle delivery to cancer cells.

2.2 Introduction

Nanomedicine has developed into a promising field for the delivery of therapeutics to tumors, but with several obstacles that need to be resolved. Tumor targeting in general is aided by the EPR effect,[2] whereby macromolecules show preferential accumulation in

tumor tissue compared to healthy tissue. The size and shape of nanoparticles used for *in vivo* delivery can strongly affect the biodistribution and cellular uptake of the nanoparticles.[51, 94-98] Additionally, the charge of the nanoparticles,[99] types of targets used such as folate receptor, epidermal growth factor receptor (EGFR) or integrins,[100] and the extent of functionalization with polymeric materials such as PEG[101] can strongly affect the ability of the nanoparticle to enter the tumor tissue and internalize into the tumor cells. The extent of internalization must be considered when delivering therapeutics that do not readily cross the cell membrane, such as microRNA (μRNA) or small interfering RNA (siRNA) therapeutics.

ssDNA or RNA aptamers are a class of oligonucleotides that demonstrate high binding affinity for specific target molecules. Aptamers have been used to decorate different nanoparticles such as gold and iron oxide nanoparticles, carbon nanotubes, liposomes, micelles, and polymeric nanoparticles in order to provide targeting capabilities to these nanoparticles.[102] A SELEX process was used to develop a 40 nucleotide (nt) guanine-rich ssDNA aptamer, FKN-S2,[103] that targets a novel chemokine, fractalkine, with high affinity (K_d = 3.4 ± 0.7 nM of the free aptamer for fractalkine) and specificity, binding to the chemokine domain of fractalkine. Fractalkine, also known as CX_3CL1,[104] and one other chemokine, CXCL16,[105] are the only chemokines that exist in two active forms, membrane-bound and soluble. The soluble form is produced by cleavage of membrane-bound fractalkine near the cell membrane by the metalloproteinases ADAM10 and ADAM17, and is a chemoattractant for monocytes, natural killer cells and T-cells.[106, 107] The membrane-bound fractalkine captures CX_3CR1 (fractalkine receptor)-expressing leukocytes via

integrin-independent binding,[108] and has been shown to actively cycle between the plasma membrane and an internal, moderately acidic, vesicular pool.[109] The chemokine domain of fractalkine sits on a glycosylated mucin-like stalk whose role is to extend the chemokine domain away from the cell membrane to decrease steric hindrance to binding.[110]

Fractalkine is involved in several inflammatory disorders and the pathogenesis of different types of cancer.[111] Constitutive expression of fractalkine on healthy organs is low or absent, while overexpression is seen under inflammation or cancer. For example, fractalkine was either not expressed, or a negligible diffuse expression was observed on normal human kidneys, while fractalkine was highly expressed in patients with renal inflammation or renal allograft rejection.[112, 113] Fractalkine was absent in normal coronaries but present in several patients with coronary artery inflammatory disease.[114] In patients with colorectal cancer, fractalkine was detectable to significantly higher extents than in healthy mucosa.[115] Similarly, normal human livers showed low levels of fractalkine, while increased expression was detected in patients with hepatitis.[116]

Protein overexpression on cancer cells is a desirable feature for targeting. EGFR, for example, is expressed on healthy organs such as skin, liver, head, neck and gastrointestinal tract, and is overexpressed on different cancerous tissues, where the percentage of tumors that overexpress EGFR vary by tumor type.[117, 118] Fractalkine's overexpression in different diseases, and its ability to internalize, are two features that may make fractalkine a promising target for the delivery of therapeutics, as incorporation of fractalkine-targeting epitopes may allow both targeting and internalization of nanoparticles in a specific manner.

Even though a CX_3CR1 antagonist has been developed (a small-molecule called AZD8797),[119] and shown to have efficacy in a rat model for multiple sclerosis,[120] this is the first demonstration of a ssDNA aptamer, or any other ligand being used to target fractalkine, for *in vitro* and *in vivo* delivery of nanoparticles to fractalkine-expressing cancer cells.

We have previously developed FKN-S2 aptamer-amphiphiles by conjugating a C_{16} dialkyl tail to the FKN-S2 aptamer.[121] These aptamer-amphiphiles self-assembled in aqueous solution into micelles and nanotapes (flat bilayer structures that are often twisted) depending on the spacer used between the dialkyl tail and FKN-S2. The binding affinity of the aptamer was found to be affected by the addition of the tail, the orientation of the aptamer and type of spacer used.[121] Conjugation of FKN-S2 at its 3'-end to a C_{16} dialkyl tail with a ten thymine oligonucleotide spacer (T_{10} spacer-dialkyl tail) showed the highest binding affinity of different FKN-S2-amphiphiles for fractalkine, although other spacers, such as short PEG, were also investigated.[121] The 40nt FKN-S2 aptamer with the T_{10} spacer at its 3'-end, conjugated to a $(C_{16})_2$ tail, self-assembled into micelles and will henceforth be referred to as FKN-S2-T_{10} aptamer-amphiphile.

In this work, we show the ability for small self-assembled PEGylated micelles composed of FKN-S2-T_{10} aptamer-amphiphiles to specifically target and internalize into cancer cells that express fractalkine. In previous studies the aptamer extended outside the PEG corona of a polymeric nanoparticle,[122] gold nanoparticle,[123] or micelle,[124] for example. This exposed the aptamer to nucleases and rapid enzymatic cleavage,[123] and was shown to

compromise the antifouling properties of PEG at increased aptamer surface densities.[122] In this study we took a different approach where PEG_{5000} was attached at the 5'-end of the aptamer, thus providing an outer PEG corona to the aptamer micelle.

In vitro uptake experiments investigated the binding and internalization of the FKN-S2-T_{10} micelles (PEGylated or not) by mouse colon adenocarcinoma MCA-38 cells transfected to expressing human fractalkine (MCA-38.FKN)[121] and by control healthy human BJ fibroblasts. Binding and internalization of PEGylated FKN-S2-T_{10} micelles to control human colonic epithelial cells (HCoEpiC) was also examined. PEGylated FKN-S2-T_{10} and control micelles (formed by a random ssDNA-amphiphile with no guanines) were further investigated *in vivo* and therefore, their stability to serum and nucleases was examined. *In vivo* experiments using a subcutaneous MCA-38.FKN tumor model evaluated biodistribution of the micelles overtime via micro positron emission tomography (μPET)/computerized tomography (CT). Ex vivo biodistribution studies were also performed. Confocal microscopy of the tumors investigated cell internalization of the PEGylated FKN-S2-T_{10} and control micelles by the fractalkine-expressing cancer cells. As a proof of concept, we demonstrated in this study that fractalkine can be used as targeting molecule both *in vitro* and *in vivo* and that even though PEGylated micelles can extravasate into the tumor independent of the ssDNA used to form the micells, the FKN-S2-T_{10} aptamer is required for cell internalization by the fractalkine-expressing cancer cells.

2.3 Methods

2.3.1 Materials

All materials were purchased from Sigma-Aldrich (St. Louis, MO) and used without further purification or modification unless otherwise stated. Buffers include high performance liquid chromatography (HPLC) buffer A (100 mM hexafluoroisopropanol and 15 mM triethylamine in water), HPLC buffer B (100 mM hexafluoroisopropanol and 15 mM triethylamine in methanol), TEAA buffer (50% molar basis triethylamine, 50% molar basis glacial acetic acid, pH = 7.0), Cu-TBTA (10 mM Copper (II)-Tris[(1-benzyl-1H-1,2,3-triazol-4-yl)methyl]amine in 55% dimethyl sulfoxide (DMSO), 45% water), 1X phosphate buffered saline (PBS) (137 mM sodium chloride, 2.7 mM potassium chloride, 10 mM disodium phosphate, 1.8 mM monopotassium phosphate in water), and 1X TBST (tris-buffered saline 20X (1 M) with tween 20 (BioLegend, San Diego, CA), diluted to 1X with distilled water, pH adjusted to 7.6 with HCl).

2.3.2 Synthesis of ssDNA-Amphiphiles

ssDNA sequences were purchased from Integrated DNA Technologies (Coralville, IA) with a 3’ amino-modifier for conjugation to the hydrophobic tail. The 5’ end was either unmodified or was ordered with a fluorophore (HEX 538(ex)/555(em) nm, Cy5 648(ex)/668(em) nm, FAM 495(ex)/520(em)), or alkyne group for further modification. The FKN-S2 aptamer with T_{10} spacer (FKN-S2-T_{10}: 5’-GGGGT GGGTG GGGGG CACGT GTGGG GGCGG CCAGG GTGCT TTTTT TTTTT-AmMo-3’) and control, random sequence containing no guanines, with T_{10} spacer (5’-TTCTA TTCTC ACATT TCATC TATTA AACCA CCAAT TAATT TTTTT TTTTT-AmMo-3’) were used in this

study. ssDNA was precipitated in water using 100 mM cetyl trimethylammonium bromide (CTAB) followed by resuspension in a 90%/10% (v/v) mixture of dimethylformamide (DMF) and DMSO at 500 µM. C_{16} dialkyl tails, synthesized as described elsewhere,[121] were added in 10X molar excess and reacted overnight at 60 °C. The solution was concentrated by drying under air stream until approximately 100 µL in volume. The ssDNA was precipitated by an ethanol precipitation, where 900 µL of ethanol were added followed by 30 µL of 3 M sodium acetate in water and 270 µL of water and placed in a -20 °C freezer for a minimum of 2 h. The precipitate was centrifuged, rehydrated with 800 µL of water and filtered through a 0.45 µm PES filter. The filtered ssDNA-amphiphiles were then separated from unreacted ssDNA using HPLC with HPLC buffer A and HPLC buffer B over 30 min. ssDNA-amphiphiles were then dried to approximately 1 mL, precipitated via ethanol precipitation to remove HPLC buffer components, and rehydrated at 500 µM in water for storage at -20 °C.

2.3.3 Alkyne DOTA-Thiol Reaction

ssDNA-amphiphiles with a 5' alkyne modification were mixed with 10 molar equivalents of 1,4,7,10-tetraazacyclododecane-1,4,7,-tris(acetic acid)-10-(2-thioethyl)acetamide (DOTA-thiol) and one tenth molar equivalents of 2-hydroxy-2-methylpropiophenone photoinitiator in water. The solution was degassed under vacuum for 15 min and stirred under UV light for 2 h. The solution was dialyzed overnight using a Tube-O-DIALYZER Medi 1K MWCO dialysis membrane (G-Biosciences, St. Louis, MO). DOTA-labeled ssDNA-amphiphiles were then concentrated to 500 µM by drying under an airstream.

2.3.4 PEG Click Reaction

ssDNA-amphiphiles with a 5' alkyne modification were mixed in 50% water and 50% DMSO to a final concentration of 100 µM. TEAA buffer was added to a concentration of 200 mM, Cu-TBTA buffer was added to a concentration of 1 mM, ascorbic acid was added to a concentration of 2 mM, and PEG_{5000}-azide was added in 5 times molar excess of the ssDNA-amphiphiles. The solution was mixed and left overnight in the dark at room temperature, followed by an ethanol precipitation to remove excess buffer components. The PEGylated ssDNA-amphiphiles were rehydrated at 500 µM in water for storage at -20 °C.

2.3.5 Liquid Chromatography-Mass Spectroscopy (LC-MS)

ssDNA-amphiphiles were analyzed using an Agilent 1100 LC MSD Model G1946 Mass Spectrometer at the University of Minnesota Masonic Cancer Center. ssDNA-amphiphiles at 500 µM were injected with 4 µL of volume onto a 300 µm C3 column with a 20-min gradient between 15 mM ammonium acetate in water and acetonitrile. The eluent of the chromatography column was sent to the mass spectrometer in order to determine the mass of the ssDNA-amphiphiles.

2.3.6 Proton Nuclear Magnetic Resonance (^1H NMR)

^1H NMR spectra were recorded on a Bruker 850 MHz spectrometer at the University of Minnesota NMR Center with 98% H_2O/2% DMSO or 98% H_2O/2% D_2O at room temperature.

2.3.7 Micelle Preparation

Micelle samples were prepared by heating a solution of different ssDNA-amphipiles at the desired ratios to 90 °C for 15 min and cooling to room temperature. Heating was done to induce disassembly of the amphiphiles[24] and allow for formation of micelles composed of all different amphiphiles in the solution upon cooling.

2.3.8 Dynamic Light Scattering (DLS) and Zeta Potential

DLS and zeta potential measurements were made using a Brookhaven ZetaPALS Particle Analyzer. 250 µM ssDNA-amphiphile solutions were diluted to ~20 µM with 1X PBS and transferred to a 1.0 cm path length cuvette for data collection. For each micelle sample three independent DLS and zeta potential measurements were performed (n=3), each consisting of ten 1-min runs.

2.3.9 Cyrogenic Transmission Electron Microscopy (Cryo-TEM)

Lacey Formvar/Carbon 200 mesh copper grids were purchased from Ted Pella (Redding, CA) and glow-discharged for 1 min to make the grids more hydrophilic. 4.5 µL of 400 µM ssDNA-amphiphiles in 1X PBS were deposited onto the grid and vitrified in liquid ethane by Vitrobot (Vitrobot parameters: 4.5 sec blot time, 3 sec wait time, 3 sec relax time, 0 offset, 95% humidity). The grids were kept under liquid nitrogen and transferred to a Tecnai G2 Spirit TWIN 20-120 kV/LaB6 TEM operated at an accelerating voltage of 120 kV and an Eagle 2k CCD camera at the University of Minnesota Characterization Facility. Size analysis of 25 micelles from each formulation was performed using ImageJ.

2.3.10 Circular Dichroism (CD)

250 µM solutions of ssDNA-amphiphile were diluted to 5 µM with 1X PBS and transferred to a 1.0 cm path length cuvette. CD spectra from 320-200 nm were collected using a Jasco J-815 spectrapolarimeter at the University of Minnesota Biophysical Technology Center, using a read speed of 50 nm min^{-1} in 1 nm steps. Three accumulations per amphiphile solution were recorded with the background spectrum of 1X PBS automatically subtracted. The accumulations were averaged and the raw ellipticity values were converted to molar ellipticity.

2.3.11 Cell Culture

MCA-38.FKN cells[121] or BJ fibroblasts (American Type Culture Collection, Manassas, VA) were cultured at 37 °C and 5% CO_2 using Dulbecco's Modified Eagle Medium (DMEM) (Thermo Fisher Scientific, Rockford, IL) supplemented with 10% (v/v) fetal bovine serum (FBS) (Thermo Fisher Scientific, Rockford, IL). Human colonic epithelial cells (HCoEpiC) (ScienCell Research Laboratories, Carlsbad, CA) were cultured at 37 °C and 5% CO_2 using colonic epithelial cell medium supplemented with 100 units/mL penicillin, 0.1 mg/mL streptomycin, and 5 mL of colonic epithelial cell growth supplement (ScienCell Research Laboratories, Carlsbad, CA). Cells were passaged when they reached 80% confluence by treatment with TrypLE Express cell dissociation agent (Thermo Fisher Scientific, Rockford, IL).

2.3.12 Fractalkine Expression via Flow Cytometry

Fractalkine expression of MCA-38.FKN cells, BJ fibroblasts, and HCoEpiC was assessed by flow cytometry. $2x10^5$ MCA-38.FKN cells and $1x10^5$ BJ fibroblasts were each suspended in 200 µL of binding buffer consisting of 1X PBS supplemented with 1% (w/v) bovine serum albumin (PBS/BSA) and 5 µg/mL of anti-fractalkine antibody (AF365, R&D Systems, Minneapolis, MN) or an isotype control (02-6202, Thermo Fisher Scientific, Rockford, IL) were added. $2x10^4$ HCoEpiC were suspended in 200 µL of PBS/BSA with 2 µg/mL of anti-fractalkine antibody or the isotype control. After incubating for 30 min at 4 °C, the cells were centrifuged, washed with PBS/BSA and suspended in 200 µL of PBS/BSA with 5 µg/mL (2 µg/mL were used for HCoEpiC) of a fluorescently labeled secondary antibody (NL002, R&D Systems, Minneapolis, MN). The cells were incubated with the secondary antibody for 30 min at 4 °C, washed twice with PBS/BSA, and assessed for fractalkine expression by flow cytometry (BD Accuri C6, University Flow Cytometry Resource, University of Minnesota).

2.3.13 Micelle Binding and Internalization via Flow Cytometry

Micelle samples containing 10 mol% HEX-labeled FKN-S2-T_{10} aptamer-amphiphiles and different concentrations of PEGylated FKN-S2-T_{10} aptamer-amphiphiles and FKN-S2-T_{10} aptamer-amphiphiles were prepared at 250 µM in 1X PBS. 25,000 MCA-38.FKN cells, or 10,000 BJ fibroblasts were added to a 24-well plate and allowed to attach and proliferate for 24 h. After 24 h, fresh media and the micelle solutions were added to the cells at a final amphiphile concentration of 12.5 µM for each micelle sample. After an additional 24 h at 37 °C the micelle solution was removed, the cells were detached from the plate, washed

with PBS, and analyzed with an Accuri C6 flow cytometer to assess the amount of cell fluorescence. The raw fluorescence data were scaled to the cell surface area of the MCA-38.FKN or BJ fibroblasts to account for the substantial difference in cell size. The average surface area of 100 cells was calculated using ImageJ as 1,191 μm^2 for the MCA-38.FKN cells and 5,409 μm^2 for the BJ fibroblasts. Three independent experiments were conducted and the data analyzed for statistical significance between each micelle sample using a two-way ANOVA with Tukey's HSD post-hoc test. PEGylated FKN-S2-T_{10} micelles were also delivered to 25,000 MCA-38.FKN cells and 25,000 HCoEpiC for 24 h at 37 °C following the above protocol. MCA-38.FKN and HCoEpiC were compared using fluorescence values. Three independent experiments were performed and statistical significance was evaluated by student's t-test analysis.

2.3.14 Micelle blocking with FKN-S2-T_{10} free aptamer via flow cytometry

Micelles containing 20 mol% HEX-labeled FKN-S2-T_{10} aptamer-amphiphiles, 40 mol% PEGylated FKN-S2-T_{10} aptamer-amphiphiles and 40 mol% FKN-S2-T_{10} aptamer-amphiphiles were prepared at 250 µM in 1X PBS, while free FKN-S2-T_{10} aptamer (5'-GGGGT GGGTG GGGGG CACGT GTGGG GGCGG CCAGG GTGCT TTTTTTTTTT-3') was prepared at 1 mM in 1X PBS. 100,000 MCA-38.FKN cells were suspended in vials with 1 mL of 1X PBS. 150 µL of 1X PBS (unblocked sample), or 150 µL free FKN-S2-T_{10} aptamer (blocked sample) were added to the cell vials and incubated at 4 °C for 1 h. 6 µL of micelle solution were added to the cell vials and incubated for an additional 1 h at 4 °C. Cells were washed twice with 1X PBS, resuspended in 1X PBS and measured for fluorescence with an Accuri C6 flow cytometer.

2.3.15 Micelle Binding and Internalization via Confocal Microscopy

Micelles containing 10 mol% Cy5-labeled FKN-S2 aptamer-amphiphiles, 45 mol% PEGylated FKN-S2-T_{10} aptamer-amphiphiles and 45 mol% FKN-S2-T_{10} aptamer-amphiphiles were prepared at 250 µM in 1X PBS. 20,000 MCA-38.FKN, HCoEpiC, or BJ fibroblast cells were deposited onto glass coverslips contained within wells of a 24-well plate and allowed to attach and proliferate for 24 h. After 24 h, 25 µL of the micelle solution was added to the cells, bringing the final amphiphile concentration to 12.5 µM. 24 h after the micelles were added, cells were fixed with 4% paraformaldehyde and their nuclei and membranes simultaneously stained for 10 min with Hoescht 33342 (Thermo Fisher Scientific, Rockford, IL) at 0.92 µg/mL for the nucleus and Wheat Germ Agglutinin AlexaFluor594 (Thermo Fisher Scientific, Rockford, IL) at 5.0 µg/mL for the membrane.

For the organelle staining and colocalization study, after MCA-38.FKN cells proliferated for 24 h, 25 µL of the micelle solution and 10 µL of CellLight Early Endosomes-GFP (Thermo Fisher Scientific, Rockford, IL) were added to the cells, bringing the final amphiphile concentration to 12.5 µM. Lysosomes were stained using Lysotracker Red (Thermo Fisher Scientific, Rockford, IL) by adding 5 µL of a 20 µM Lysotracker Red solution to the cells (final concentration: 200 nM) 2 h prior the 24 h experimental end-point. 24 h after the micelles were added, cells were fixed with 4% paraformaldehyde and their nuclei stained with Hoescht 33342 at a concentration of 0.92 µg/mL for 10 min.

Cells were mounted onto glass slides using Prolong Gold and imaged with an Olympus FluoView FV1000 BX2 Upright Confocal microscope (University Imaging Centers, University of Minnesota).

2.3.16 Micelle Serum Stability via Gel Electrophoresis

Three different micelle formulations were investigated for stability after exposure to serum: FKN-S2-T_{10} micelles, PEGylated FKN-S2-T_{10} micelles, and PEGylated control micelles. All micelles contained 20 mol% HEX-labeled ssDNA-amphiphiles and were prepared at 250 µM in water. Micelles were mixed into three separate conditions using 2.5 µL of micelles and 47.5 µL of solution, for 50 µL total mixture: 1X PBS as a control, 10% (v/v) FBS in water to mimic *in vitro* conditions, and 90% (v/v) FBS in water to mimic *in vivo* conditions. Micelle solutions were incubated at 37 °C for 24 h and were run on 2% agarose gels (2% agarose in 1X TAE buffer) at 120V for 35 min, and imaged using a ChemiDoc MP Imaging System (Bio-Rad, Hercules, CA).

2.3.17 Micelle Exonuclease/Endonuclease Degradation via Gel Electrophoresis

Three different micelle formulations were investigated for degradation after exposure to DNase I and exonuclease III (Thermo Fisher Scientific, Rockford, IL): FKN-S2-T_{10} micelles, PEGylated FKN-S2-T_{10} micelles, and PEGylated control micelles. All micelles contained 20 mol% HEX-labeled ssDNA-amphiphiles and were prepared at 250 µM in water. Micelles were mixed into four separate conditions to test for nuclease degradation by using 2.5 µL of micelles and 47.5 µL of solution, for 50 µL total mixture: 0-5 U/mL in 1X reaction buffer provided by the kit for DNase I, as well as 0-5 U/mL in 1X reaction

buffer provided by the kit for exonuclease III. Micelle solutions were incubated at 37 °C for 24 h, run on 2% agarose gels at 120V for 40 min, and imaged using a ChemiDoc MP Imaging System (Bio-Rad, Hercules, CA).

2.3.18 Copper Chelation Assay

^{64}Cu is a popular isotope due to its 12.7 h half-life, allowing PET scans for up to 48 h after injection.[125] To verify that copper would bind to DOTA-labeled FKN-S2-T_{10}-amphiphiles a copper chelation assay was designed. Copper (Cu^{2+}) standard solutions ranging between 0 and 40 µM were created by mixing a 100 µM $CuCl_2$ stock solution with water, and then diluted by a factor of two using 100 mM sodium acetate, buffered to pH 6 with acetic acid, thus creating solutions ranging between 0 and 20 µM Cu^{2+} in 150 µL of total solution. Additional samples of 10 µM Cu^{2+} were created via the same method to be mixed with ssDNA micelles containing 5 mol% DOTA-labeled FKN-S2-T_{10}-amphiphiles, 47.5 mol% PEGylated FKN-S2-T_{10}-amphiphiles, and 47.5% FKN-S2-T_{10}-amphiphiles. Samples with DOTA:Cu^{2+} ratios varying between 1 and 10 were created by mixing 15 µL of 100 µM $CuCl_2$ solution, 500 µM DOTA-labeled micelles in water (1.5 µL for equimolar through 15 µL for 10X excess), 15 µL of 10X PBS, and diluted to 150 µL total volume with water. All solutions were lightly vortexed and incubated at 37 °C for 1 h. To precipitate the ssDNA and leave only the free, unchelated Cu^{2+} in solution, 1 mL of 2.5% (w/v) $LiClO_4$ in acetone was added to all solutions, vortexed, and incubated at -20 °C for 15 min. The solutions were centrifuged for 15 min at 16,100g and the supernatant was collected and dried completely overnight in a heated vacuum. Dried samples were rehydrated with 100 µL water and incubated with a Copper Assay Kit according to the manufacturer's instructions.

The absorbance of each sample was measured at 359 nm to determine the amount of free Cu^{2+} in solution. Linear regression was performed on triplicate measurements of the standard solutions. The results of this regression were used to determine the concentration of unchelated Cu^{2+} left in the DOTA-labeled ssDNA samples (n = 3).

2.3.19 Micro-positron Emission Tomography (μPET)/Computerized Tomography(CT) Imaging of Animal Model

MCA-38.FKN cells were suspended in 1X PBS at 10^6 cells/mL. 100 μL of the cell suspension was injected into subcutaneous space of the shoulder of Jackson J:Nu female homozygous mice (Jackson Labs, Bar Harbor, ME). Tumors were allowed to grow to approximately 1 mL in volume before mice were injected with ^{64}Cu-DOTA-labeled micelles. Micelle samples with FKN-S2-T_{10} aptamer-amphiphiles or control-amphiphiles containing 5 mol% DOTA-labeled ssDNA-amphiphiles, 47.5 mol% PEGylated ssDNA-amphiphiles, and 47.5% ssDNA-amphiphiles at 250 μM were diluted to 150 μM in 2X PBS. The ^{64}Cu (Department of Medical Physics, University of Wisconsin, Madison) was diluted to 2 μCi/μL in 100 mM sodium acetate in water at pH=6, mixed with the micelle solution (1:1 v/v) and incubated at 37 °C for 1 h to give a final ssDNA-amphiphile concentration of 75 μM in 1X PBS and 1 μCi/μL of ^{64}Cu.

Mice were placed under a heat lamp prior to injections to dilate the veins in their tails. The tails were wiped with ethanol swabs to clean them prior to injection and 200 μL of the ^{64}Cu-labeled micelle solution was injected into the lateral tail veins of the mice. The final solution to be injected contained approximately 0.8 pmol ^{64}Cu and 1.5 nmol of DOTA, approximately 1,850X molar excess of DOTA to ^{64}Cu. The radioactivity and time of

measurement of each individual syringe was measured immediately before and after tail vein injections. 15 min prior to each imaging time point (1, 3, 24 h after injection), mice were anesthetized using 3% isofluorane in oxygen at 0.8 L/min flow. μPET and CT scans were taken on a Siemens Inveon μPET/CT scanner (Center for Magnetic Resonance Research, University of Minnesota). After the 1 h and 3 h imaging time points, mice were placed under a heat lamp until they regained consciousness. After the 24 h time point, mice were euthanized for ex vivo organ radioactivity measurements.

All animal work in this chapter was approved by the IACUC at the University of Minnesota – Twin Cities.

2.3.20 In Vivo Biodistribution Analysis

Manual segmentation of CT scans to identify the location of each organ is cumbersome and prone to bias, so Digimouse,[126] a reference dataset, was used. Digimouse provides a CT scan of a mouse, together with an image where each pixel is assigned a label corresponding to the organ at that location, also known as atlas. Images of two to four mice were acquired simultaneously, so the first step was to separate the CT and μPET images into two to four images of each individual mouse. This was done using a custom interactive tool written for MevisLab (http://www.mevislab.de). Care was taken to maintain the coordinate system and the calibrated radiological values contained in the original DICOM files.

The workflow of the μPET/CT image analysis is illustrated in Figure S12. To avoid artifacts in calculating the transformation, the tumor area was excluded from the

estimation. The tumor was segmented using ITK-SNAP, a free open-source software to perform semi-automatic segmentation using adaptive contours. First, an upper and lower threshold were used to separate the tumor tissue from the surrounding material and determine the direction and speed of the adaptive contour in the next step; then, the union of a few spherical ROIs were used to initialize the contour; finally, the contour went through several steps of evolution to adapt itself to the shape of the tumor.

To find the transformation from the CT image of the Digimouse to the CT image from the scanned mouse, a three-step registration workflow was performed: rigid-body, affine and elastic transformation model based on B-Splines. Elastix, a free open-source software was used for elastic registration. The tumor segmentation was used as an exclusion region during the estimation of the transformation. The resulting transformation was then applied to the atlas from Digimouse using a nearest-neighbor approximation, and the transformed atlas was combined with the segmentation of the tumor by assigning a new, unassigned label to every pixel in the tumor. The resulting atlas was in the coordinate system and spacing of the CT image, so the following step was to transform the atlas into the coordinate system and spacing of the µPET image using the “applyTransform” command from the ANTs toolbox (http://stnava.github.io/ANTs/), with the atlas as input, specifying no transformation and indicating the µPET image as reference. The µPET image radiation was quantified for each region in the resulting atlas. R in RStudio was finally used to extract the measurements of interest and export the data into an Excel table.

Radiation values tabulated from this analysis were decay-adjusted to allow comparisons at different time points. The total injected dose was calculated by measuring the time-normalized radiation in the syringe prior to injection and subtracting the time-normalized radiation in each syringe after injection as well as the time-normalized radiation in each mouse's tail after 24 h as measured from the ex vivo analysis. The tail value was subtracted due to the possibility of missing the vein during injection thus, limiting the amount of ^{64}Cu delivered to the whole body. The volume of each organ was converted to mass based on literature values for organ densities.[127, 128] The radiation values for each organ were adjusted for the decay of ^{64}Cu (12.7 h half-life). Data were plotted as percent injected dose per gram of tissue (%ID/gr) and student's t-test statistical analysis was used to evaluate statistical significance.

2.3.21 Ex Vivo Biodistribution Analysis

After the *in vivo* μPET/CT data were collected at the 24 h time point, mice were euthanized to collect organs for ex vivo measurements. Organs were excised and weighed to determine the mass. The radioactivity of each organ (kcpm) was recorded using a scintillator and converted to μCi using a calibration curve. The radiation values for each organ were adjusted for the decay of ^{64}Cu. The total injected dose was calculated as discussed above. Data were plotted as %ID/gr and compared with student's t-test statistical analysis.

2.3.22 Confocal Microscopy of Tumors

Mice were given subcutaneous MCA-38.FKN tumors using the same procedure as for the μPET/CT imaging. 200 μL of micelles with FKN-S2-T_{10} aptamer-amphiphiles or control-

amphiphiles consisting of 20 mol% FAM-labeled ssDNA-amphiphiles, 40 mol% PEGylated ssDNA-amphiphiles, and 40 mol% ssDNA-amphiphiles at 75 μM in 1X PBS were injected into the lateral tail vein of mice. After 24 h mice were euthanized, tumors excised and frozen in isopentane cooled by dry ice. Unstained frozen sections were cut (5 μm) and air dried overnight. The following day the slides were put into a tap water rinse for 5 min to hydrate and then moved to TBST buffer. Endogenous peroxidase activity was quenched by slide immersion in 3% hydrogen peroxide solution for 10 min followed by TBST rinse. A serum-free blocking solution, Rodent Block M (Biocare Medical, Concord, CA), was placed on sections for 1 h. Blocking solution was removed and slides were incubated in Wheat Germ Agglutinin AlexaFluor594 Conjugate (Thermo Fisher Scientific, Rockford, IL) used at a 1:200 dilution overnight at 4 °C. The next morning the slides were put into a TBST rinse followed by a 5 min incubation in 12.3 μg/mL Hoescht 33342 (Thermo Fisher Scientific, Rockford, IL). The slides were rinsed twice with TBST, 5 min each then into distilled water and cover slipped using VectaSheild anti-fading mounting media (Vector Laboratories, Burliggame, CA). Slides were kept frozen until imaging on an Olympus FluoView FV1000 BX2 Upright Confocal Microscope (University Imaging Centers, University of Minnesota).

2.4 Results

2.4.1 Synthesis and Characterization of Micelles

Synthesis steps for all ssDNA-amphiphiles are shown in Figure 2.1. Successful synthesis was verified using LC-MS (Table 2.1) as well as ^{1}H NMR (Figure 2.2, 2.3), showing the expected products from each reaction. Figure 2.4A shows the chemical structures of the

different ssDNA-amphiphiles used in this study. In order to investigate the effect of PEGylation on the targeting capability of the aptamer-amphiphiles, micelles were created with 0, 45 and 90 mol% PEGylated FKN-S2-T_{10} aptamer-amphiphiles (Figure 2.4B shows a cartoon of a PEGylated ssDNA micelle).

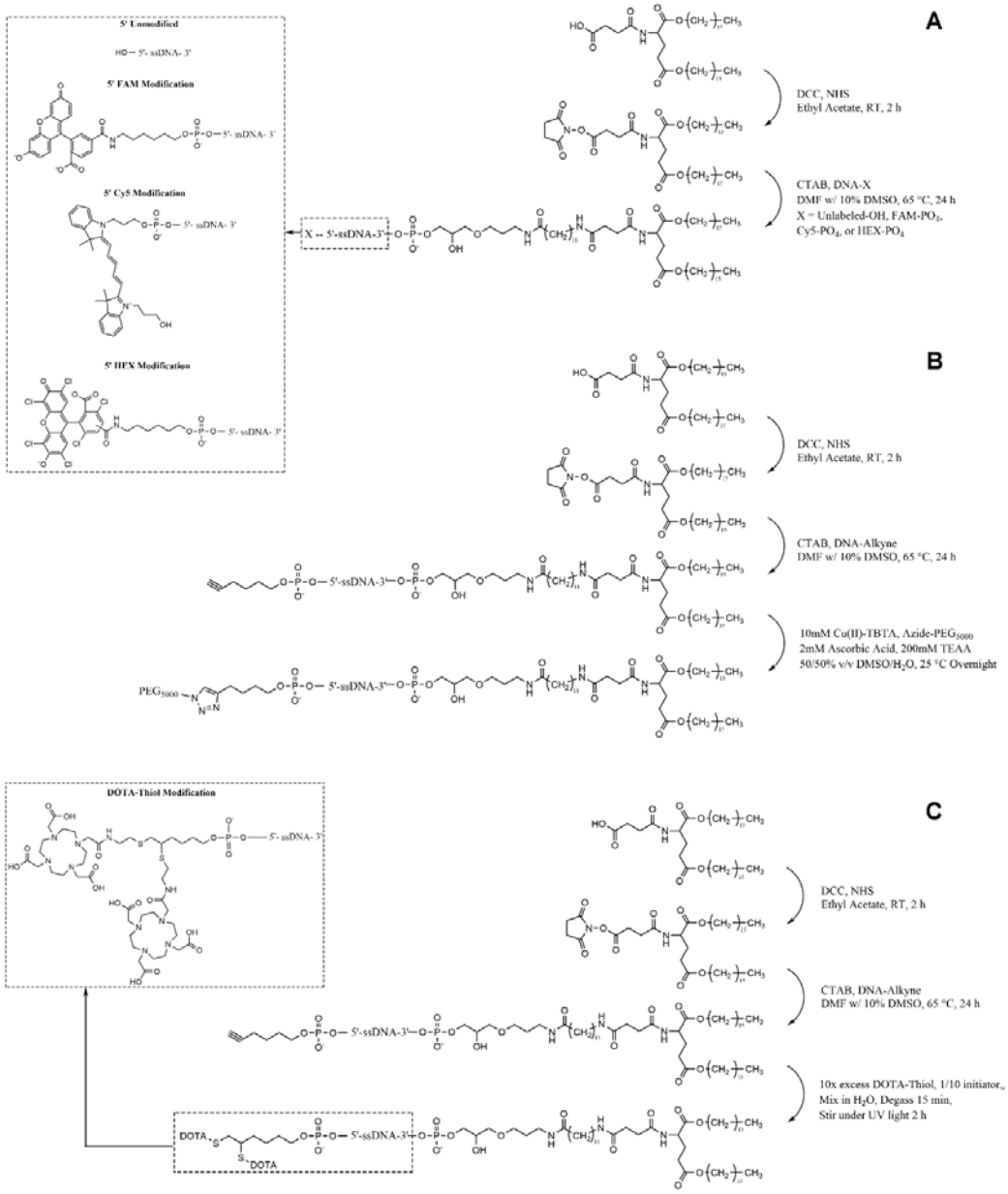

Figure 2.1 Synthesis schemes of ssDNA-amphiphiles (A) with or without fluorophores, (B) with PEG_{5000}, (C) with DOTA. The insets show the structures of the different probes attached to the 5' end of the ssDNA.

Table 2.1. Expected and measured masses of ssDNA-amphiphiles as determined by LC-MS.

Amphiphiles	Expected mass (M-H)	Observed mass (M-H)
FKN-S2-T_{10}	16,615.7	16,614.9
HEX-FKN-S2-T_{10}	17,359.4	17,359.2
Cy5-FKN-S2-T_{10}	17,147.9	17,147.4
DOTA-FKN-S2-T_{10}	17,693.6	17,693.0
Control	16,076.0	16,076.0
DOTA-Control	17,066.6	17,066.2

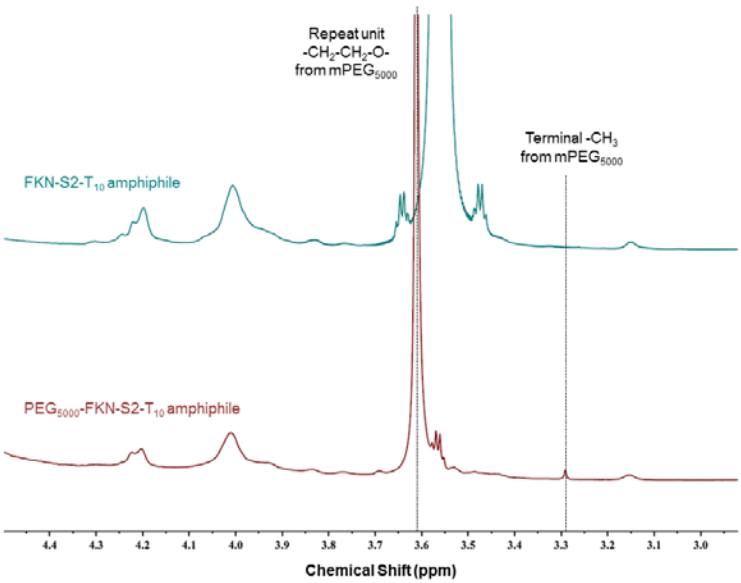

Figure 2.2. ^{1}H NMR of FKN-S2-T_{10} aptamer-amphiphile and PEG_{5000}-FKN-S2-T_{10} aptamer-amphiphile in 98% H_2O / 2% D_2O verifying PEGylation of the ssDNA-amphiphile.

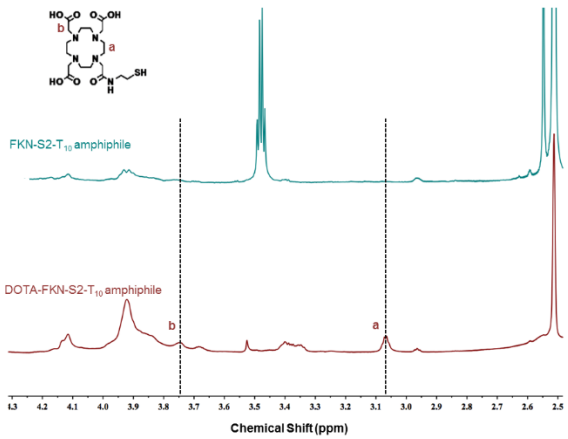

Figure 2.3. ^{1}H NMR of FKN-S2-T_{10} aptamer-amphiphile and DOTA-FKN-S2-T_{10} aptamer-amphiphile in 98% H_2O / 2% DMSO-d_6 verifying DOTA conjugation.

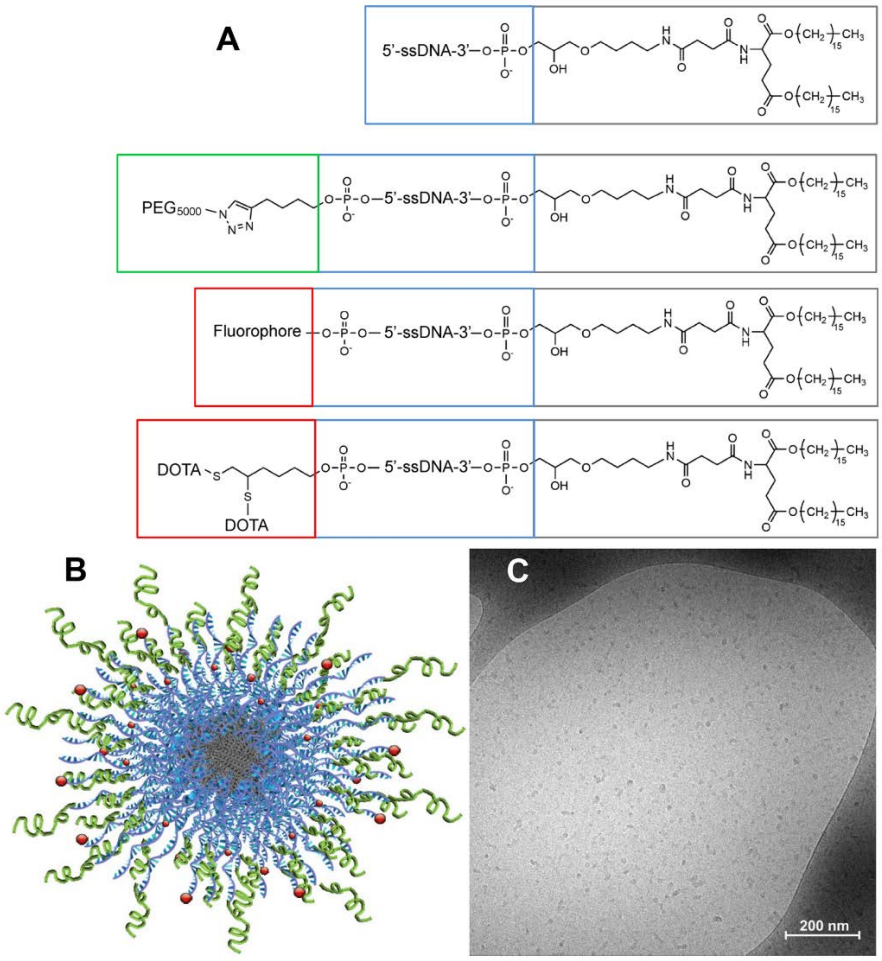

Figure 2.4. (A) Chemical structures of different ssDNA-amphiphiles used to create micelles. (B) Schematic representation of a PEGylated ssDNA micelle, where the ssDNAs are shown in blue (not showing any secondary structure), the hydrophobic tails in gray, PEG in green, and labels in red. Not drawn to scale. (C) Cryo-TEM of FKN-S2-T_{10} micelles with 45 mol% PEGylated FKN-S2-T_{10} aptamer-amphiphiles.

Zeta potential and sizes of different micelles are reported in Table 2.2. There was no statistically significant difference between groups with different concentrations of PEG5000, demonstrating no change in size or charge upon addition of PEG. Cryo-TEM showed that all amphiphiles formed 12x10 nm weakly ellipsoidal micelles (a cryo-TEM for the 45 mol% PEGylated FKN-S2-T10 micelles is shown in Figure 2.4C). DLS gave an average diameter of 18, 22 and 22 nm for the 0, 45 and 90 mol% PEGylated FKN-S2-T_{10} micelles respectively.

Table 2.2. Size and zeta potential of micelles with varying degrees of PEGylation. Data are presented as the mean ± SE. Student's t-test analysis showed that there was no statistically significant difference between groups with different concentrations of PEG_{5000}.

Micelles	Major x minor axis from cryo-TEM (nm)	Hydrodynamic diameter from DLS (nm)	Zeta potential (mV)
0 mol% PEG_{5000}-FKN-S2-T_{10}	12.5 ± 0.3 x 10.3 ± 0.3	18.4 ± 2.3	-18 ± 2
45 mol% PEG_{5000}-FKN-S2-T_{10}	12.3 ± 0.5 x 10.3 ± 0.3	22.1 ± 0.9	-17 ± 3
90 mol% PEG_{5000}-FKN-S2-T_{10}	12.0 ± 0.3 x 9.6 ± 0.3	21.7 ± 1.1	-15 ± 3
45 mol% PEG_{5000}-Control	11.9 ± 0.3 x 8.6 ± 0.2	17.2 ± 1.8	-17 ± 4

The free FKN-S2 aptamer formed a G-quadruplex and stem-loop secondary structure in PBS (Figure 2.5).[121] When conjugated to a T_{10} spacer-dialkyl tail, such as the one used in this study, the FKN-S2-T_{10}-amphiphiles self-assembled into micelles with a critical micelle concentration of around 50 nM, forming intermolecular G-quadruplexes within the

micelle.[121] CD was performed for the 0, 45 and 90 mol% PEGylated micelles and it was shown that all micelles showed a positive peak at 265-266 nm and a negative peak at 241-242 nm, characteristic of parallel G-quadruplex (Figure 2.6). However, the addition of PEG_{5000} to the 90 mol% PEGylated micelles did cause a change in the intensity of the peaks, suggesting that the G-quadruplex may have been destabilized to a certain extent.

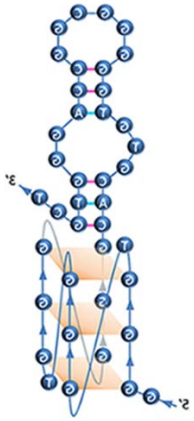

Figure 2.5. Cartoon of the secondary structure of the FKN-S2 aptamer.

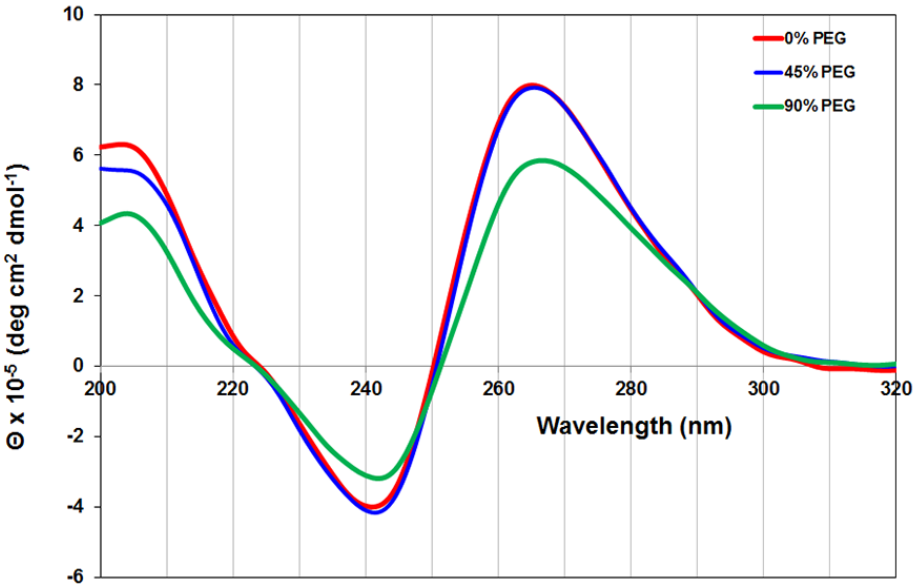

Figure 2.6. CD spectra of 5 µM FKN-S2-T_{10} aptamer-amphiphiles with different amounts of PEG_{5000} in 1X PBS. All micelles showed a positive peak at 265-266 nm and a negative peak at 241-242 nm characteristic of parallel G-quadruplex.

2.4.2 In Vitro Delivery of Micelles

Fractalkine expression was verified via flow cytometry for MCA-38.FKN cells and BJ fibroblasts (Figure 2.7A, 2.7B). Binding and internalization of FKN-S2-T_{10} micelles, and the effect of PEG_{5000} addition to cell association were first evaluated *in vitro* via flow cytometry. Fluorescence was normalized to the average surface area of each cell type to account for the substantial difference in cell size. Results in Figure 2.8 showed that MCA.38-FKN cells had a much higher associated fluorescence per area than BJ fibroblasts for each micelle mixture. Additionally, the non-PEGylated micelles had the highest fluorescence per area when delivered to MCA-38.FKN cells, while there was no statistical difference between the 45 and 90 mol% PEGylated micelles. There was also no statistically significant difference between the cell association of the three micelle formulations when delivered to BJ fibroblasts. Even though the addition of PEG_{5000} inhibited binding and internalization of FKN-S2-T_{10} micelles to the MCA-38.FKN cells to some extent, PEGylated micelles were used for further studies, as PEG has been shown to improve serum stability, blood circulation and immunogenic response of nanoparticles, resulting in higher tumor accumulation.[129, 130] Throughout the remaining experiments, all micelles (referred to as PEGylated micelles) were formulated with the smallest percentage of probe-labeled amphiphiles that would provide a satisfactory signal-to-noise ratio. The remaining percentage of amphiphiles was split evenly between PEGylated and non-PEGylated amphiphiles. Table 1 shows all micelle compositions for each experiment performed in this study.

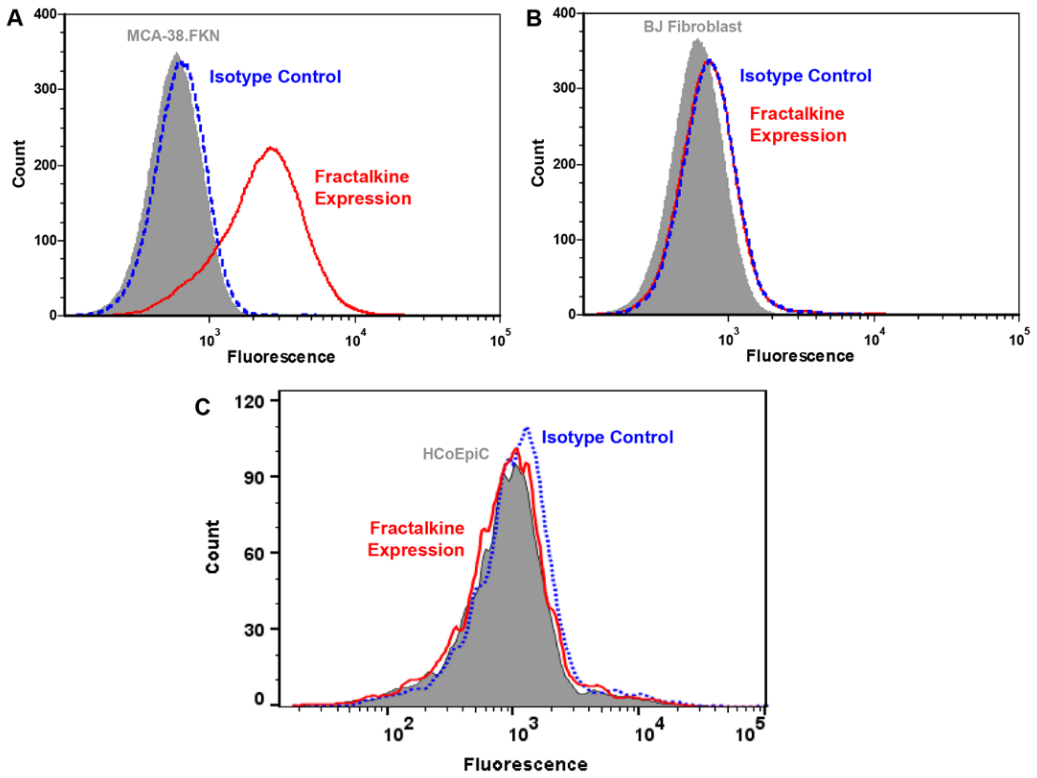

Figure 2.7. Fractalkine expression on (A) MCA-38.FKN cells, (B) BJ fibroblast cells, and (C) HCoEpiC.

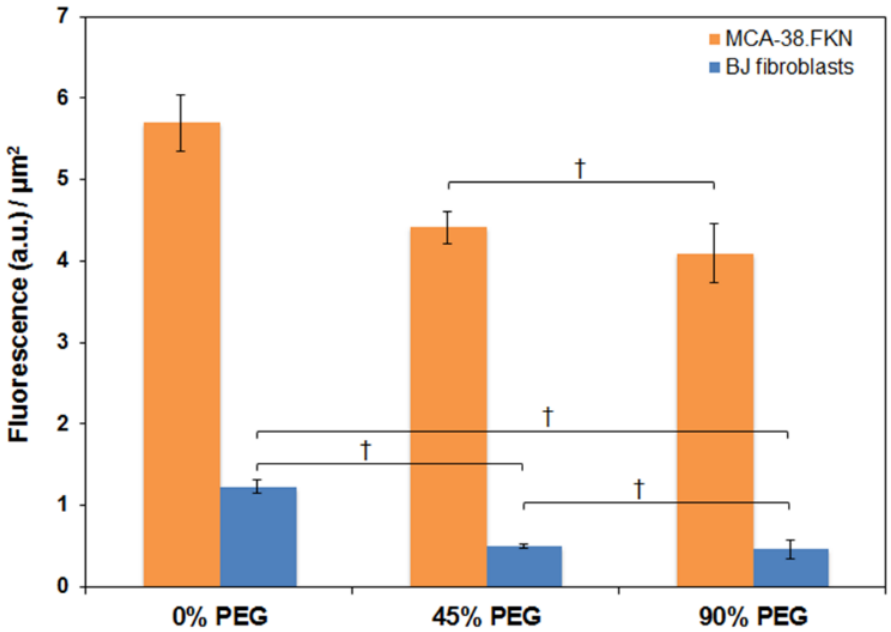

Figure 2.8. Binding and internalization of FKN-S2-T_{10} micelles with different amounts of PEG_{5000} by MCA-38.FKN and BJ fibroblasts after 24 h at 37 °C. Fluorescence was normalized to cell area. Data are presented as mean±SE (n=3). A two-way ANOVA with Tukey's HSD post-hoc analysis indicated that all pairs showed significant statistical difference ($p<0.05$) with the exception of the ones with † ($p>0.05$).

The presence of free aptamer decreased binding of PEGylated FKN-S2-T_{10} micelles to MCA-38.FKN cells by 50%, showing effective blocking (Figure 2.9). Confocal microscopy was performed on MCA-38.FKN and BJ fibroblasts incubated with PEGylated FKN-S2-T_{10} micelles to determine the extent of binding and internalization for each cell type. The MCA-38.FKN cells (Figure 2.10A) showed high amounts of micelle internalization, while the BJ fibroblasts (Figure 2.10B) showed mainly surface binding with minimal micelle internalization. In the MCA-38.FKN cells the micelles were present in both the cytosol and acidic organelles, but were mainly distinct from the early endosomes (Figure 2.11).

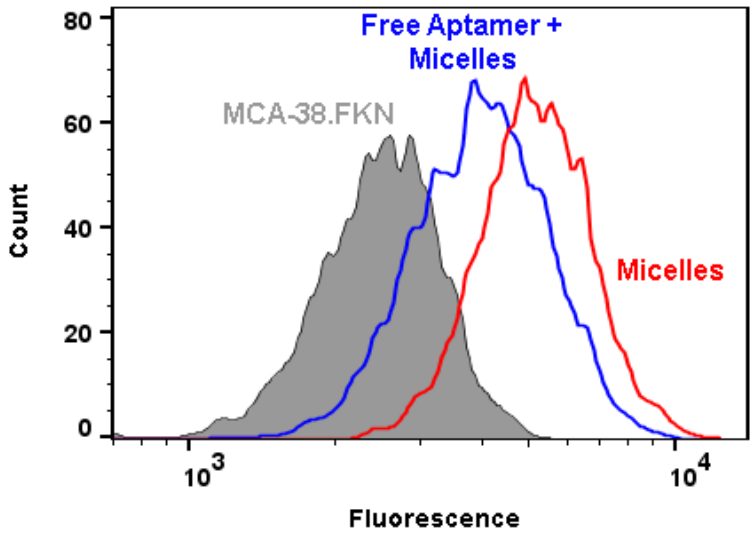

Figure 2.9. Blocking of FKN-S2-T_{10} micelles in the presence of free FKN-S2-T_{10} aptamer. The micelles were composed of 20 mol% HEX-labeled FKN-S2-T_{10} aptamer-amphiphiles, 40 mol% PEGylated FKN-S2-T_{10} aptamer-amphiphiles and 40 mol% FKN-S2-T_{10} aptamer-amphiphiles. MCA-38.FKN cells were blocked with free FKN-S2-T_{10} aptamer for 1 h at 4 °C, followed by incubation with the micelles for an additional 1 h at 4 °C.

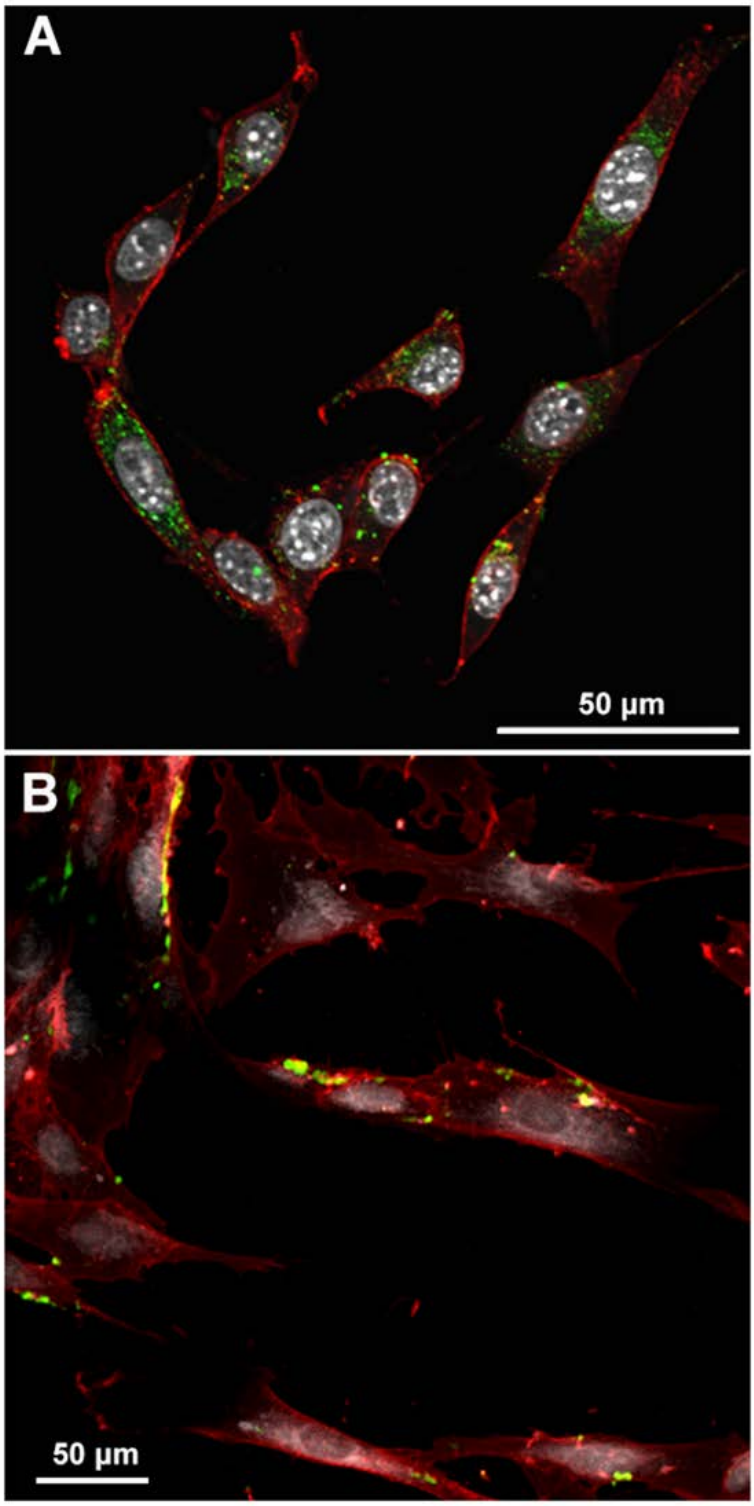

Figure 2.10. Confocal microscopy of PEGylated FKN-S2-T_{10} micelles incubated for 24 h at 37 °C with (A) MCA-38.FKN cells, or (B) BJ fibroblasts. Micelles are shown in green, nuclei in gray and cell membranes in red.

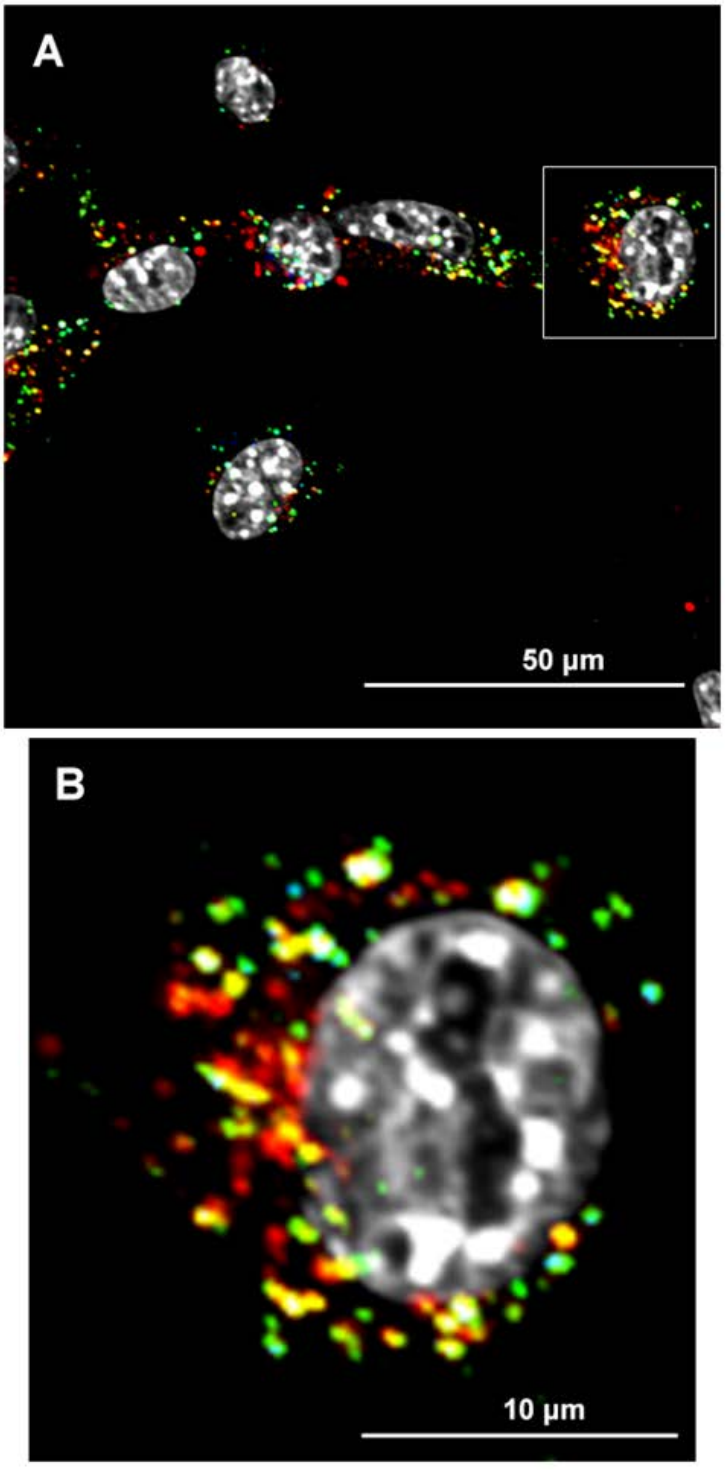

Figure 2.11. (A) Intracellular distribution of PEGylated FKN-S2-T_{10} micelles in MCA-38.FKN cells. (B) Zoom in of the square area shown in A. Micelles are shown in red, early endosomes in blue, acidic organelles in green and nuclei in gray.

Cell binding and internalization of PEGylated FKN-S2-T_{10} micelles by HCoEpiC that did not express fractalkine (Figure 2.7C) was also examined. HCoEpiC showed minimal cell association via flow cytometry compared to MCA-38.FKN cells (Figure 2.12A), and minimal surface binding with no internalization via confocal microscopy (Figure 2.12B).

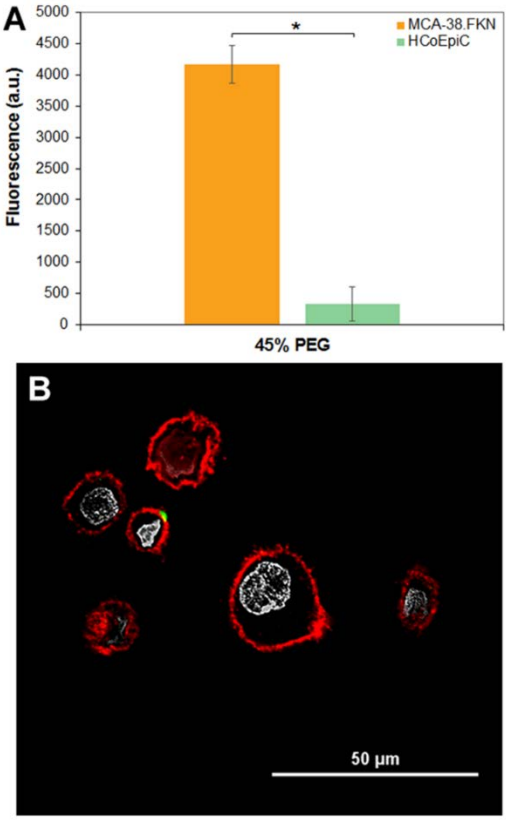

Figure 2.12. (A) Binding and internalization of PEGylated FKN-S2-T_{10} micelles by HCoEpiC after 24 h at 37 °C. Data are presented as mean±SE (n=3). Student's t-test analysis was used to determine significance, * $p<0.001$. (B) Confocal microscopy of PEGylated FKN-S2-T_{10} micelles incubated for 24 h at 37 °C with HCoEpiC. Micelles are shown in green, nuclei in gray and cell membranes in red.

2.4.3 Micelle Stability to Serum and Nucleases

The stability to serum and nucleases was investigated for the PEGylated FKN-S2-T_{10} and PEGylated control micelles that were used for the *in vivo* studies. Non-PEGylated FKN-S2-T_{10} micelles were also used as a control to test the effect of PEG_{5000}. All micelles

contained HEX-labeled ssDNA-amphiphiles that gave rise to the micelle signal in the gels. The micelles were exposed to 1X PBS, 10% FBS in water to mimic *in vitro* conditions, and 90% FBS in water to mimic *in vivo* conditions, for 24 h at 37 °C (Figure 2.13). Controls without micelles were also included to capture the autofluorescence of serum proteins. Upon exposure to 10% and 90% FBS the micelle band decreased and shifted upwards, even in the presence of PEG, and the band associated with serum proteins became stronger, for all micelles. Comparison between the PEGylated FKN-S2-T_{10} micelles and PEGylated control micelles showed that the micelle band was stronger, and the serum band was weaker for the PEGylated control micelles in the presence of 90% FBS. The stability of micelles to DNase I (Figure 2.14) and exonuclease III (Figure 2.15) at 0-5 U/mL for 24 h at 37 °C was also examined, and all micelles were stable at all concentrations for both nucleases.

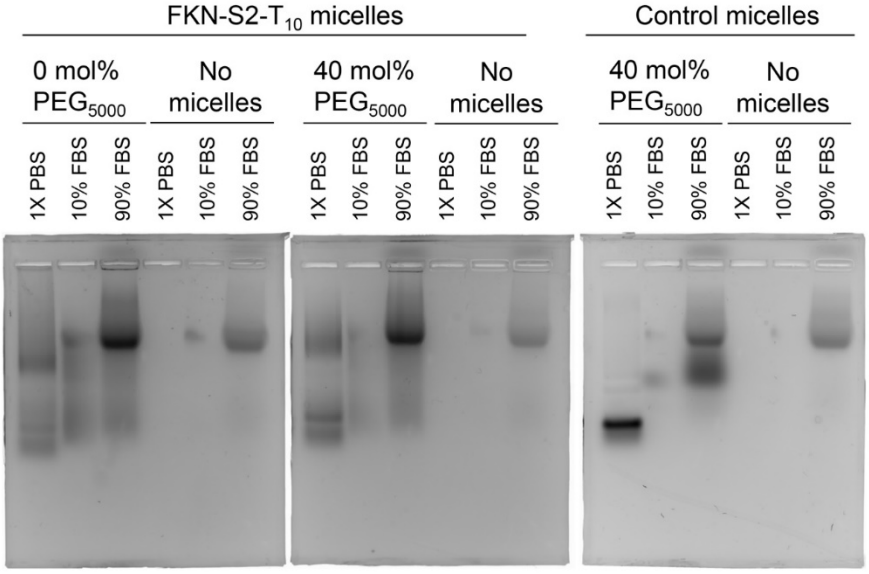

Figure 2.13. Gel analysis of ssDNA micelles incubated at 37 °C for 24 h in 1X PBS, 10% (v/v) FBS in water to mimic *in vitro* conditions, and 90% (v/v) FBS in water to mimic *in vivo* conditions. Controls without micelles were also included to capture the autofluorescence of serum proteins. All formulations had 20 mol% HEX-labeled ssDNA-amphiphiles that gave rise to the micelle signal.

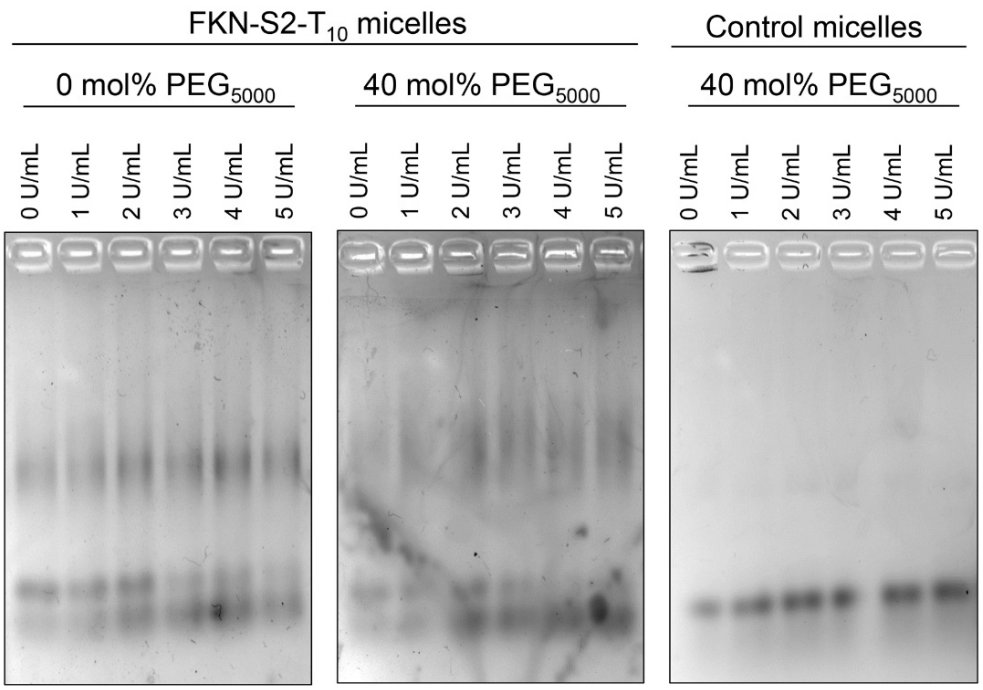

Figure 2.14. Gel analysis of ssDNA micelles incubated with 0-5 U/mL DNase I at 37 °C for 24 h. All formulations had 20 mol% HEX-labeled ssDNA-amphiphiles that gave rise to the micelle signal.

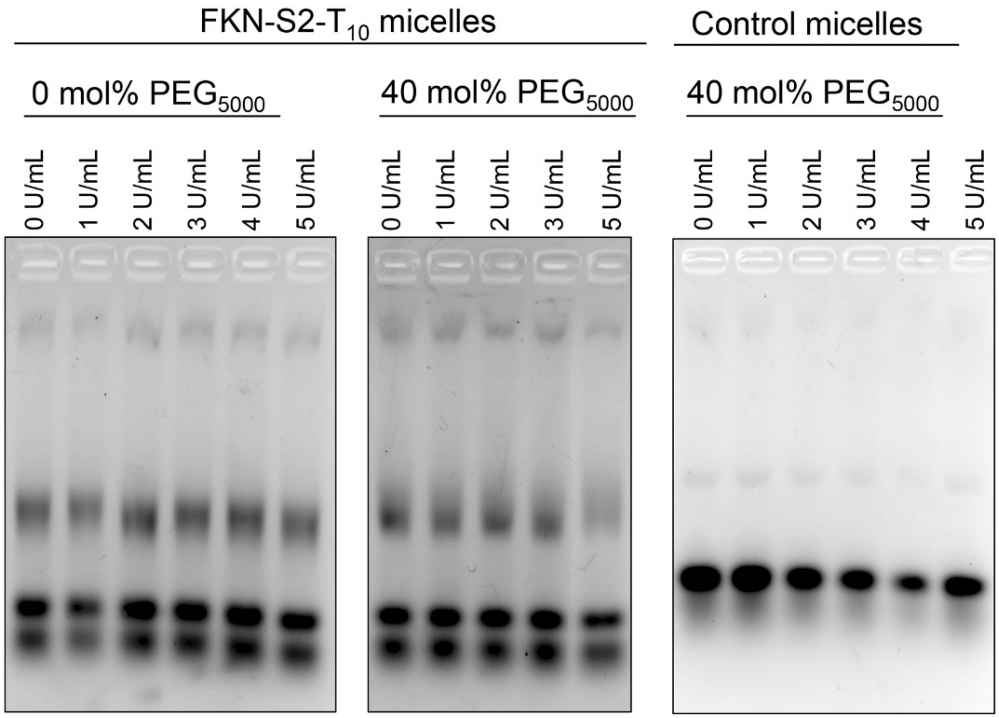

Figure 2.15. Gel analysis of ssDNA micelles incubated with 0-5 U/mL exonuclease III at 37 °C for 24 h. All formulations had 20 mol% HEX-labeled ssDNA-amphiphiles that gave rise to the micelle signal.

2.4.4 Biodistribution and Tumor Internalization of Micelles in an Animal Model

The biodistribution of PEGylated FKN-S2-T_{10} micelles and PEGylated control micelles was determined *in vivo* using µPET/CT. DOTA-labeled ssDNA-amphiphiles was used to chelate ^{64}Cu. DOTA labeling has been shown to have a minor effect on the size and surface charge of nanoparticles.[131, 132] DOTA-labeled amphiphiles were present in approximately 1,850X molar excess of ^{64}Cu in order to chelate all added ^{64}Cu. This was demonstrated by showing that copper was chelated by DOTA-labeled ssDNA micelles when DOTA was present at 5X-10X molar excess (Figure 2.16).

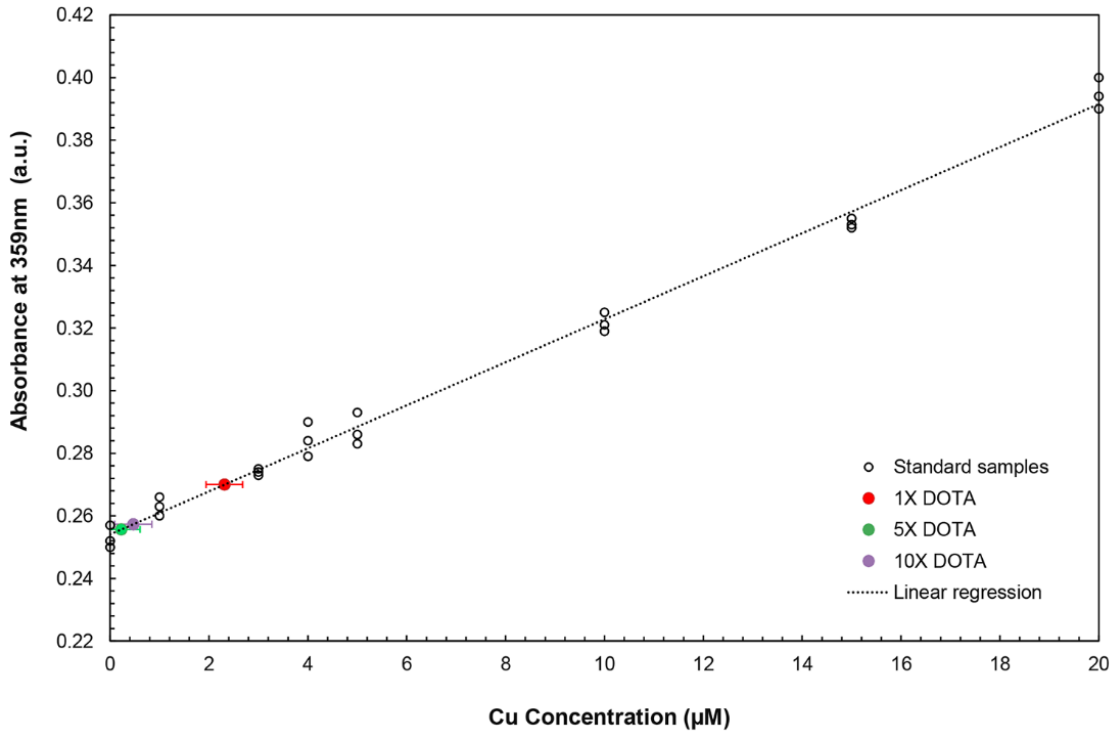

Figure 2.16. Concentration of unchelated Cu^{2+} remaining in solution after treatment with DOTA-labeled ssDNA micelles (present at 1X, 5X, and 10X molar excess of Cu^{2+}), as determined by the calibration curve. The micelles were composed of 5 mol% DOTA-labeled FKN-S2-T_{10}-amphiphiles, 47.5 mol% PEGylated FKN-S2-T_{10}-amphiphiles, and 47.5% FKN-S2-T_{10}-amphiphiles. Data are presented as mean ± SE (n=3). For the *in vivo* studies, ^{64}Cu-labeled micelle solutions contained approximately 1,850X molar excess of DOTA to ^{64}Cu.

Representative μPET/CT three-dimensional volume renderings of mice at 1, 3 and 24 h are shown in Figure 2.17A (not adjusted for ^{64}Cu decay), while the *in vivo* biodistribution of the PEGylated FKN-S2-T_{10} and control micelles from the μPET images is plotted for each organ in Figure 2.17B. As shown in Figure 2.17B there was no statistically significant difference between the PEGylated FKN-S2-T_{10} and PEGylated control micelles for most organs within a given time point. The biodistribution of the PEGylated FKN-S2-T_{10} micelles over time showed no statistical difference between 1 and 3 h, with the exception of pancreas, or between 1 and 24 h, with the exception of liver. However, for many organs the 3 h time point was statistically higher than 24 h, thus showing a point of high accumulation between 1 and 3h and a decline after that. Similarly, the biodistribution of the PEGylated control micelles over time showed no statistical difference between 1 and 3 h, or 1 and 24 h for most organs. The PEGylated control micelles showed higher accumulation at 3 h compared to 24 h only for some organs (skin, liver, lungs and bladder) though. There was no statistically significant difference in the accumulation of the PEGylated FKN-S2-T_{10} or control micelles in the tumor over time.

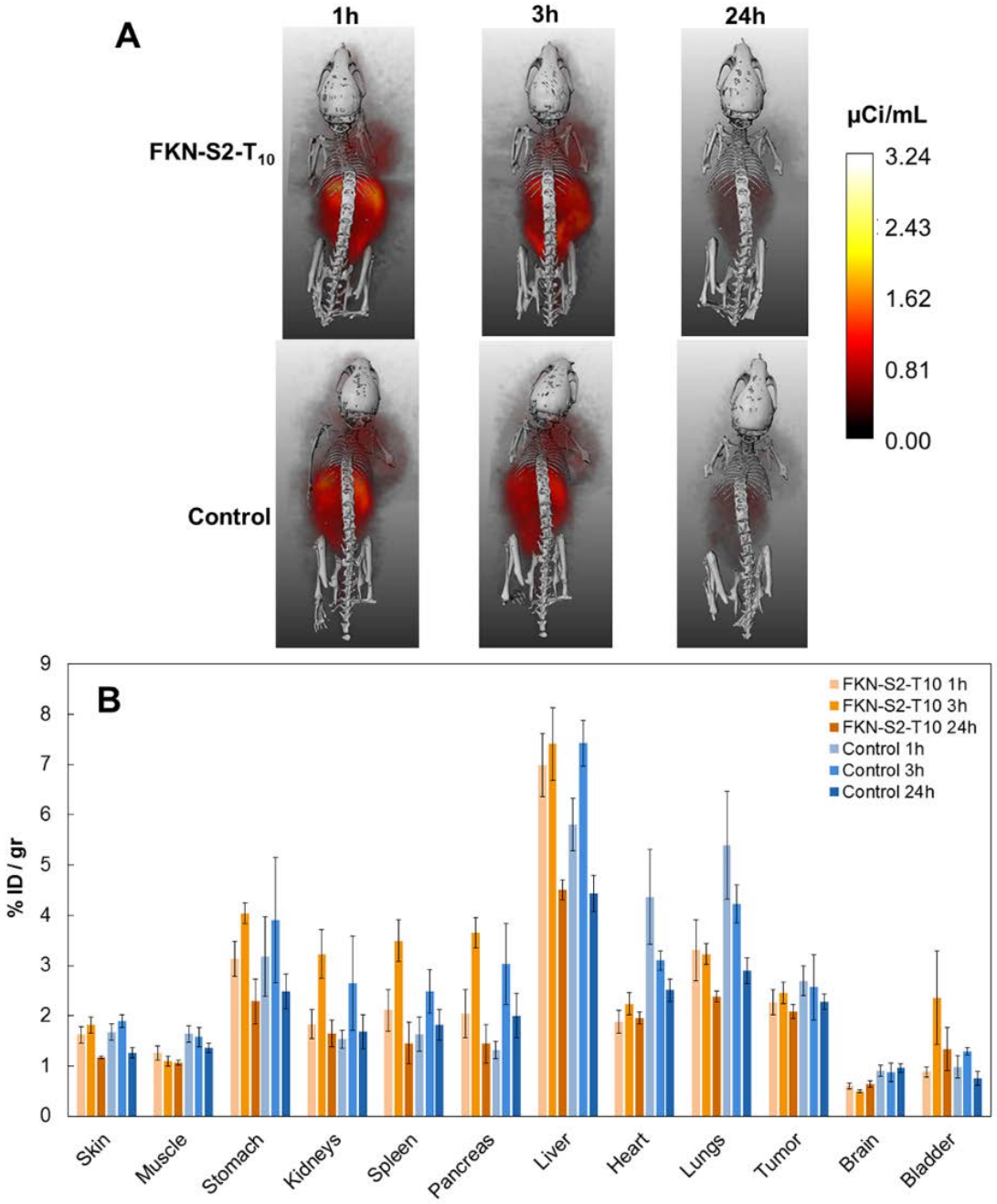

Figure 2.17. (A) Representative mice with subcutaneous MCA-38.FKN tumors shown as three-dimensional volume renderings of coronal µPET (orange) overlaid on CT images (gray) at 1, 3 and 24 h after intravenous tail injection of ^{64}Cu-DOTA-labeled PEGylated FKN-S2-T_{10} micelles (top), or ^{64}Cu-DOTA-labeled PEGylated control micelles (bottom). (B) Biodistribution of micelles at 1, 3 and 24 h post injection from µPET images. Data were adjusted for ^{64}Cu decay and plotted as mean±SE (n=3-6). P-values from student's t-test analysis can be found in Table 2.3.

Table 2.3 P-values from the student's t-test analysis of *in vivo* biodistribution data for ^{64}Cu-DOTA-labeled PEGylated FKN-S2-T_{10} or control micelles at 1, 3, and 24 h post intravenous tail injection, shown in Figure 2.17B.

Comparison between FKN-S2-T_{10} and control micelles

Organ	1h	3h	24h
Skin	>0.05	>0.05	>0.05
Muscle	>0.05	>0.05	<0.05
Stomach	>0.05	>0.05	>0.05
Kidneys	>0.05	>0.05	>0.05
Spleen	>0.05	>0.05	>0.05
Pancreas	>0.05	>0.05	>0.05
Liver	>0.05	>0.05	>0.05
Heart	<0.05	<0.05	>0.05
Lungs	>0.05	>0.05	>0.05
Tumor	>0.05	>0.05	>0.05
Brain	<0.05	>0.05	<0.05
Bladder	>0.05	>0.05	>0.05

Comparison between FKN-S2-T_{10} micelles at different times

Organ	1h & 3h	1h & 24 h	3h & 24 h
Skin	>0.05	<0.05	<0.05
Muscle	>0.05	>0.05	>0.05
Stomach	>0.05	>0.05	<0.05
Kidneys	>0.05	>0.05	<0.05
Spleen	>0.05	>0.05	<0.05
Pancreas	<0.05	>0.05	<0.05
Liver	>0.05	<0.05	<0.05
Heart	>0.05	>0.05	>0.05
Lungs	>0.05	>0.05	<0.05
Tumor	>0.05	>0.05	>0.05
Brain	>0.05	>0.05	>0.05
Bladder	>0.05	>0.05	>0.05

Comparison between control micelles at different times

Organ	1h & 3h	1h & 24 h	3h & 24 h
Skin	>0.05	>0.05	<0.05
Muscle	>0.05	>0.05	>0.05
Stomach	>0.05	>0.05	>0.05
Kidneys	>0.05	>0.05	>0.05
Spleen	>0.05	>0.05	>0.05
Pancreas	>0.05	>0.05	>0.05
Liver	>0.05	>0.05	<0.05
Heart	>0.05	>0.05	>0.05
Lungs	>0.05	>0.05	<0.05
Tumor	>0.05	>0.05	>0.05
Brain	>0.05	>0.05	>0.05
Bladder	>0.05	>0.05	<0.05

The ex vivo biodistribution data at 24 h in Figure 2.18 showed no statistically significant difference between the PEGylated FKN-S2-T_{10} and PEGylated control micelles for any organ measured, with the exception of blood where control micelles were present more than the FKN-S2-T_{10} micelles. Tumor delivery was approximately 4% ID/gr for both micelles, and the organs with the highest delivery at 24 h were the liver and kidneys for both nanoparticles. In contrast, the *in vivo* biodistribution (Figure 2.17B) showed the liver as the only organ with high accumulation at 24 h.

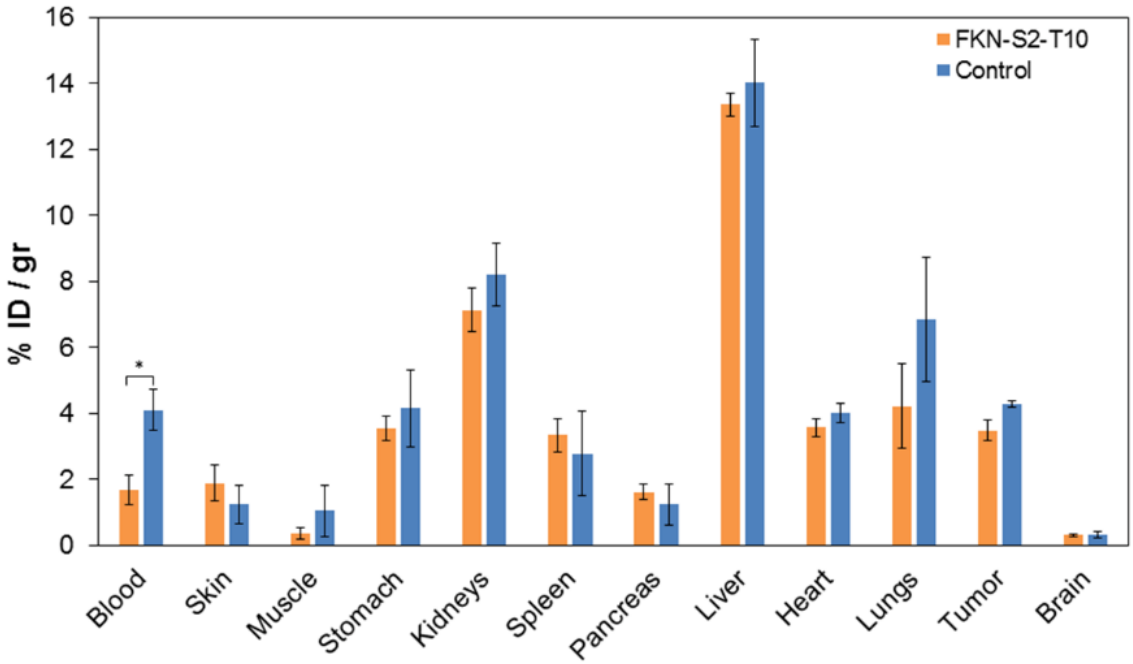

Figure 2.18. Ex vivo biodistribution of ^{64}Cu-DOTA-labeled PEGylated FKN-S2-T_{10} micelles or ^{64}Cu-DOTA-labeled PEGylated control micelles, in MCA-38.FKN tumor-bearing mice, 24 h post intravenous tail injection. Data were adjusted for ^{64}Cu decay and plotted as mean±SE (n=4-5). Student's t-test analysis was used to determine significance, * $p<0.05$. There was no significant statistical difference for pairs without brackets.

We hypothesized that although tumor uptake was similar between the PEGylated FKN-S2-T_{10} and control micelles, only the FKN-S2-T_{10} micelles internalized into the tumor cells. Figure 2.19 shows confocal microscopy images of MCA-38.FKN tumor sections 24 h post

intravenous tail injection of FAM-labeled PEGylated FKN-S2-T_{10} and PEGylated control micelles. The PEGylated FKN-S2-T_{10} micelles showed significant internalization by the tumor cells and colocalization with the nuclei, while the PEGylated control micelles were mainly located on the extracellular space or associated with the cell membrane.

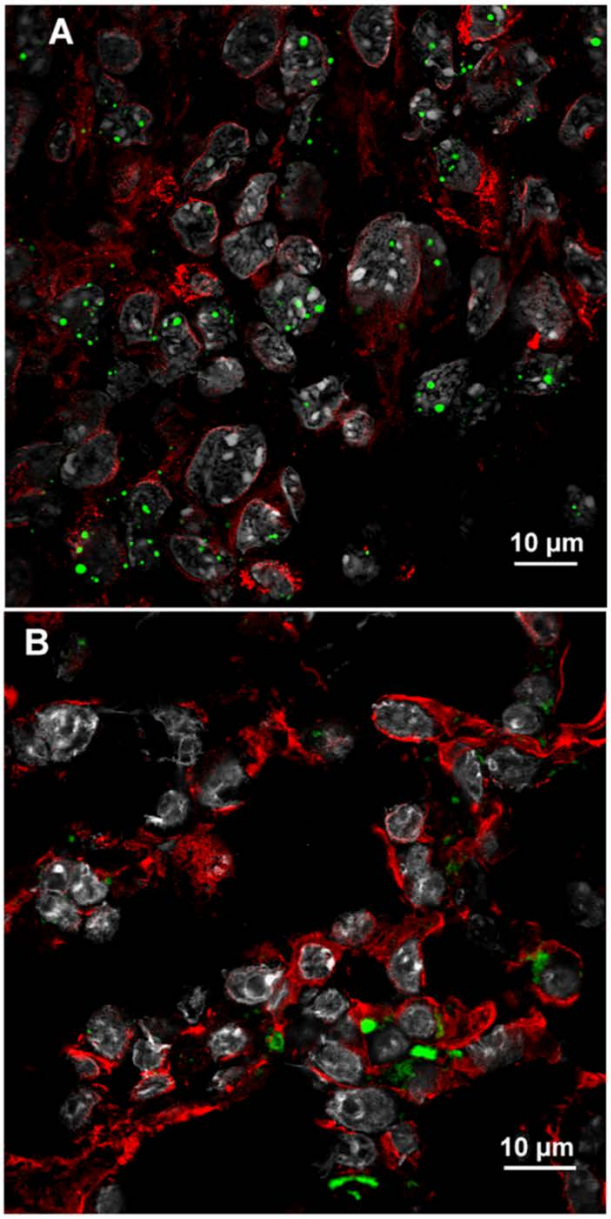

Figure 2.19. Confocal microscopy of tumor sections 24 h post intravenous tail injection of (A) FAM-labeled PEGylated FKN-S2-T_{10} micelles, or (B) FAM-labeled PEGylated control micelles. Membranes are shown in red, nuclei in gray and micelles in green.

2.5 Discussion

In this report, we used FKN-S2-T_{10} aptamer-amphiphiles to create micelles that could target fractalkine-expressing cancer cells. The micelles were decorated with PEG_{5000}, as PEG has been shown to decrease nanoparticle immunogenicity and increase blood circulation time, which improves tumor accumulation.[133, 134] Cryo-TEM revealed that the FKN-S2-T_{10} aptamer-amphiphiles self-assembled in weakly ellipsoidal micelles, as has been observed before for ssDNA-amphiphiles that form G-quadruplexes.[135] The difference in micelle diameters between cryo-TEM and DLS is attributed to the fact that electron contrast in TEM derives mostly from the core,[136, 137] while DLS reports the hydrodynamic diameter of the spheres that is larger than their true diameter. Therefore, it is likely that the actual diameter of the micelles falls between 12 and 22 nm.

MCA-38.FKN cells and BJ fibroblasts were used initially to determine the effect of PEGylation on the binding and internalization ability of the micelles. FKN-S2-T_{10} micelles (PEGylated or not) associated at higher numbers with fractalkine-expressing MCA-38.FKN cells compared to BJ fibroblasts that did not express fractalkine. PEGylation decreased binding of the FKN-S2-T_{10} micelles to MCA-38.FKN cells, but the amount of PEGylation (45 or 90 mol%) did not make a difference. In contrast, the non-specific binding of FKN-S2-T_{10} micelles to BJ fibroblasts was unaffected by PEG. Although the non-PEGylated micelles showed the highest binding and internalization when delivered to the MCA-38.FKN cells, micelles with partial PEGylation were selected for further experiments to take advantage of the advantages PEG confers to nanoparticles. PEGylated

FKN-S2-T_{10} micelles were also evaluated with HCoEpiC and showed minimal cell association compared to MCA-38.FKN cells.

Confocal imaging was performed to determine the extent of internalization versus non-specific membrane association for the healthy and tumor cells. After 24 h, membrane-associated cell binding was mainly observed for the BJ fibroblasts and HCoEpiC, while the MCA-38.FKN cells internalized the micelles to a much greater extent. The micelles were mainly found free in the cytosol of MCA-38.FKN cells, with some colocalization with acidic organelles. The results of confocal microscopy and blocking experiment performed in the presence of free aptamer, suggested that the PEGylated FKN-S2-T_{10} micelles bound and internalized to fractalkine-expressing cells in a specific manner, in agreement with previous work showing that the FKN-S2 aptamer bound to fractalkine with high affinity and specificity.[103]

The stability of the PEGylated FKN-S2-T_{10} and control micelles was evaluated in the presence of serum and nucleases after 24 h. Gel experiments suggested that serum proteins adsorbed onto the micelles, even in the presence of partial PEGylation, desorbing amphiphiles from the micelles. These results were in agreement with findings from the literature, where it was shown that the main mechanism of serum degradation for PEGylated ssDNA-gold nanoparticles was protein-mediated strand desorption and 3'-exonucleases.[123] It was also shown that 5'-exonucleases did not play a significant role in ssDNA breakdown, and PEG_{5000} protected the nanoparticles from aggregation mediated by serum proteins.[123] Protein adsorption and amphiphile desorption from the micelles

appeared weaker in the case of PEGylated control micelles, in agreement with previous work showing that poly-T ssDNA sequences bound less serum proteins than G-rich ssDNA.[138] The stability of micelles to endonuclease DNase I and exonuclease III was also evaluated. Exonuclease III was used as, in addition to the 3'-hydroxyl termini of double-stranded DNA, it was shown to be active towards the 3'-end of ssDNA,[139] and we wanted to examine if 3'-end conjugation of the ssDNA to the tail provided protection from 3'-exonucleases. Results showed that all micelles were stable to both nucleases for all concentrations tested (0-5 U/mL). In fact, it was demonstrated in the literature that 50 U/mL of DNase I was needed for degradation of ssDNA on gold nanoparticles protected by PEGylation, which was 500 times higher than the physiological mouse serum concentration of DNase I (0.1 U/mL).[123] It should be noted that the average DNase I concentration in the blood plasma of healthy humans was 0.356±0.410 U/mL, while a decrease in DNase I activity below detection level was reported for colon cancer patients.[140] Our results also demonstrated that both PEGylated and non-PEGylated FKN-S2-T_{10} micelles were stable to both nucleases, as it was shown in the literature that steric hindrance through dense ssDNA packing in a micelle corona limits accessibility of nucleases.[139]

The biodistribution of PEGylated FKN-S2-T_{10} and control micelles was investigated and results showed that absolute values between *in vivo* and ex vivo biodistribution data were different reflecting the different approaches of these two methods.[141] For example, small differences in the perceived border of an organ in CT could result in large differences in radioactivity, while differences in blood flow before and after euthanasia can lead to

differences in measured radiation. From the time points examined through μPET images, there seemed to be a peak retention time between 1 and 3 h and a decline after that for most organs for the aptamer micelles. Similar to most intravenously injected nanoparticles, a prominent liver uptake of both micelles was detected at all times examined though μPET, which declined over time. The PEGylated control micelles though were present at higher amounts in heart, which is a highly perfused organ, at 1 and 3 h compared to PEGylated FKN-S2-T_{10} micelles. This result, along with the presence of more control micelles in the blood at 24 h in the ex vivo biodistribution data, suggested that the control micelles remained in blood circulation more than the aptamer micelles. Even though both micelles had the same PEGylation, the difference may lie in the actual ssDNA sequence of the micelles. Our serum stability results suggested that serum proteins adsorbed less on the PEGylated control micelles that lacked guanines, in agreement with previous findings in the literature.[138] Thus, binding of a higher amount of opsonins on the surface of PEGylated FKN-S2-T_{10} micelles compared to the control micelles was possible, which could be followed by phagocytosis and rapid clearance from the blood stream.[142]

The ex vivo biodistribution results at 24 h showed no statistically significant difference between the micelles for any organ measured, with the exception of blood for the control micelles. The lack of statistical differences between the two groups is not surprising, as biodistribution depends on the size, charge and shape of the nanoparticle.[94, 98] The excised organs with the highest delivery were the liver and kidneys for both nanoparticles. The nature of the kidney accumulation was not clear, as nanoparticles smaller than our micelles (<10 nm in diameter) experience renal clearance.[143] Kidney radioactivity is unlikely to be

due to the presence of free copper, either from unchelated copper or copper released *in vivo* due to kinetic instability of ^{64}Cu-DOTA complexes, as copper accumulates mainly in the liver.[125, 144] However, ^{64}Cu-DOTA complexes accumulate in the kidneys,[131] and therefore the presence of desorbed radiolabeled amphiphiles may be a possible explanation for the kidney accumulation for both micelles.

Tumor delivery at 24 h post injection was approximately 4% ID/gr for both the aptamer and control micelles, similar to tumor accumulation observed by other micelles.[125, 145] There was no statistically significant difference in the accumulation of PEGylated FKN-S2-T_{10} or control micelles in the tumor over time from the μPET images, or at 24 h based on values of excised tumors. However, confocal imaging of tumors demonstrated that PEGylated FKN-S2-T_{10} micelles internalized into the MCA-38.FKN cells while PEGylated control micelles did not. In particular, there was significant colocalization of the targeted micelles with the nuclei. In contrast, the control micelles were mainly located on the extracellular space or associated with the cell membrane. This showed that both micelles were able to extravasate and enter the tumor independent of the ssDNA sequence used, but were only able to internalize into the fractalkine-expressing tumor cells when they were composed of the FKN-S2-T_{10} aptamer-amphiphile. Our results were consistent with literature reports showing that targeting did not help in tumor accumulation or retention over time, as both targeted and non-targeted PEGylated nanoparticles demonstrated nearly identical tumor localization kinetics and accumulation after 24 h.[131, 146] Instead, it was shown that targeting contributed to enhanced internalization by the tumor cells.[147]

In conclusion, we have shown for the first time the development, characterization and targeting efficacy of PEGylated FKN-S2-T_{10} micelles for human fractalkine *in vitro* and *in vivo*. Partial PEGylation minimized non-specific interactions with healthy cells without compromising the secondary structure of the aptamer, or binding and internalization into fractalkine-expressing colon cancer cells. Serum adsorption was observed that may have contributed to amphiphile desorption from the micelles, but both aptamer and control micelles were highly resistant to nucleases. *In vivo* biodistribution of PEGylated FKN-S2-T_{10} and control micelles showed that tumor uptake was independent of the ssDNA sequence, but the aptamer was required for binding and internalization into the fractalkine-expressing tumor cells *in vivo*.

2.6 Acknowledgements

Portions of this work were completed by Tim Pearce, PhD, who is a co-first author of the paper from which this chapter was adapted.[93] μPET/CT images were recorded with the assistance of Kristin Mathson and analyzed with the assistance of Thomas Pengo at the University of Minnesota Informatics Institute.

3 Delivery of ssDNA-Amphiphile Nanotubes to Glioblastoma Multiforme

3.1 Summary

In this work, we evaluated the ability of nanotubes made out of guanine-rich self-assembled ssDNA-amphiphiles to bind and internalize to GL261 mouse glioblastoma cells. Stability tests showed that the nanotubes did not degrade when exposed to 10% or 85% serum, or nucleases for 24 h. Confocal microscopy images showed that after 24 h, the nanotubes internalized by GL261 cells but not by C8-D1A healthy mouse astrocytes. For comparison, spherical micelles made out of the same ssDNA-amphiphiles did not internalize to either GL261 or C8-D1A cells. Intracellular trafficking analysis showed that the nanotubes internalized to GL261 by endocytosis, and after 24 h they were found in endosomes, lysosomes and free in the cytosol. Delivery of the nanotubes was also investigated *in vivo* in an orthotopic GL261-bearing mouse model. Direct brain injections of the nanotubes showed only the side of the brain with the tumor retained the nanotubes, while the nanotubes were not visible in the healthy tissue. *In vivo* biodistribution of the nanotubes after their systemic delivery also showed high brain accumulation, thus demonstrating their promise as a drug delivery vehicle for glioblastoma.

3.2 Introduction

Targeted drug delivery vehicles have become a promising field for delivery of therapeutics to brain cancers. Tumor targeting in general is aided by the enhanced permeability and retention (EPR) effect,[2] but targeting of the brain is made more difficult by the blood-brain-barrier (BBB), which acts to limit the transport of large-molecule drugs to the brain.[148]

Glioblastoma multiforme (GBM) is the most malignant type of primary brain tumor. Despite treatment through neurosurgery, radiation, and chemotherapy, long-term survival remains low. GBM has been shown to increase the permeability of the BBB,[149-151] which combined with the EPR effect can help in the development of new treatment options.

The delivery of nanoparticles to the brain as carriers for therapeutics is promising. The field of polymeric and liposomal nanoparticles is well developed, and both types of nanoparticles have been used extensively as delivery vehicles to the brain.[152, 153] However, typical accumulation of targeted liposomal or polymeric nanoparticles 24 h after systemic injection are often lower than 0.5 percent injected dose per gram of tissue (%ID/g).[154, 155] It is therefore important to improve the accumulation of the nanoparticle delivery vehicle in the brain tissue so that more therapeutic can reach the tumor.

Several options exist for increasing the accumulation of nanoparticles to their intended location. Targeting through the attachment of small-molecule peptides,[156-158] antibodies,[111, 159, 160] or aptamers[161, 162] has been shown to improve the retention of nanoparticles when delivered to GBM. The addition of poly (ethylene glycol) to nanoparticles has been shown to improve delivery and accumulation by improving the blood circulation and immunogenic properties of the nanoparticles,[130, 163] thereby allowing for better accumulation by increasing the time exposed to the intended target. The shape and aspect ratio of a nanoparticle can also influence its cell association. In low Reynolds number flows, such as the blood capillaries, elongated particles align with the fluid flow in a phenomenon known as shear alignment. In the presence of targeting antibodies, this leads

to better retention of nanorods compared to nanospheres in the brain endothelium, with the targeted nanorods showing more than seven times greater brain uptake than targeted nanospheres of the same volume.[71] Even in the absence of targeting, the internalization of positively charged hydrogel rod-like high-aspect-ratio nanoparticles was much more rapid and efficient than the internalization of particles of equal volume with an aspect ratio of one, showing the effect of shape on cell internalization.[164]

Off-targeting effects also need to be minimized when delivering toxic loads. Therefore, it is important for nanoparticles to have varied uptake between cell types to increase delivery to target cells while limiting off-targeting to healthy cells. It has been shown that for non-targeted nanoparticles, larger-sized negatively charged hydrogel nanodiscs and nanorods lead to better cellular internalization than their smaller counterparts.[72] It was also shown that cell lines have differential preferences for internalizing nanodiscs or nanorods by using different pathways.[72] This suggests that it is possible to identify nanoparticles whose intrinsic shape and size may allow for preferential accumulation in cancerous cells as compared to healthy cells.

Single-walled carbon nanotubes functionalized with targeting moieties, such as small peptides or monoclonal antibodies, have been utilized to selectively target glioblastoma cells.[165, 166] When delivered systemically through the tail vein to subcutaneous human glioblastoma xenograft tumors, these nanotubes showed efficient uptake by the subcutaneous glioblastoma tumors, but low overall brain accumulation,[165] while *in vitro* studies showed that selective targeting via antibody incorporation can lead to effective cell

death whereby the targeted nanotubes can be used to induce photothermolysis of the targeted cells.[166] Multi-walled carbon nanotubes have also shown effective cell targeting when functionalized with a BBB-crossing peptide, leading to the efficient delivery of doxorubicin and prolonged survival rates of mice bearing orthotopic glioblastoma tumors.[167]

DNA nanotechnology is a growing field that allows for the creation of custom-designed nanoparticles. DNA origami[168] and DNA tile assembly[169] are two methods that allow for the assembly of specific nanoparticle structures composed solely of DNA molecules. Both techniques have been utilized to create DNA nanotubes that can deliver to cells *in vitro* and *in vivo*.[170-174] It was shown that nanotubes made from tile assembly are internalized by immune cells, human cervical cancer cells, and nasopharyngeal epidermal carcinoma cells when targeted with either CpG sequences or folic acid.[170-172] These tile-assembled nanotubes are more resistant to degradation than free ssDNA or double-stranded DNA (dsDNA) plasmids when exposed to serum conditions that mimic the *in vivo* environment [170, 171]. These nanotubes can also be used to deliver therapeutic loads such as small interfering RNA (siRNA).[171] Nanotubes assembled in a tile-like manner also showed increased resistance to degradation when incubated with serum compared to a short oligonucleotide dsDNA sequence.[173] These tile-like nanotubes also showed higher cellular internalization than free dsDNA molecules when delivered to human cervical cancer cells.[173] DNA origami nanotubes have also been used to deliver doxorubicin to human breast cancer cells, where the origami nanotubes with doxorubicin showed higher cell death than free doxorubicin delivered alone.[174] A major limitation of both DNA origami and

DNA tile assembly is that they require precise solvent and thermal conditions to allow for DNA annealing and often require computer-aided design to develop the required DNA sequences needed to achieve certain structures. It was shown that the sodium concentration available in 1X PBS is not sufficient to stabilize tile-assembled DNA nanotubes and that more than 4 mM Mg^{2+} was necessary to stabilize the structures.[171]

Taking inspiration from the lipid and peptide-amphiphile self-assembly literature, we have previously developed ssDNA-amphiphiles that are capable of self-assembling in aqueous solution into spherical micelles, nanotapes and nanotubes. These amphiphiles consist of three main sections, a ssDNA hydrophilic headgroup, a C_{16} dialkyl hydrophobic tail, and a spacer used to separate the two other sections. We have shown that in the presence of a hydrocarbon spacer, spherical micelles and nanotubes with varying lengths can form from ssDNA-amphiphiles in aqueous solution.[23, 24] One amphiphile in particular was identified as forming short ssDNA nanotubes in large quantities. This amphiphile consists of a ten nucleotide (nt) ssDNA headgroup containing five consecutive guanine (G) repeats attached to a dialkyl tail using a C_{12} hydrocarbon spacer. The structures formed from this amphiphile will be referenced as nanotubes or micelles for the remainder of this work.

In this work we investigate the uptake of ssDNA nanotubes by the model mouse glioblastoma GL261 cell line without the addition of a targeting moiety. Using size exclusion chromatography, we separated the self-assembled nanoparticles based on their size, creating samples containing only self-assembled nanotubes or micelles. The serum and nuclease stability of the nanotubes was investigated to show they are resistant to

degradation in different culture conditions. The nanotubes and micelles were delivered to GL261 cells and imaged with confocal microscopy to demonstrate the preferential uptake of the nanotubes to glioblastoma cells. Further internalization experiments were used to determine the internalization pathways utilized by the nanotubes during cellular uptake. *In vivo* experiments using an orthotopic GL261 tumor model investigated the retention of nanotubes after direct brain injections as well as the biodistribution over time after systemic tail-vein injections via micro positron emission tomography (μPET)/computerized tomography (CT) and ex vivo organ analysis. Here were report the uptake of ssDNA nanotubes by GL261 cells based on the size characteristics of the nanoparticles as well as high overall brain accumulation by the nanotubes using *in vivo* models.

3.3 Materials and Methods

3.3.1 Materials

All materials were purchased from Sigma Aldrich and used without further purification or modification unless otherwise stated. Buffers include high performance liquid chromatography (HPLC) buffer A (100 mM hexafluoroisopropanol and 15 mM triethylamine in water), HPLC buffer B (100 mM hexafluoroisopropanol and 15 mM triethylamine in methanol), TEAA buffer (50% molar basis triethylamine, 50% molar basis glacial acetic acid, pH = 7.0), Cu-TBTA (10 mM Copper (II)-Tris[(1-benzyl-1H-1,2,3-triazol-4-yl)methyl]amine) in 55% dimethyl sulfoxide (DMSO), 45% water), 1X phosphate buffered saline (PBS) (137 mM sodium chloride, 2.7 mM potassium chloride, 10 mM disodium phosphate, 1.8 mM monopotassium phosphate in water, pH = 7.4), and

1X TAE (40 mM tris(hydroxymethyl)aminomethane, 20 mM acetic acid, 1 mM ethylenediaminetetraacetic acid).

3.3.2 Synthesis of ssDNA-Amphiphiles

ssDNA sequences were purchased from Integrated DNA Technologies (Coralville, IA) with a 3'-amino modifier and an optional 5' HEX (538/555 nm ex/em) or hexynyl (alkyne) group. The G-rich sequence (5'-CTCTTGGGGG-AmMo-3') and C-rich sequence (5'-CCCATTACCCTAGACCCTTATCCC-AmMo-3') were used in this study. ssDNA was precipitated in water using 100 mM cetyl trimethylammonium bromide (CTAB) and centrifuged for 15 minutes at 16,100 g, followed by removal of the liquid and drying of the precipitate under an airstream to remove any excess water. The dried precipitated ssDNA was then resuspended in 90%/10% (v/v) mixture of dimethylformamide (DMF) and DMSO at 500 µM. The C_{16} dialkyl tail with the C_{12} hydrocarbon spacer was synthesized as described elsewhere,[22] added in 10 times molar excess, and reacted for 16 h at 65 °C. The solution was concentrated by drying in a vacuum oven until approximately 50 µL in volume. The reaction product with the ssDNA-amphiphile and unreacted ssDNA was precipitated by a lithium perchlorate precipitation, where 1 mL of lithium perchlorate in acetone (2.5% w/v) was added and the solution was mixed until homogeneous, followed by the addition of 100 µL of water and placed in a -20 °C freezer for 15 min. The precipitate was centrifuged for 15 min at 16,100 g and rehydrated with 1 mL of water and filtered through a 0.45 µm PES filter (GE Healthcare, Chicago, IL). The filtered ssDNA-amphiphiles were separated from unreacted ssDNA using HPLC with HPLC buffer A and HPLC buffer B over 30 min. ssDNA-amphiphiles were then dried under an air stream to

approximately 150 µL, precipitated with 1 mL of lithium perchlorate in acetone to remove HPLC buffer components, and rehydrated at 500 µM in water for storage at -20 °C.

3.3.3 Alkyne DOTA-Thiol Reaction

ssDNA-amphiphiles with a 5'-alkyne modification were mixed with ten molar equivalents of 1,4,7,10-tetraazacyclododecane-1,4,7-tris(acetic acid)-10-(2-thioethyl)acetamide (DOTA-thiol) and one tenth molar equivalent of 2-hydroxy-2-methylpropriophenone photoinitiator in water. The solution was degassed under vacuum for 15 min and stirred under UV light for 2 h. The solution was dialyzed overnight using a Tube-O-DIALYZER Medi 1K MWCO dialysis membrane (G-Biosciences, St. Louis, MO). DOTA-labeled ssDNA-amphiphiles were then concentrated to 500 µM by drying under an air stream.

3.3.4 IRDye 800CW Click Reaction

ssDNA-amphiphiles with a 5'-alkyne modification were mixed in 50% water and 50% DMSO to a final concentration of 100 µM. TEAA buffer was added to a concentration of 200 mM, Cu-TBTA buffer was added to a concentration of 1 mM, ascorbic acid was added to a concentration of 2 mM, and IRDye 800CW Azide (778/794 nm ex/em) (Licor, Lincoln, NE) was added in five times molar excess of the ssDNA-amphiphiles. The solution was mixed and left overnight in the dark at room temperature, followed by a lithium perchlorate in acetone precipitation to remove excess buffer components. The dye-labeled ssDNA-amphiphiles were rehydrated at 500 µM in water for storage at -20 °C.

3.3.5 Liquid Chromatography – Mass Spectrometry (LC-MS)

ssDNA-amphiphiles were analyzed using an Agilent 1100 LC MSD Model G1946 Mass Spectrometer at the University of Minnesota Masonic Cancer Center. 4 µL of ssDNA-amphiphiles at 500 µM were injected onto a 300 µm C_3 column with a 20 min gradient between 15 mM ammonium acetate in water and acetonitrile. The eluent of the chromatography column was sent to the mass spectrometer to determine the mass of the ssDNA-amphiphiles.

3.3.6 Nanotube Preparation

ssDNA nanotubes containing different amphiphiles (unlabeled mixed with fluorescently-labeled or DOTA-labeled) were created by combining the desired amphiphiles at the correct ratio in water. One volume equivalent of DMSO was added to the mixtures so the final DMSO concentration was 50% (v/v). The mixtures were then stirred for 4 h, during which water was slowly added to the mixtures until the final DMSO concentration at 4 h was 10% (v/v). Mixtures were dialyzed overnight using a Tube-O-DIALYZER Medi 1K MWCO dialysis membrane to remove excess DMSO and dried under an air stream to 500 µM to prepare for nanoparticle separation.

3.3.7 Nanotube Separation via Size Exclusion Chromatography

Nanotubes were separated from micelles using size exclusion chromatography on an Äkta fast protein liquid chromatography (FPLC) (Amersham Biosciences, Piscataway, NJ). A C10/20 Column (GE Healthcare, Chicago, IL) loaded with Sepharose CL-4B chromatography matrix was used to separate the nanoparticles. 500 µM of ssDNA-

amphiphile mixtures were loaded at 500 µL per run onto the column and separated using water as a buffer. Fractions were collected based on UV absorbance of the eluent, dried under an airstream to 500 µM, and analyzed using cryogenic transmission electron microscopy (cryo-TEM).

3.3.8 Cryogenic Transmission Electron Microscopy

Lacey Formvar/Carbon 200 mesh copper grids were purchased from Ted Pella (Redding, CA) and glow-discharged for 1 min to make the grids more hydrophilic. 4.5 µL of 500 µM ssDNA-amphiphiles in water were deposited onto the grid and vitrified in liquid ethane using a Vitrobot (Vitrobot parameters: 5 sec blot time, 3 sec wait time, 3 sec relax time, 0 offset, 95% humidity, 25 °C). The grids were transferred to and kept under liquid nitrogen until imaged on a Tecnai G2 Spirit TWIN 20-120 kV/LaB6 TEM operated at an accelerating voltage of 120 kV using an Eagle 2k CCD camera at the University of Minnesota Characterization Facility. Size analysis of 31 micelles, and 153 nanotubes, and 50 C-rich nanotubes was performed using ImageJ software.

3.3.9 Cell Culture

GL261 mouse glioblastoma cells (NIH) or C8-D1A healthy mouse astrocytes (ATCC, Manassas, VA) were cultured at 37 °C and 5% CO_2 using Dulbecco's Modified Eagle Medium (DMEM) (Thermo Fisher Scientific, Rockford, IL) supplemented with 10% (v/v) fetal bovine serum (FBS) (Thermo Fisher Scientific, Rockford, IL) and 100 units/mL penicillin, 0.1 mg/mL streptomycin. Cells were passaged when they reached 80%

confluence by treatment with TrypLE Express Cell dissociation agent (Thermo Fisher Scientific, Rockford, IL).

3.3.10 Nanotube Serum Stability via Gel Electrophoresis

Nanotubes containing 20 mol% HEX-labeled ssDNA-amphiphiles were prepared at 250 µM in water on an amphiphile basis. Nanotubes were mixed into three separate conditions using 2.5 µL of nanotubes and 47.5 µL of solution, for 50 µL total volume of mixture and 12.5 µM final ssDNA-amphiphile concentration. The three solutions used were: 5 µL of 10X PBS with 42.5 µL water as a control, 5 µL 10X PBS with 5 µL FBS with 37.5 µL of water (10% v/v FBS) to mimic *in vitro* conditions, and 5 µL 10X PBS with 42.5 µL FBS (85% v/v FBS) to mimic *in vivo* conditions. Nanotube solutions were incubated at 37 °C for 24 h and were run on 2% agarose gels (2% agarose in 1X TAE buffer) at 120 V for 35 min, and imaged using a ChemiDoc MP Imaging System (Bio-Rad, Hercules, CA).

3.3.11 Nanotube Exonuclease/Endonuclease Stability via Gel Electrophoresis

Nanotubes containing 20 mol% HEX-labeled ssDNA-amphiphiles were prepared at 250 µM in water on an amphiphile basis. Nanotubes were mixed with DNase 1 and exonuclease III (Thermo Fisher Scientific, Rockford, IL) using 2.5 µL of nanotubes and 47.5 µL of solution for 50 µL total solution and 12.5 µM final ssDNA-amphiphile concentration. The 47.5 µL solutions of nucleases contained 5 µL of the 10X reaction buffer provided by each kit to create a final concentration with the ssDNA-amphiphiles of 1X reaction buffer Nuclease concentrations were tested between 0 and 5 U/mL final concentration. Nanotube-nuclease solutions were incubated at 37 °C for 24 h and were run on 2% agarose gels (2%

agarose in 1X TAE buffer) at 120 V for 35 min, and imaged using a ChemiDoc MP Imaging System (Bio-Rad, Hercules, CA).

3.3.12 Nanoparticle Internalization via Confocal Microscopy and Organelle Colocalization

ssDNA-amphiphile nanoparticles containing 20 mol% HEX-labeled ssDNA-amphiphiles were prepared at 250 µM in 1X PBS. 200,000 GL261 or C8-D1A cells were deposited onto glass coverslips within wells of a 24-well plate and allowed to adhere and proliferate for 24 h. The next day, media was replaced with 500 µL of fresh media, and nanoparticles were added to a final concentration of 12.5 µM. After 24 h, the media containing nanoparticles was removed and the cells were washed once with 1X PBS. The cells were then stained simultaneously for their nuclei and membranes using Hoechst 33342 (Thermo Fisher Scientific, Rockford, IL) at 0.92 µg/mL and Wheat Germ Agglutinin AlexaFluor647 (Thermo Fisher Scientific, Rockford, IL) at 5.0 µg/mL respectively for 7 min at 37 °C. The cells were then washed once with 1X PBS and fixed using 4% paraformaldehyde in 1X PBS for 10 min at room temperature, and then washed twice with 1X PBS to remove any remaining paraformaldehyde. Cells were mounted onto glass slides using Prolong Diamond Antifade Mountant (Thermo Fisher Scientific, Rockford, IL) and imaged with an Olympus FluoView FV1000 BX2 Upright Confocal Microscope (University Imaging Centers, University of Minnesota). Image analysis was performed using ImageJ software.

Organelle colocalization was performed in the same manner, but the media replenishment after 24 h used 1 mL instead of 500 µL. Early endosomes were stained by adding 10 µL of CellLight Early Endosomes-GFP Bacman 2.0 (Thermo Fisher Scientific, Rockford, IL) for

a final concentration of 10 particles per well. The CellLight solution was added at the same time as the HEX-labeled ssDNA-amphiphiles, which had a final concentration of 12.5 µM. 2 h prior to the completion of the 24 h incubation, Lysotracker Deep Red (Thermo Fisher Scientific, Rockford, IL) was added to the wells at a final concentration of 200 nM. At the end of the 24 h incubation, the media containing nanoparticles was removed and the cells were washed once with 1X PBS. The nuclei were then stained using Hoechst 33342 at 0.92 µg/mL for 10 min at 37 °C, washed once with 1X PBS, fixed with 4% paraformaldehyde in 1X PBS for 10 min at room temperature, washed twice with 1X PBS, and mounted onto glass slides using Prolong Diamond Antifade Mountant. The cells were then imaged with an Olympus FluoView FV1000 BX2 Upright Confocal Microscope, with image analysis performed in ImageJ software.

3.3.13 Inhibition of Endocytosis

GL261 cells were sub-cultured in a black 96-well plate at 10,000 cells/well in 150 µL of media. After 24 h, media was replenished with 150 µL of fresh media and then cells were incubated with 5 µg/mL filipin III, 2 µM rottlerin, 80 µM dynasore (Abcam, Cambridge, UK), or no inhibitor for 30 min. Nanotubes containing 20 mol% HEX-labeled ssDNA-amphiphiles were added to the cells at a final concentration of 12.5 µM for 1 h. Cells were then washed twice with 1X PBS to remove any non-internalized nanotubes and the fluorescence of internalized nanotubes was measured at 535/555 nm (ex/em) using the area-scanning function of a Synergy H1 microplate reader (BioTek, Winooski, VT). Autofluorescence of untreated cells was subtracted from all fluorescence measurements. Comparisons between groups at a given time point were performed using an ANOVA

analysis with a post-hoc Tukey's HSD test, while pair-wise t-tests were used for comparisons between the same inhibitor across time points.

3.3.14 Direct Injections of Nanotubes to Orthotopic Glioblastoma Mouse Model

Male C57BL/6J mice were purchased from Jackson Laboratory. Four mice were placed into deep anesthesia using an intraperitoneal injection of ketamine (100 mg/kg) and xylazine (10 mg/kg). Buprenorphine (0.03 mg/mL intramuscular) was administered, the mouse head was sterilized, and a 1 cm incision was made along the scalp. 30,000 GL261 cells in 3 µL of sterile saline were implanted into the right-side striatum of the mice. Nanotubes containing 20 mol% IRDye 800CW-labeled ssDNA-amphiphiles were prepared at 1 mM on an amphiphile basis in 1X PBS. Three of the mice were anesthetized with ketamine (100 mg/kg) and xylazine (10 mg/kg) and 2 µL of the nanotube solution was injected into both the left and right striatum, 14 days after tumor cell implantation. At 45 to 105 min after nanotube injections, mice were decapitated, and brains were taken and fixed in 4% paraformaldehyde overnight. Mouse brains were imaged using an *In vivo* Imaging System (IVIS) (University Imaging Centers, University of Minnesota) with 780/820 nm excitation emission settings.

3.3.15 Fluorescent Immunohistochemistry (IHC) Staining and Imaging of Brain Tissue

Following direct imaging, the mouse brains were fixed in 4% paraformaldehyde in 1X PBS, dehydrated in 30% sucrose in 1X PBS, and embedded with cryo-compound OCT (Tissue-Tek, Sacura). The brains were then frozen at -80 °C, 10 µm sections were cut using a Leica cryostat, mounted onto charged Superfrost Plus glass slides (Fisher Scientific), and

stored at -20 °C until staining. The tissue sections were incubated with polyclonal antibodies against glial fibrillary acidic protein (GFAP) (Lifespan Biosciences, Seattle WA) diluted 1:500 in 1X PBS with 1% tween and 5% donkey serum in a humidified chamber at 4 °C overnight. The sections were then incubated with AlexaFluor-488 secondary antibody diluted 1:750 (R&D Systems, Minneapolis MN) for 1 h at room temperature, followed by staining with DAPI for 10 min at room temperature. Mounted slices were imaged in three fluorescent channels using a Nikon Eclipse TE2000-U inverted wide-field fluorescent microscope (University Imaging Centers, University of Minnesota). Image analysis was performed using ImageJ software.

3.3.16 Micro-Positron Emission Tomography (μPET)/Computerized Tomography (CT) Imaging of Orthotopic Glioblastoma Mouse Model

Tumors were prepared in the same manner as for direct brain injections. Fourteen days after GL261 implantation, nanotubes containing 5 mol% DOTA-labeled ssDNA-amphiphiles were mixed with $^{64}CuCl_2$ (Department of Medical Physics, University of Wisconsin, WI). The dried $^{64}CuCl_2$ salt was dissolved in 100 mM sodium acetate in water (pH = 6) at 2 μCi/μL. The nanotubes at 250 μM were diluted to 150 μM in 2X PBS and then mixed with the ^{64}Cu solution (1:1 v/v) giving final concentrations of 75 μM ssDNA-amphiphile and 1 μCi/μL ^{64}Cu in 1X PBS. The mixture was incubated at 37 °C for 1 h to allow for chelation of the radioisotope by the DOTA moieties as well as to pre-heat the solution prior to injection.

Mice were placed under a heat lamp prior to injections to dilate the veins in their tails. The tails were wiped with ethanol swabs to clean them prior to injection, and 200 μL of the

^{64}Cu-labeled nanotube solution was injected into the lateral tail veins of the mice. The final solution injected contained approximately 0.8 pmol of ^{64}Cu and 1.5 nmol of DOTA-labeled ssDNA-amphiphiles, approximately 1,850 times molar excess of DOTA to ^{64}Cu, which has been shown to entirely chelate all available copper.[93] The radioactivity and time of measurement for each individual syringe was measured immediately before and after tail vein injections. 15 min prior to each imaging time point (1, 3, 24 h after injection), mice were anesthetized using 3% isofluorane in oxygen at 0.8 L/min flow. μPET and CT scans were taken on a Siemens Inveon μPET/CT scanner (Center for Magnetic Resonance Research, University of Minnesota). After the 1 h imaging time point, mice were placed under a heat lamp until they regained consciousness. After either the 3 h or the 24 h time point, mice were euthanized for ex vivo organ radioactivity measurements; if mice were not euthanized after the 3 h time point, they were placed under a heat lamp until they regained consciousness.

Images from the μPET/CT scans were saved as DICOM files and cropped to separate each individual mouse. This was done using a custom interactive tool written for MevisLab (http://www.mevislab.de). Care was taken to maintain the coordinate system and the calibrated radiological values contained in the original DICOM files. From these separated images, volumetric 3D renderings of each mouse were created for the whole mouse body. ImageJ was used to create the maximum intensity projections of the head of each mouse and to plot the μPET intensity profiles as a function of distance across the head of the mouse, starting from the left hemisphere.

All animal experiments in this chapter were approved by the IACUC at the University of Minnesota – Twin Cities.

3.3.17 Ex Vivo Biodistribution Analysis

At 3 h or 24 h after injections, mice were euthanized to collect organs for the biodistribution measurements. Organs were excised and weighed to determine their mass. The radioactivity of each organ (kilo counts per minute, kcpm) was recorded using a scintillator and converted to μCi using a calibration curve. The radiation values for each organ were then adjusted for the decay half-life of ^{64}Cu (12.7 h). The total injected dose was calculated by measuring the decay-adjusted radiation in the syringe prior to the injection and subtracting the decay-adjusted radiation in the syringe after injection. Additionally, the decay-adjusted radiation in each mouse's tail at the time of euthanasia was subtracted due to the possibility of missing the vein during injection, thereby limiting the amount of ^{64}Cu systemically delivered. Organ radioactivity was scaled to the normalized injected dose and then scaled by the mass of the organ. Data were plotted as percent injected dose per gram of tissue (%ID/g) and statistically analysis between the two timepoints was performed with a student's t-test.

Images from the μPET/CT scans were saved as DICOM files and cropped to separate each individual mouse. This was done using a custom interactive tool written for MevisLab (http://www.mevislab.de). Care was taken to maintain the coordinate system and the calibrated radiological values contained in the original DICOM files. From these separated images, volumetric 3D renderings of each mouse were created for the whole mouse body.

ImageJ was used to create the maximum intensity projections of the head of each mouse and to plot the μPET intensity profiles as a function of distance across the head of the mouse, starting from the left hemisphere.

3.4 Results

3.4.1 Synthesis and Characterization of Nanoparticles

Synthesis steps for all ssDNA-amphiphiles are shown in Figure 3.1 and 3.2. Successful synthesis was verified using LC-MS (Table 3.1).

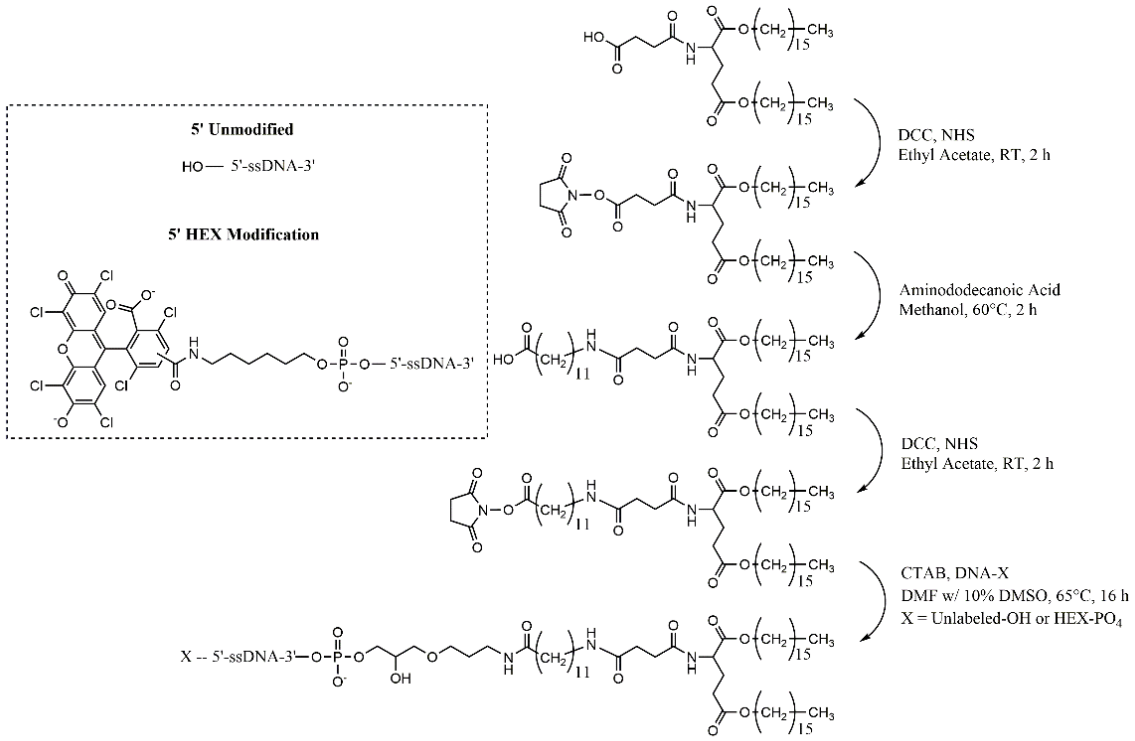

Figure 3.1 Synthesis schemes of ssDNA-amphiphiles with modifications pre-attached to the ssDNA. The inset shows the HEX modification. The full protocol for the first three steps is described elsewhere.[22]

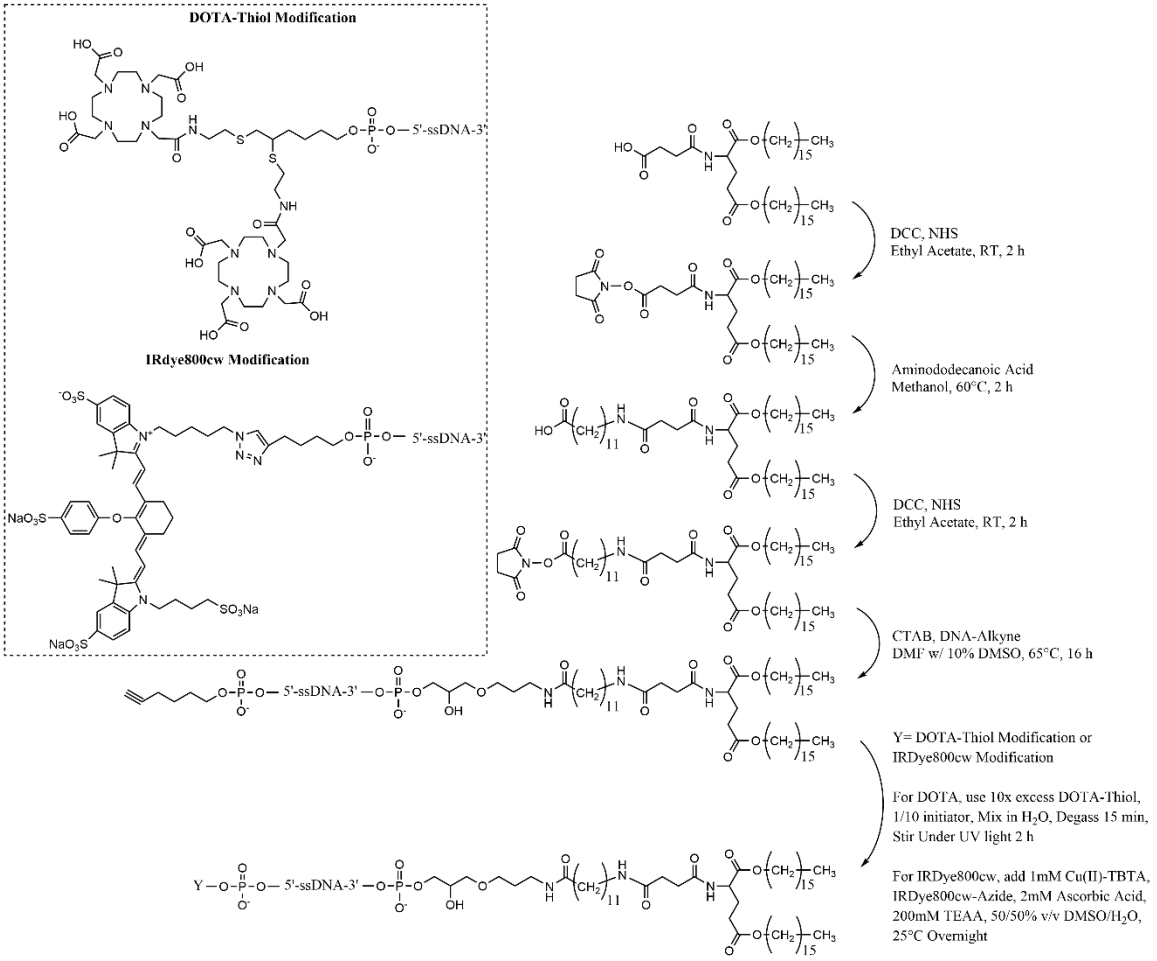

Figure 3.2 Synthesis schemes of ssDNA-amphiphiles with modifications added to the ssDNA via alkyne reactions. The insets show the chemical structures of all modifications used. The full protocol for the first three reaction steps is described elsewhere.[22]

Table 3.1 Expected and measured masses of ssDNA-amphiphiles that did not require addition modification at the 5` terminus.

	Expected Mass (Da)	Measured Mass (Da)
G-rich ssDNA-amphiphile	4161.6	4159.3
G-rich ssDNA-amphiphile HEX	4905.7	4901.2
G-rich ssDNA-amphiphile DOTA	5245.8	5243.7
C-rich ssDNA-amphiphile	8215.2	8211.1
C-rich ssDNA-amphiphile HEX	8959.31	8956.9

Figure 3.3A shows the chemical structures of the different amphiphiles used in this work. Cryo-TEM was used to determine the size of the nanoparticles formed due to self-assembly in aqueous solution. The G-rich ssDNA-amphiphiles formed 10 ± 1 by 8 ± 1 nm weakly ellipsoidal micelles and nanotubes 153 ± 105 nm in length, 25 ± 2 nm in width, and had a wall thickness of 6 ± 1 nm.

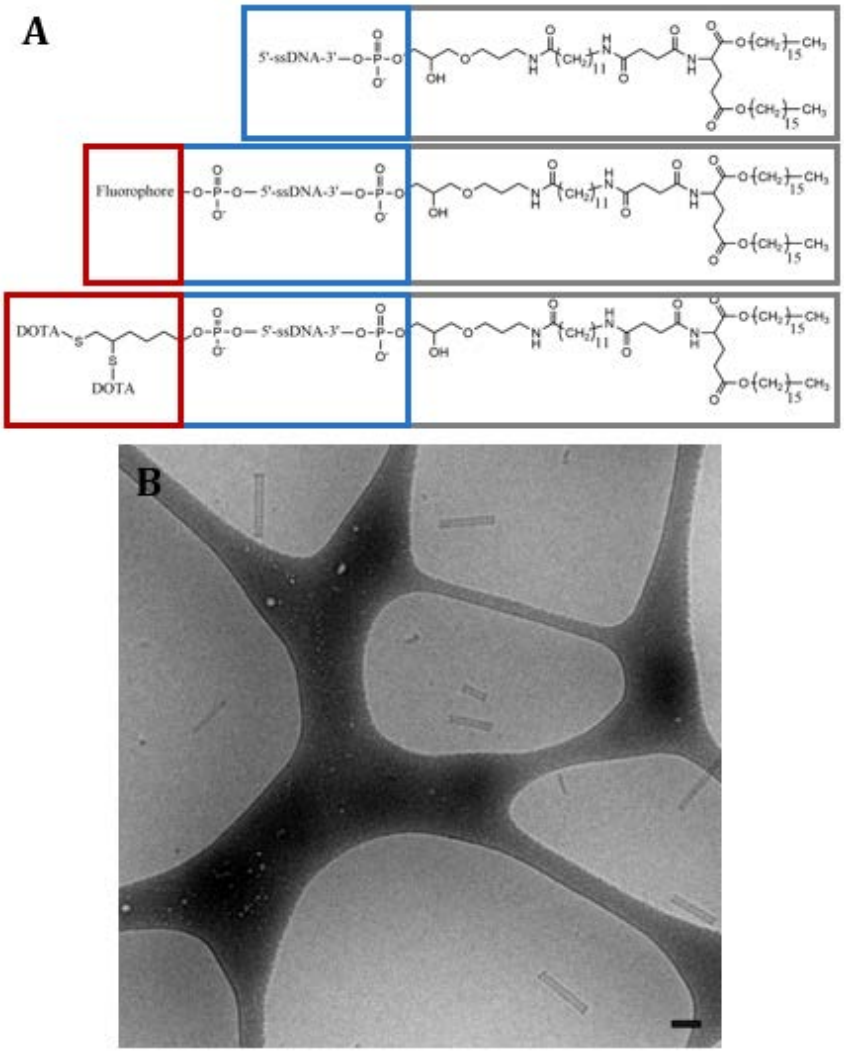

Figure 3.3 (A) Chemical structures of different ssDNA amphiphiles used to create self-assembled structures. (B) Cryo-TEM of ssDNA amphiphiles self-assembled into nanotubes (after FPLC separation), scale bar is 100 nm.

We hypothesized that the nanotubes were formed when the hydrophobic amphiphile tails sequester together creating a bilayer while the ssDNA headgroups extend away from the hydrophobic tails towards the interior and exterior of the nanotubes. This structure is based on previous work using SAXS and cryo-TEM analysis that indicates a bilayer structure.[23, 24] Figure 3.3C shows a cryo-TEM image of the ssDNA-amphiphiles self-assembling into nanotubes. Nanotubes were separated from micelles using size exclusion chromatography. Although full separation of the two nanostructures was never possible due to overlapping elution peaks, it was possible to separate the majority of the nanotubes from the micelles for use as separate samples (Figure 3.4 shows cryo-TEM images of the nanotubes and micelles before and after separation).

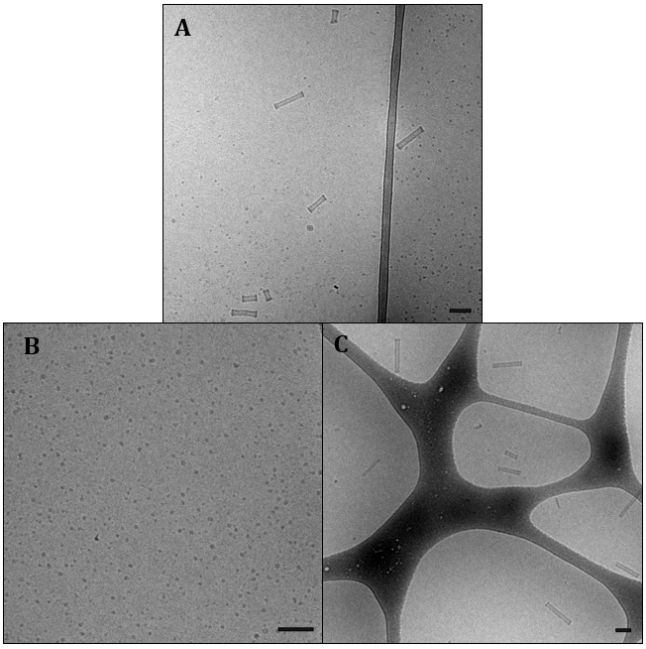

Figure 3.4 Cryo-TEM images of ssDNA amphiphiles (A) prior to FPLC showing presence of micelles and nanotubes, (B) micelle fraction after FPLC, and (C) nanotube fraction after FPLC. Scale bar is 100 nm in all images.

3.4.2 Serum and Nuclease Stability of Nanotubes

The stability of nanotubes in different serum concentrations and nuclease concentrations was investigated using gel electrophoresis to evaluate degradation. The nanotubes were exposed to 1X PBS, 10% FBS (v/v) in 1X PBS to mimic *in vitro* serum conditions, and 85% FBS (v/v) in 1X PBS to mimic *in vivo* serum conditions. As a control, each of the solutions was tested in the absence of the ssDNA-amphiphile nanotubes to ensure that all signal observed originated from the DNA nanoparticles. After 24 h incubations at 37 °C, it was found that there was little change in the electrophoretic mobility of the nanotubes when incubated with 10% FBS (Figure 3.5A). At 85% FBS concentration, the nanotubes showed significantly less electrophoretic mobility (Figure 3.5A). This is likely the result of adsorption of serum proteins onto the surface of the nanotubes, as this adsorption would cause a screening of the negative charges on the DNA backbone as well as an increase in the overall size of the nanoparticles, where both effects lead to less overall electrophoretic mobility.

The G-rich nanotubes were also tested for their stability after exposure to varying concentrations of DNAse I and exonuclease III. After incubation with nuclease concentrations between 0 and 5 U/mL for 24 h at 37 °C, it was found that there was no degradation of the DNA nanotubes when exposed to either DNAse I (Figure 3.5B) or Exonuclease III (Figure 3.5C). The lack of any degradation of the nanotubes is promising for their *in vivo* use.

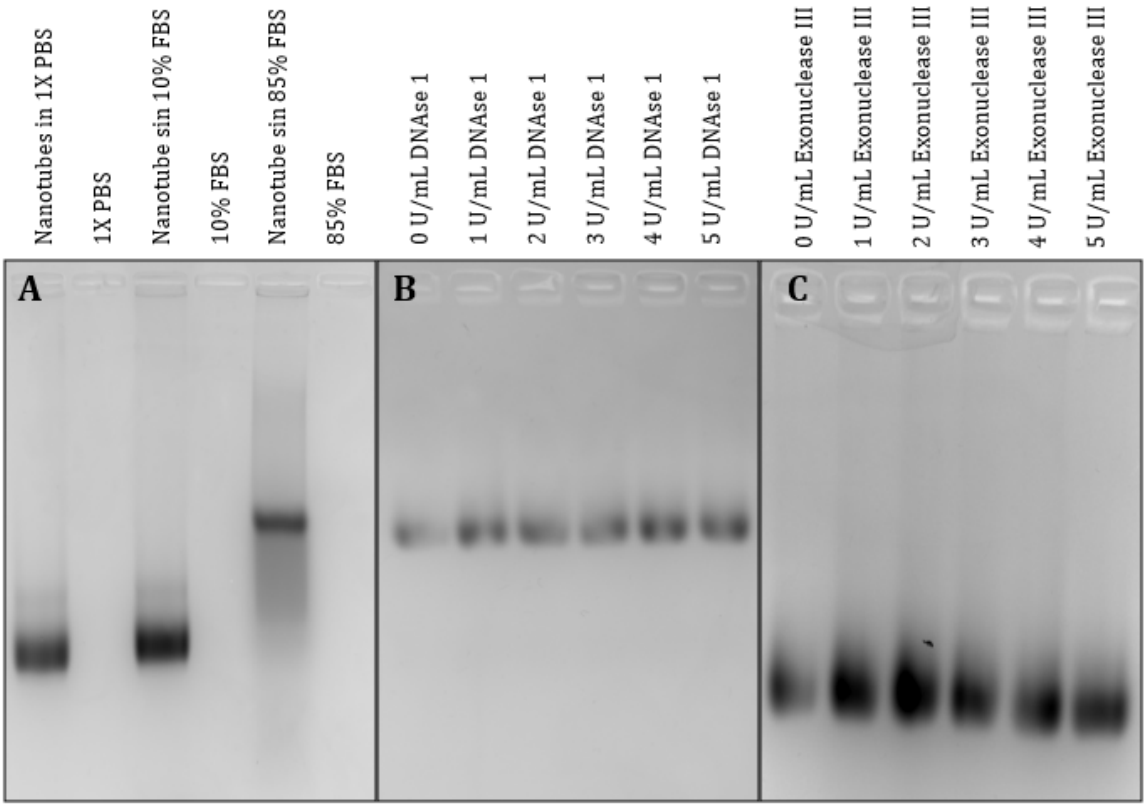

Figure 3.5 (A) Serum stability of nanotubes 20% labeled with HEX. (B, C) Nuclease stability of nanotubes with DNAse1 (B) or ExonucleaseIII (C) with concentrations varying between 0 U/mL and 5 U/mL.

3.4.3 Nanotube and Micelle Cell Internalization

Confocal microscopy was performed on GL261 mouse glioblastoma cells incubated for 24 h at 37 °C with HEX-labeled nanotubes (Figure 3.6A) and micelles (Figure 3.6B) to determine the extent of internalization for each type of nanoparticle. The micelles showed minimal surface binding and internalization after 24 h incubation, while the nanotubes clearly showed strong internalization. As a healthy control cell line, C8-D1A healthy mouse astrocytes were also incubated with the nanotubes (Figure 3.6C) and micelles (Figure 3.6D) and showed no internalization with minimal extracellular surface binding.

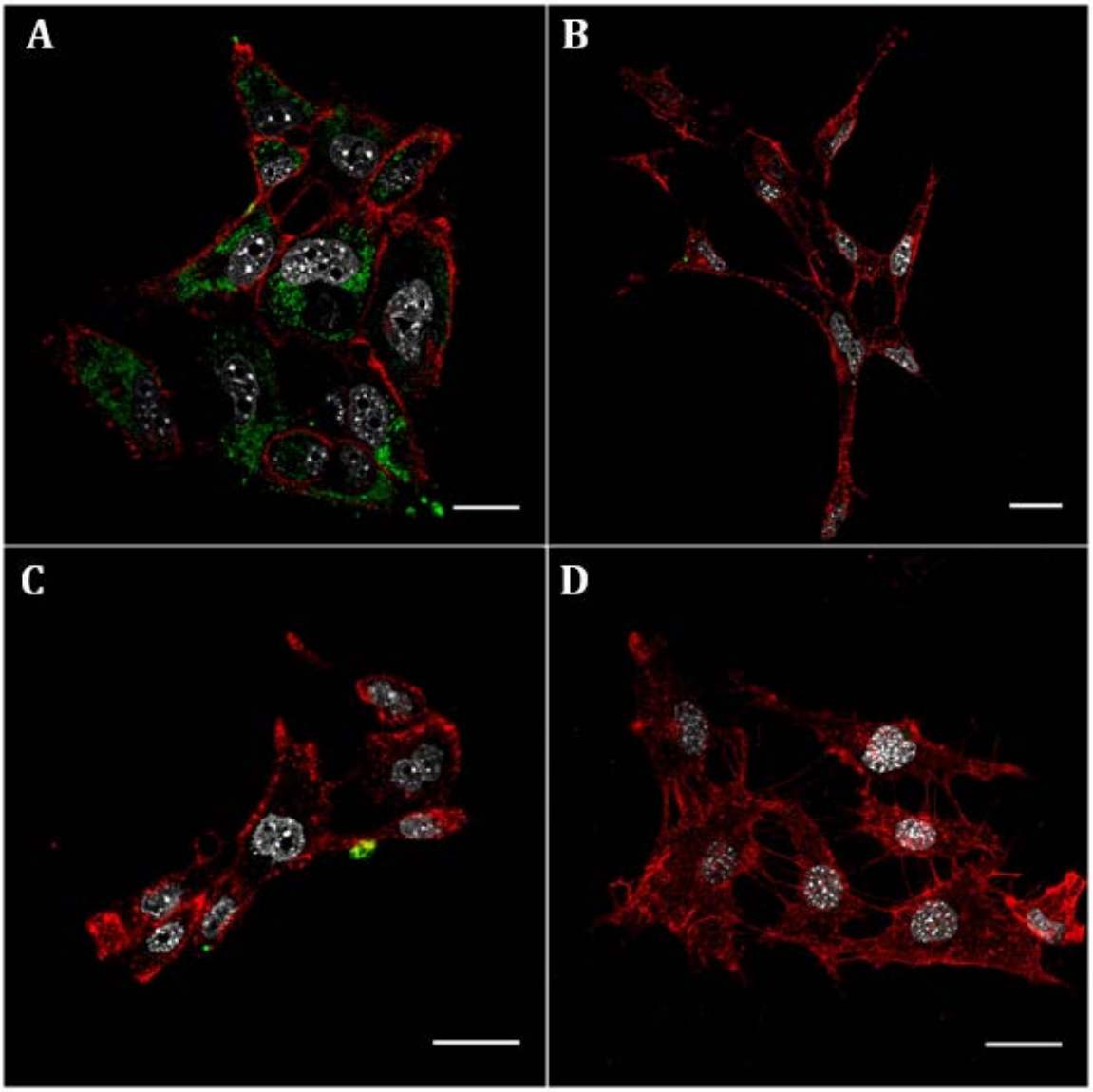

Figure 3.6 Confocal Microscopy of ssDNA-amphiphiles delivered to cells for 24 h at 37 °C. DNA-amphiphiles are shown in green, nuclei in gray, and cell membranes in red. (A) GL261 cells with nanotubes. (B) GL261 cells with micelles. (C) C8-D1A Healthy Mouse Astrocytes with nanotubes. (D) C8-D1A Healthy Mouse Astrocytes with micelles. Scale bars are 20 μm.

To determine if the nanotube internalization observed was due to the particular G-rich sequence of the ssDNA used, GL261 cells were incubated for 24 h at 37 °C with cytosine-rich nanotubes (Figure 3.7). The C-rich sequence produced nanotubes 167 ± 79 nm in length, 29 ± 3 nm in width and 7 ± 1 nm in wall thickness, a similar size and shape to the

G-rich sequence (Figure 3.8). These nanotubes showed strong internalization despite the different ssDNA sequence.

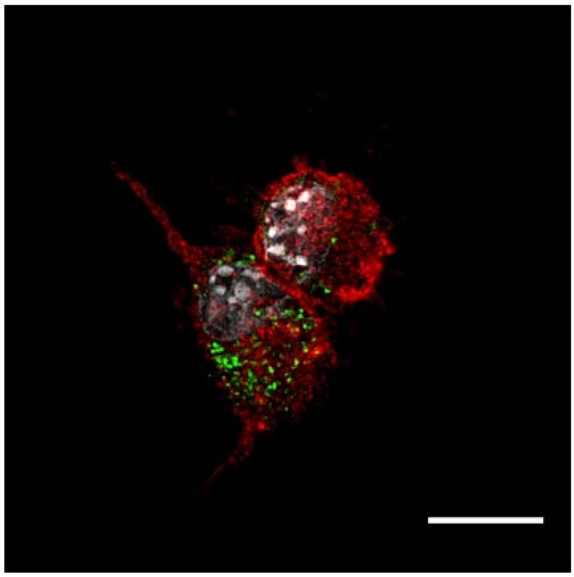

Figure 3.7 Confocal Microscopy of C-rich nanotubes delivered to GL261 cells for 24 h at 37 °C. DNA-amphiphiles are shown in green, nuclei in gray, and cell membranes in red. Scale bar is 20 μm.

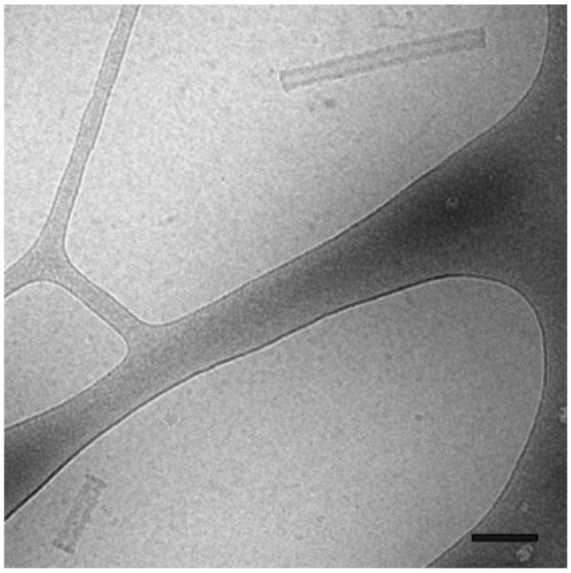

Figure 3.8 Cryo-TEM image of C-rich ssDNA nanotubes after FPLC separation. Scale bar is 100 nm.

3.4.4 Intracellular Trafficking of Nanotubes

Different endocytosis pathways were blocked to investigate which pathways were utilized by the nanotubes (Figure 3.9). Three pathways known to be utilized in the endocytosis of nanoparticles were inhibited: caveolae-mediated endocytosis inhibited by filipin III, clathrin-mediated endocytosis inhibited by dynasore,[175] and micropinocytosis inhibited by rottlerin. The concentrations of each inhibitor used were based on previous literature.[175, 176]

To test the internalization of the nanotubes, GL261 cells were incubated with the three inhibitors and HEX-labeled nanotubes at either 1 h or 6 h. Filipin III incubation showed statistically lower amounts of internalization after a 1 h incubation with relative internalization of 67 ± 4% relative to the untreated control cells. Rottlerin and dynasore incubations did not show any statistical difference from the no-inhibitor control after a 1 h incubation, with relative internalization of 87 ± 10% and 84 ± 5% respectively. Incubation of the nanotubes with endocytosis inhibitors for 6 h showed statistically lowered internalization for all inhibitors when compared to the no-inhibitor control.

Filipin III incubation showed a relative internalization of 74 ± 1%, rottlerin incubation showed a relative internalization of 71 ± 2%, and dynasore incubation showed a relative internalization of 79 ± 2%. The intracellular fate of the nanotubes was further determined by incubating GL261 cells with the nanotubes for 24 h and staining internal organelles. The results, shown in Figure 3.10, show that the nanotubes are colocalized with the early endosomes, the acidic organelles, and are located free in the cytosol, as indicated by the magenta, yellow, and red color observed in the images respectively.

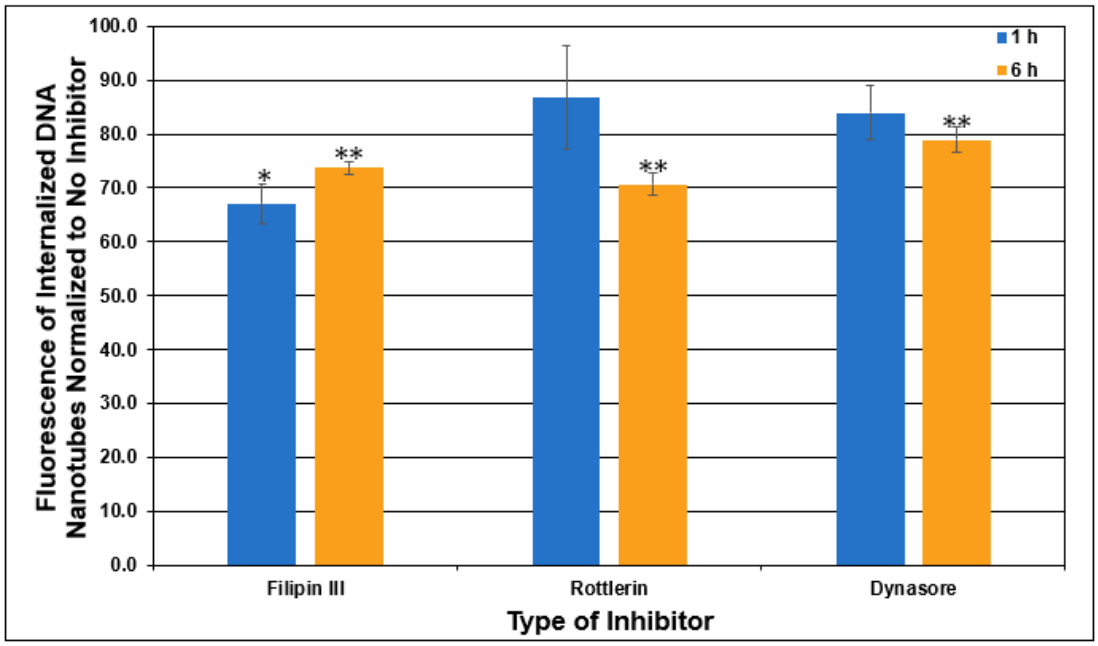

Figure 3.9 Fluorescence of internalized nanotubes after incubation for 2h at 37 °C with different internalization inhibitors. Filipin III inhibits caveolae-mediated endocytosis, Rottlerin inhibits macropinocytosis, Dynasore inhibits clathrin-mediated endocytosis. Statistical analysis compares inhibitor internalization to the internalization observed without inhibitor at a given time-point. Error bars represent Standard Error of the measurements. * $p<0.05$, ** $p<0.005$. No statistical differences were observed between the same inhibitor at different time points.

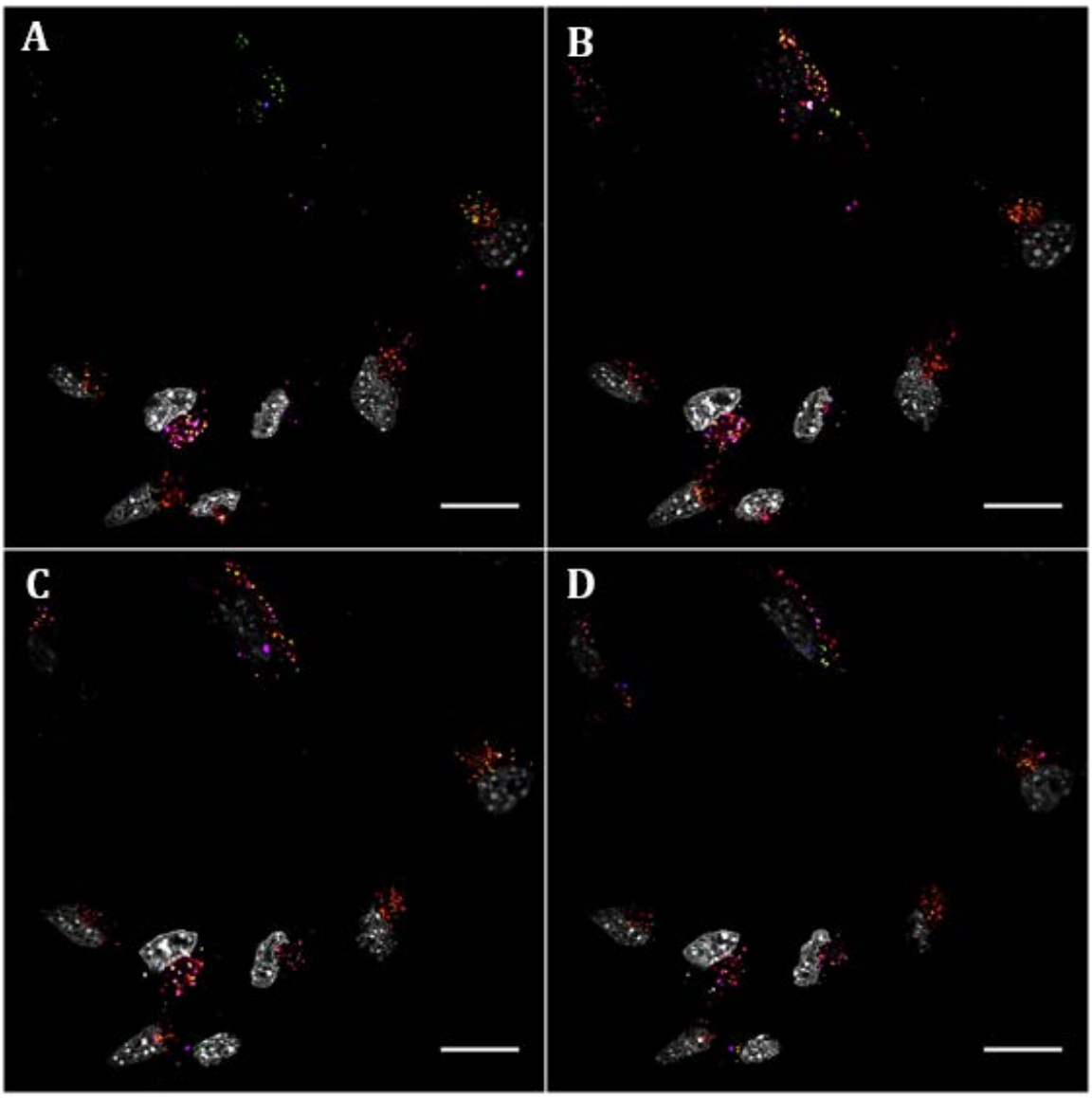

Figure 3.10 GL261 cells were incubated with nanotubes for 24 hours and then stained for nuclei (gray), early endosomes (blue), acidic organelles (green), and nanotubes (red). Frames A, B, C, and D show slices 2, 3, 4, and 5 µm above the glass coverslip respectively. Scale bars are 20 µm.

3.4.5 Direct Injections of Nanotubes to Orthotopic Glioblastoma Mouse Model

After observing strong cell internalization of the nanotubes after incubation with GL261 cells *in vitro*, the retention of nanotubes in a more clinically-applicable system was tested by directly injecting nanotubes into an orthotopic glioblastoma mouse model. GL261

tumors were grown in the right hemisphere of mouse brains and IRDye 800CW-labeled nanotubes were directly injected into both the tumor right hemisphere and healthy left hemisphere of the brain. The mice were euthanized at different time points, their brains were excised, and imaged for nearIR fluorescence (Figure 3.11). One mouse did not receive any nanotube injections as a control. The average ratio of signal between the tumor hemisphere and healthy hemisphere was 2.25, while all three mice that received injections showed signal a full order of magnitude larger than the control mouse (Table 3.2).

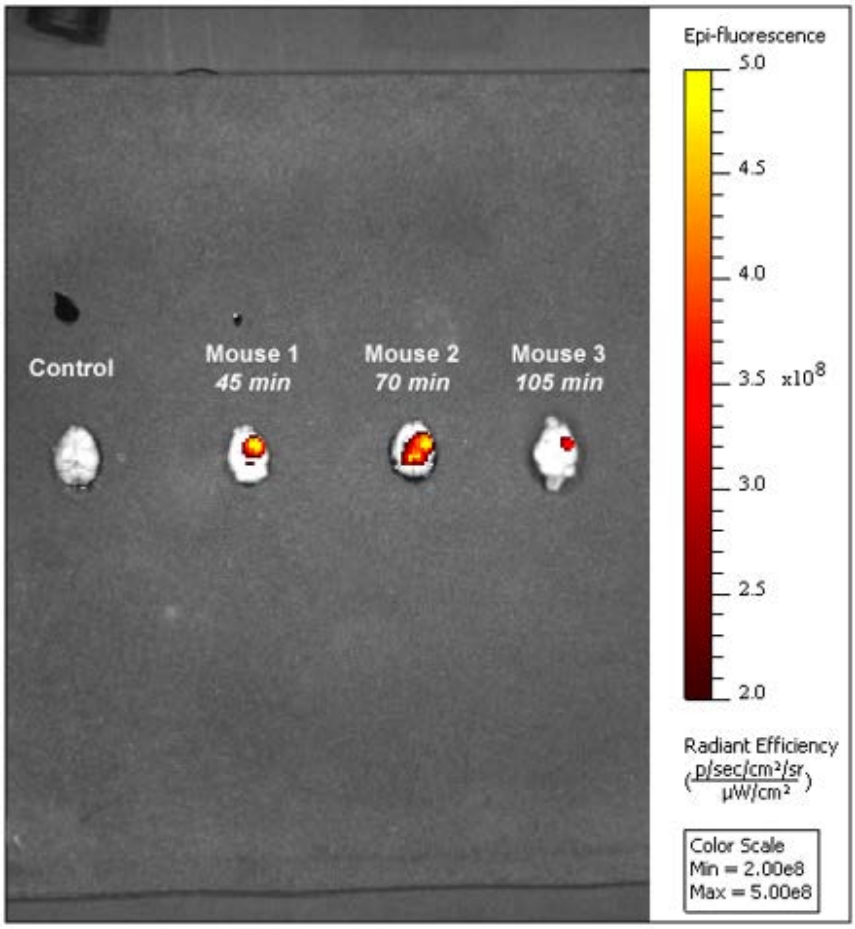

Figure 3.11 Results of direct brain injections of IRDye 800CW-labeled nanotubes into mice bearing orthotopic GL261 tumors. The radiant efficiency of fluorescently-labeled nanotubes for each mouse shown with a heat map.

Table 3.2 Radiant efficiency values of each mouse brain for the left and right hemispheres measured ex vivo. Radiant Efficiency units are [photons/s]/[μW/cm^2].

Mouse	Left Hemisphere Radiant Efficiency	Right Hemisphere Radiant Efficiency	Ratio
Control	0.45×10^8	0.46×10^8	1.02
Mouse 1	5.02×10^8	11.4×10^8	2.27
Mouse 2	4.77×10^8	10.4×10^8	2.18
Mouse 3	2.92×10^8	6.74×10^8	2.31

The excised brains were then sectioned and stained for nuclei and glial fibrillary acidic protein (GFAP) to verify that the observed differences in fluorescence between healthy and tumor hemispheres was a result of differential retention of the nanotubes by the two regions. Figure 3.12A and Figure 3.12B clearly show nanotubes in the tumor hemisphere of the brain, as shown by the bright red signal. The healthy hemisphere, in contrast, shows no retention of nanotubes despite receiving an equivalent volume of fluorescently-labeled nanotubes. The lack of nanotubes in the healthy hemisphere and the absence of fluorescence by the tumor itself was verified by imaging the control mouse brain that had received GL261 injection but no nanotubes, showing no fluorescent signal (Figure 3.12C). Additional imaging of other brain slices shows that this observation is consistent throughout all brain sections (Figure 3.13), indicating that only the tumor hemisphere retained the ssDNA-amphiphile nanotubes and that the signal observed in Figure 3.12 is not specific to the site of the nanotube injection.

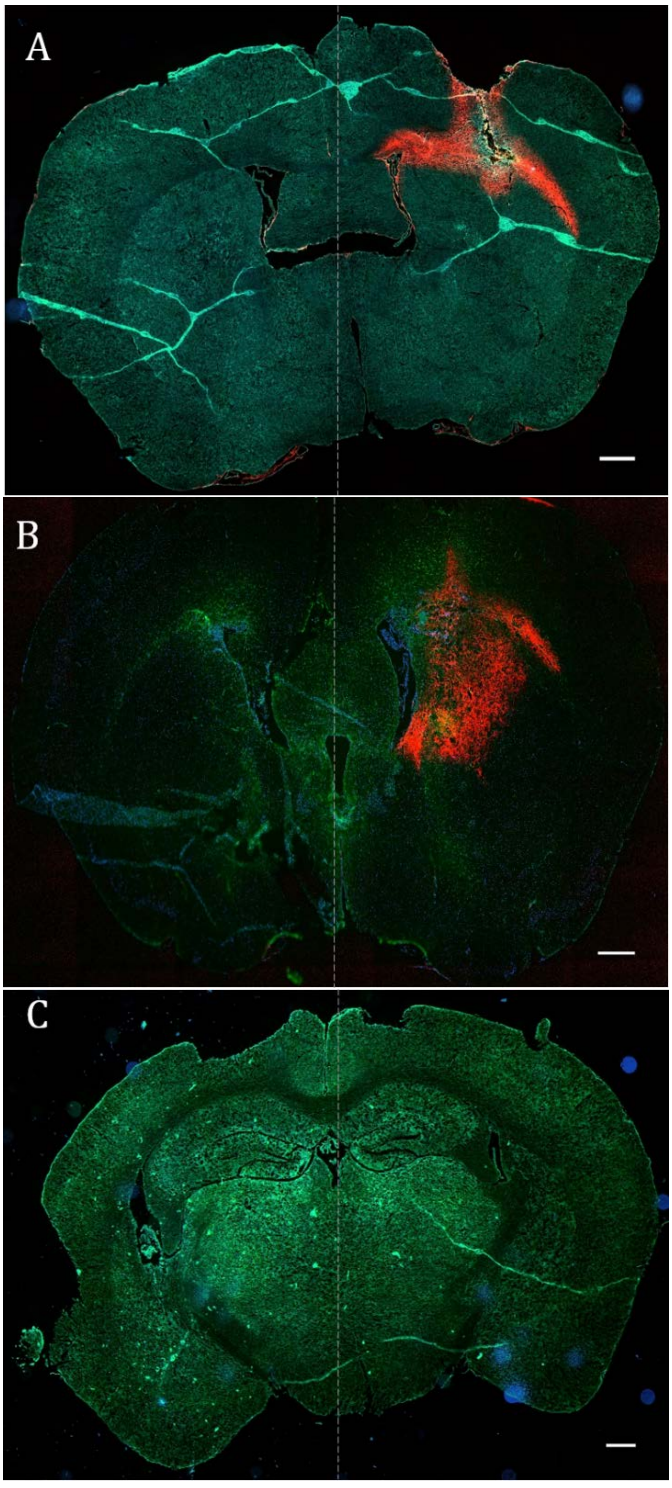

Figure 3.12 Wide-field fluorescent microscopy of excised mouse brains with nuclei stained in blue, glial fibrillary acidic protein stained in green, IRDye800CW nanotubes shown in red. Both hemispheres received an injection of the fluorescently-labeled nanotubes. (A) Mouse 1 Slide 72. (B) Mouse 2 Slide 66. (C) Conrol Mouse Slide 50. Scale bar is 500 µm.

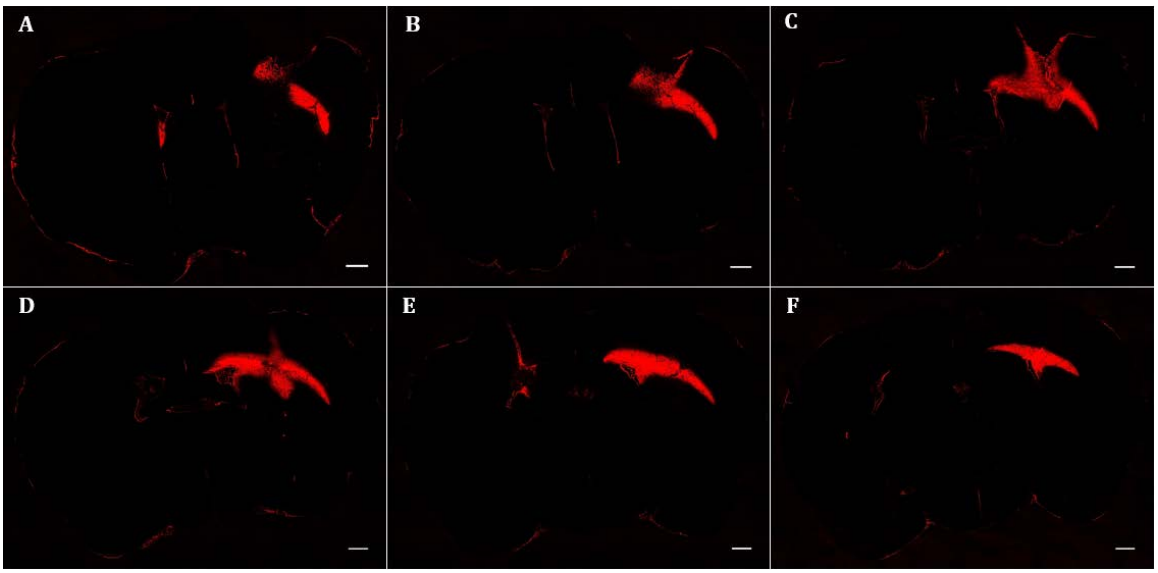

Figure 3.13 Wide-field fluorescent microscopy of different Mouse 1 brain slices showing only the Near-IR fluorescence channel. Nanotubes are bright red. (A) Slice 50 (B) Slice 60 (C) Slice 70 (D) Slice 80 (E) Slice 90 (F) Slice 100. Scale bar is 500 µm.

3.4.6 Biodistribution of Systemically Delivered Nanotubes in Orthotopic Glioblastoma Mouse Model

DOTA-labeled nanotubes were used to chelate ^{64}Cu. DOTA labeling has been shown to result in minimal changes to the size and surface charge of nanoparticles.[177, 178] The DOTA-labeled amphiphiles were present in approximately 1850 times molar excess of ^{64}Cu, ensuring that all available copper was chelated by the nanotubes.[93] Mice bearing orthotopic GL261 tumors on the right brain hemisphere were imaged with µPET/CT at 1, 3, and 24 h after systemic injections of the nanotubes through their lateral tail vein to investigate the localization of the nanotubes in the mice over time. Mice were euthanized at either 3 h or 24 h to evaluate biodistribution. Excised organs were weighed and measured for radioactivity to create a biodistribution at each time point. The activity of each organ was adjusted for the half-life decay of ^{64}Cu and expressed as percentage of injected dose per gram of tissue, shown in Figure 3.14.

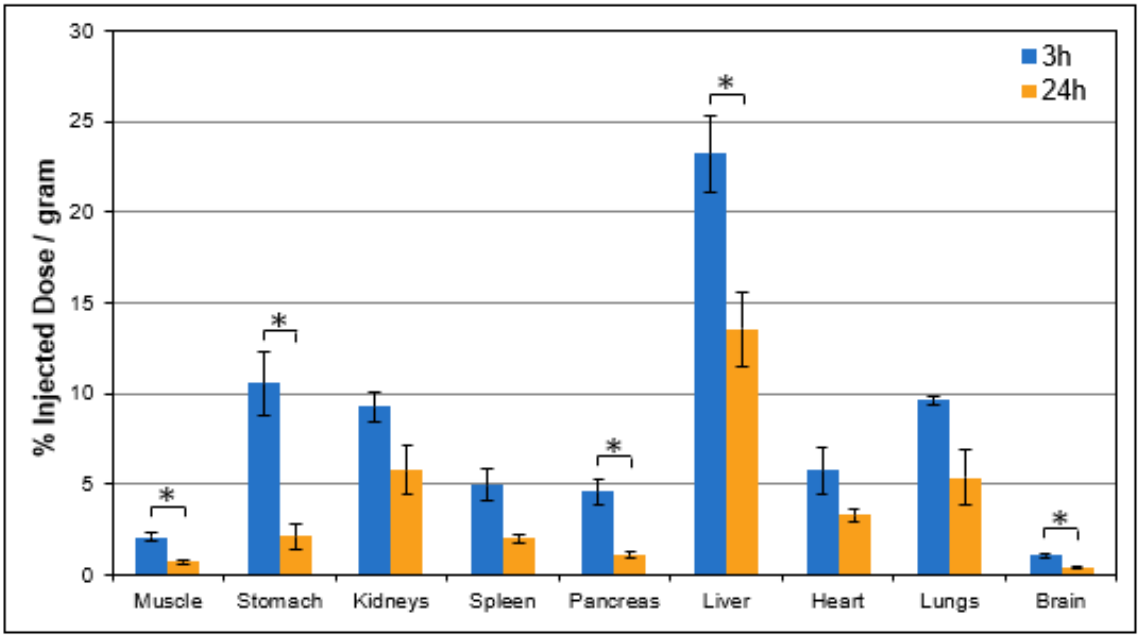

Figure 3.14 Comparison of Ex Vivo Biodistribution of nanotubes systemically delivered to mice bearing GL261 orthotopic tumors at 3 h and 24 h after injection. Error bars show standard error of measurement, * $P<0.05$.

Statistical differences between the decay-adjusted 3 h and 24 h measurements were observed for the muscle, stomach, pancreas, liver, and brain. Although the other measured organs were not statistically different, all organs follow a similar trend, where the measured radioactivity decreased between 3 h and 24 h. P-values for the organ comparisons are available in Table 3.3. Here we report the nanotube brain accumulation at 3 h as 1.1 ± 0.2 %ID/g and at 24 h as 0.4 ± 0.1 %ID/g. The organ with the highest accumulation at both time points was the liver.

Table 3.3 P-values from Student's T-test comparing the 3 h and 24 h accumulation of nanotubes after systemic delivery to mice bearing GL261 orthotopic tumors.

Ex Vivo 3-hour vs 24-hour	P-Value of T-Test
Muscle	**0.012**
Stomach	**0.029**
Kidneys	0.081
Spleen	0.176
Pancreas	**0.033**
Liver	**0.024**
Heart	0.195
Lung	0.067
Whole Brain	**0.039**

Additionally, maximum-intensity projections of the heads of each mouse from the μPET/CT images are shown for the 1, 3, and 24 h time points in Figure 3.15. These images are tail-view projections, viewing the head of the mouse looking from the tail, through the head, and out through the nose of the mouse. Figure 3.15 suggests that for some of the mice, there may be preferential nanotube accumulation occurred in the right hemisphere of the brain, the hemisphere which received the GL261 cells. This can be seen in mouse 1 and mouse 3 in the 1 h and 3 h μPET/CT images. This is further supported by the μPET profile intensity plots in Figure 3.16, which show the radiation in the brain of each mouse relative to the left edge of the mouse cranium. Volumetric 3D reconstructions of the μPET/CT scans for the whole body of each mouse can be seen for each time point in Figure 3.17.

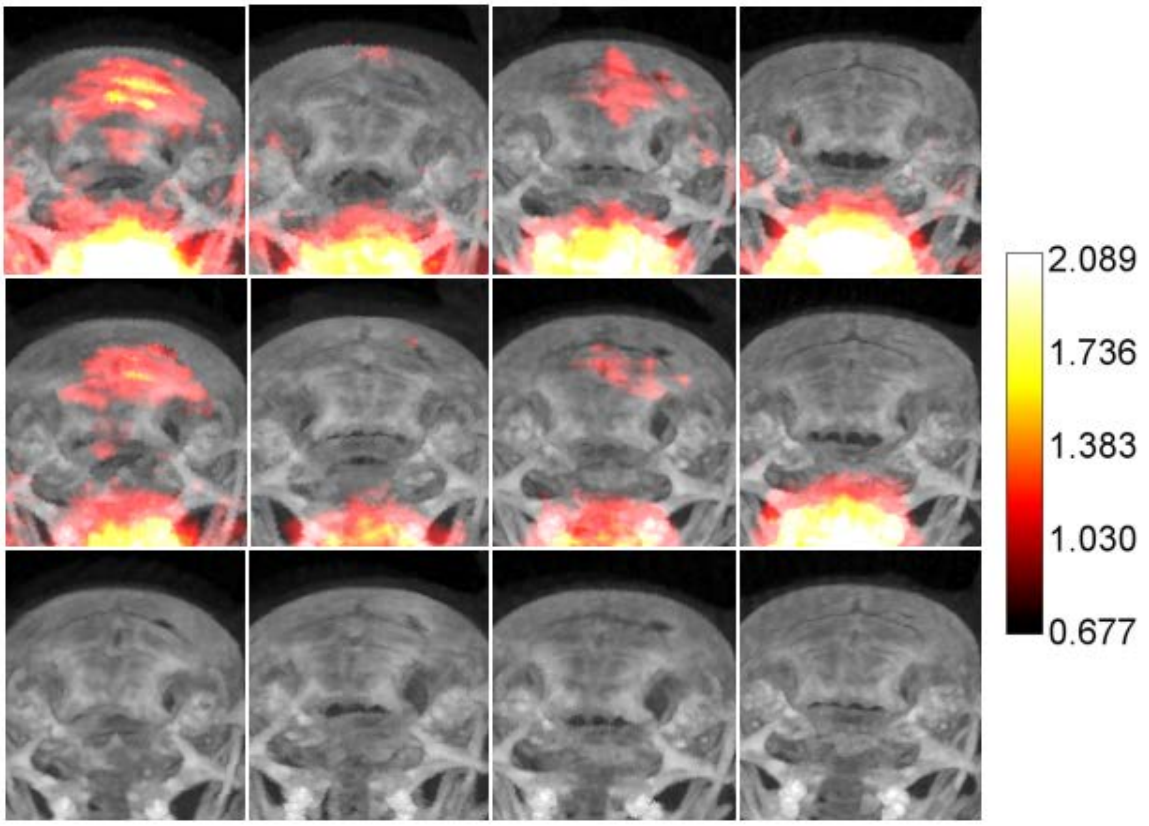

Figure 3.15 Tail-view maximum intensity projection of µPET/CT scans of mice heads at 1 h (top row), 3 h (middle row), and 24 h (bottom row) after injection. µPET intensity scale bar has units of µCi/mL. The intensity of the µPET signal has not been adjusted for the 12.7 h half-life of ^{64}Cu.

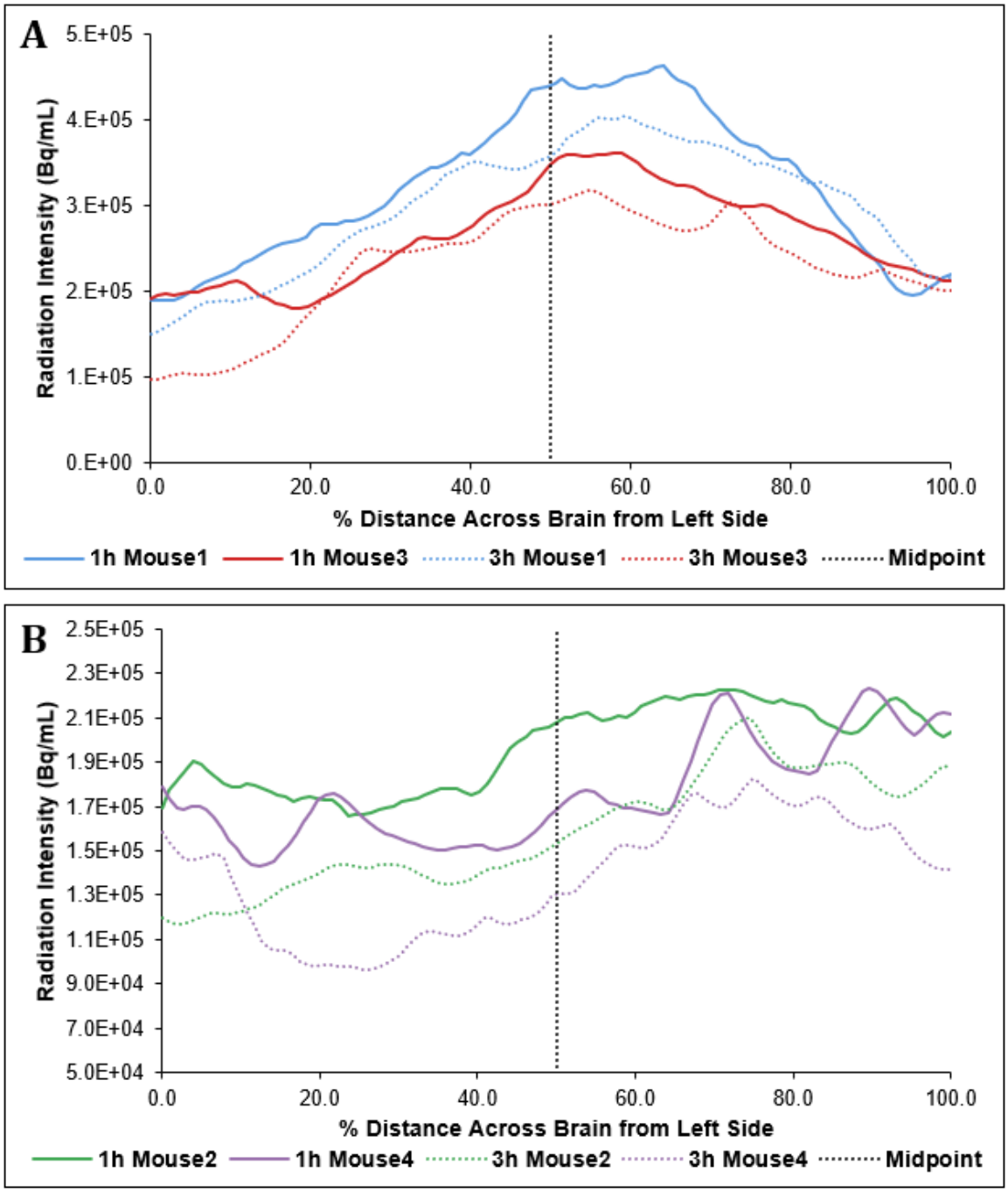

Figure 3.16 µPET signal intensity as a function of distance from the left side of the brain from the head-view images in Figure 3.15. A) Mouse 1 (blue) and Mouse 3 (red) at 1 h (solid line) and 3 h (dashed line). B) Mouse 2 (green) and Mouse 4 (purple) at 1 h (solid line) and 3 h (dashed line). Radiation intensity values have not been adjusted for the half-life decay of ^{64}Cu.

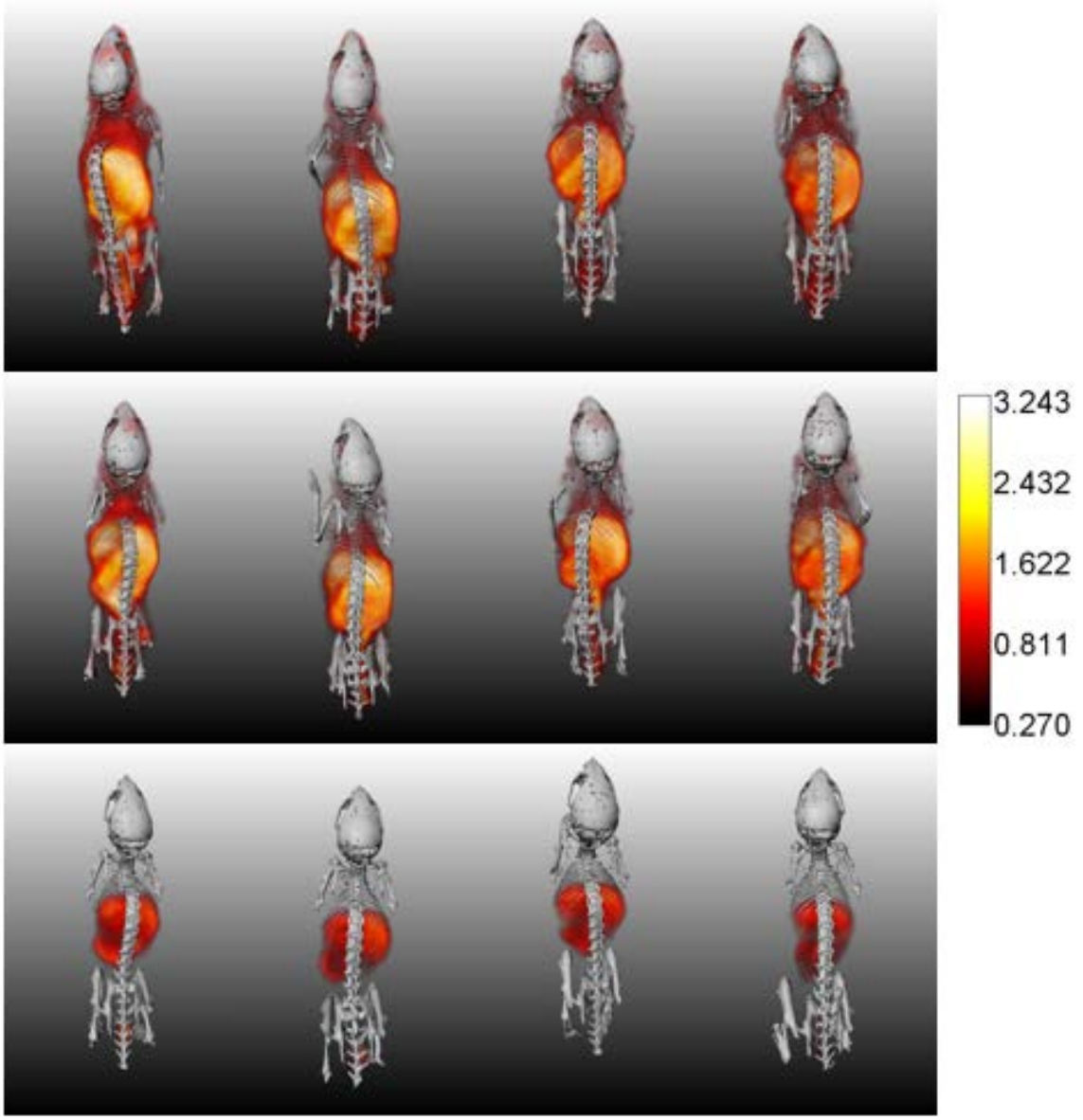

Figure 3.17 Full body volumetric 3D reconstruction of µPET/CT mice imaged at 1 h (top row), 3 h (middle row), and 24 h (bottom row) after systemic injection of ^{64}Cu-radiolabeled nanotubes. The µPET intensity scalebar for all images has units of µCi/mL, and the intensity of the µPET signal has not been adjusted for the 12.7 h half-life of ^{64}Cu. From left to right in each row is Mouse 1 through 4.

3.5 Discussion

In this work, we used ssDNA-amphiphiles that self-assembled into micelles and nanotubes.

Characterization via cryo-TEM showed that the nanotubes were monodisperse in width

and wall thickness, with dimensions of 25 ± 2 nm and 6 ± 1 nm respectively, and had an average length of 153 ± 105 nm, while the micelles that formed from the same ssDNA-amphiphiles were weakly ellipsoidal, with dimensions of 10 ± 1 by 8 ± 1 nm, matching the shape characteristics of previously reported ssDNA-amphiphile micelles.[93, 135] The two distinct populations of nanoparticles could be separated using size exclusion chromatography, allowing for the investigation of shape and size on the uptake properties of nanoparticles formed from the same ssDNA-amphiphile.

A common limitation of ssDNA-based nanoparticles is their stability when delivered *in vivo*. Any potential alteration of the nanotube structure due to interactions with serum proteins could greatly limit the ability of ssDNA-based nanoparticles to act as drug delivery vehicles, and degradation of the amphiphiles themselves would entirely preclude their use. The main degradation pathways as reported in the literature are through desorption of ssDNA by serum proteins, and degradation by nucleases, where direct cleavage of the strand at an internal site by endonucleases, or removal of nucleotides at the terminus by exonucleases is a possibility.[179] The stability of the nanotubes was investigated after incubation with varying amounts of FBS. Using 10% FBS in 1X PBS to mimic *in vitro* culture conditions, the DNA nanotubes showed no change in electrophoretic mobility, suggesting no change to the nanotube structure (Figure 3.5A Lane 3). Using 85% FBS to mimic *in vivo* conditions, the nanotubes showed a decrease in their electrophoretic mobility (Figure 3.5A Lane 5). As electrophoretic mobility is an indicator of the size/charge ratio of a molecule, it is possible that the size of the nanotubes increased, the net charge decreased, or both occurred simultaneously. This suggests that the nanotubes have adsorbed serum

proteins onto their surface in the presence of 85% FBS. No degradation products were observed after incubation with any serum solution as indicated by the lack of distinct bands with higher mobility than the control sample.

ssDNA has been shown to rapidly degrade when exogenously delivered,[180] posing another challenge to its use as a drug delivery vehicle. Therefore, the stability of the nanotubes was investigated after 24 h incubation at 37 °C with DNAse I and Exonuclease III at concentrations ranging between 0-5 U/mL. Figure 3.5B and 3.5C show that no degradation was observed for either nuclease over the entire range of concentrations. The average activity of circulating DNase I in healthy human patients is approximately 0.25 U/mL, while the circulating activity of DNAse I in human cancer patients is 0.1 U/mL or less.[181, 182] Therefore, even at more than ten times physiologically relevant concentrations, the ssDNA-amphiphile nanotubes show no degradation. Little degradation is observed for the exonuclease III, as the 3'-terminus of the amphiphiles is conjugated to the dialkyl tail, preventing exonuclease III from binding to the amphiphile. Additionally, the high local concentration of the ssDNA headgroups in the self-assembled nanostructures likely prevents interaction with DNase I, preventing degradation by internal cleavage. We did not investigate degradation of the amphiphiles due to 5' exonucleases, as it has been shown that 5' exonucleases from serum do not play a significant role in DNA breakdown even when the 5'-terminus is exposed.[179]

Confocal imaging was used to determine the extent of internalization or non-specific membrane association for nanoparticles delivered to GL261 cells. After 24 h incubation,

little internalization was observed for the micelles, which mainly showed low non-specific membrane association (Figure 3.6B), while strong internalization was observed for the nanotubes (Figure 3.6A). It is possible that the differences in uptake observed between micelles and nanotubes made up of the same amphiphiles is the result of an unintended targeting effect. It has been demonstrated that when targeting moieties are present, elongated nanoparticles see stronger internalization than spherical nanoparticles.[71] The results of the confocal imaging match these results of the sequence induced targeting. Therefore, we searched the literature for receptors that could be targeted by the ssDNA-amphiphiles unintentionally.

Scavenger receptors have been identified as a class of membrane-bound receptors that are capable of binding to certain polyanionic macromolecules.[183] Among these, poly-guanine repeat units, such as the sequence found in the G-rich ssDNA, bind to several types of scavenger receptors. However, poly-cytosine repeat units do not bind to these same types of scavenger receptors. Therefore, to test whether the strong internalization observed by the G-rich ssDNA nanotubes was due to unintended targeted via scavenger receptor uptake, a cytosine-rich ssDNA sequence was used to create nanotubes that would be delivered to the GL261 cells. This C-rich amphiphile was found to form nanotubes of similar dimensions to the G-rich amphiphile (Figure 3.8). The GL261 cells showed strong internalization of the C-rich nanotubes after 24 h incubation at 37 °C (Figure 3.7). This shows indirectly that the internalization observed by the G-rich nanotubes may not be a result of unintended targeting of scavenger receptors.

The observed uptake of the nanotubes could also be a result of the cell type. It has been shown that the uptake of elongated nanoparticles was dependent on cell type as well as the size and shape of the nanoparticles.[72] To test if the internalization of nanotubes and lack of internalization of micelles was specific to neural cells in general, and not the GL261 cells, micelles and nanotubes were incubated with C8-D1A healthy mouse astrocytes (Figure 3.6C and Figure 3.6D). These cells showed no internalization and minimal non-specific membrane association. Although this alone does not prove specificity of the nanotubes for GL261 cells, this shows promising results that nanotubes can be used as a drug carrier for delivery to glioblastoma tumors without internalization to healthy astrocytes that could result in off-targeting side effects.

The strong internalization of negatively charged ssDNA nanotubes by the GL261 cells is somewhat surprising, as the negatively charged cell membrane should repel the nanotubes. It has been shown that cationic particles show much stronger internalization as compared to neutral or anionic particles[184] and indeed most internalization and transfection agents for nucleic acids utilize free cations such as calcium phosphate, cationic polymers such as polyethylenimine, or cationic lipids such as lipofectamine. As the precise internalization pathways utilized by the ssDNA nanotubes were unknown, different endocytosis pathways were inhibited and ssDNA nanotube internalization with and without these inhibitors was measured via fluorescence at different time points. Three pathways were inhibited: clathrin-mediated endocytosis was inhibited by Dynasore,[175] caveolae-mediated endocytosis was inhibited by filipin III, and micropinocytosis was inhibited by rottlerin. Figure 3.9 shows that after incubation for 1 h, only filipin III showed a decrease in nanotube

internalization. Therefore, at this short time interval, caveolae-mediated endocytosis is used by the ssDNA nanotubes. The other two inhibitors showed decreased internalization at 1 h, but neither inhibitor showed statistical differences when compared to ssDNA nanotubes incubated without an inhibitor. However, after 6 h incubations, all three inhibitors showed statistically significant decreases in the internalization of nanotubes. This shows that all three pathways are somewhat utilized in the internalization of ssDNA nanotubes. It should be noted that the actual internalization of ssDNA nanotubes at 6 h was higher than internalization at 1 h for all mixtures tested, as more time was allowed for the internalization of ssDNA nanotubes. Confocal microscopy imaging of GL261 cells 24 h after nanotube incubation (Figure 3.10) indicates that the nanotubes are colocalized with the early endosomes, the acidic organelles, and free in the cytosol.

This observed uptake into the early endosomes, acidic organelles, and cytosol is consistent with literature reports. It was shown that DNA nanocubes are internalized by human cervical cancer cells in an endosomal type pathway.[185] DNA tetrahedral nanostructures were shown to be internalized by human cervical cancer cells in a caveolin-dependent pathway, where these nanostructures were transported to the lysosomes when unmodified but could be functionalized with nuclear localization signals that allowed for their escape from the lysosomes.[186] Additionally, similar DNA tetrahedral nanostructures were shown to partition within the cytoplasm of HEK cells at 6 h, 24 h, and 72 h after transfection.[187]

Investigation of the *in vivo* fate of the nanotubes started with the direct injection of the nanotubes into the brains of mice bearing orthotopic GL261 tumors. Injections of

fluorescently-labeled nanotubes were given to both hemispheres of the brain to compare the retention of the nanotubes by healthy tissue and tumor tissue. *Ex vivo* fluorescent imaging of the mouse brains showed that side of the brain with the tumor had approximately 2.25 times higher fluorescence than the healthy tissue (Figure 3.11), indicating higher nanotube retention by the side of the brain with the tumor. The brains were then sectioned, stained, and imaged. Representative slices from two mice are shown in Figure 3.12, showing bright fluorescence of the nanotubes in the side of the brain with the tumor and complete lack of fluorescence in the healthy tissue. As both hemispheres received the same injection of fluorescently-labeled nanotubes, the complete absence of nanotube signal in the healthy tissue was somewhat surprise. To confirm that this was not an artifact of different injection sites, each brain was imaged for nanotube fluorescence throughout the entire length of the brain. Representative slices from one mouse (shown in Figure 3.13) show no fluorescence of the nanotubes in the healthy tissue, indicating that the nanotubes were not strongly retained by the tissue in the healthy hemisphere of the brain, while they were retained by the tissue in the tumor hemisphere of the brain.

The biodistribution of the ^{64}Cu-labeled nanotubes was determined after their systemic injection into mice bearing orthotopic GL261 tumors. Mice were imaged using a μPET/CT scanner at 1, 3, and 24 h after injection, and euthanized after 3 h or 24 h allowing for organ radioactivity to be evaluated. All organs measured showed a decrease in radioactivity between 3 h and 24 h. The organ with the highest delivery was the liver, consistent with the blood clearance profiles of many types of nanoparticles.[51] Brain accumulation at 3 h was 1.1 ± 0.2 %ID/g, while brain accumulation at 24 h was 0.4 ± 0.1 %ID/g (Figure 3.14).

This is significantly higher than literature reports of PEG-co-PLGA (poly lactic-co-glycolic acid) nanoparticles, which show complete lack of accumulation of the nanoparticles 24 h after systemic tail vein injections when either non-targeted or peptide-targeted.[188] Similarly, targeted polystyrene nanorods coated with anti-transferrin monoclonal antibodies also showed only 0.25 %ID/g accumulation 6 h after systemic injection.[71] Doxorubicin bound to non-targeted polymeric nanoparticles was shown to accumulate in the brain at less than 0.8 %ID/g 8 h after injection, and only when those nanoparticles were coated in the non-ionic surfactant polysorbate 80. Without the surfactant coating, the nanoparticles showed no significant accumulation in the brain.[189]

Although internalization of the nanotubes by the GL261 cells was not confirmed after systemic injection of the nanotubes, higher radiation was observed for some mice on the side of the brain that had the tumors (Figure 3.15). These images show, along with the profile intensity plots (Figure 3.16), that mouse 1 and mouse 3 had higher accumulation of the nanotubes in the hemisphere of the brain that had the tumor 1 h and 3 h after injection. Additionally, mouse 2 may have had higher accumulation of the nanotubes in the hemisphere of the brain that had the tumor 1 h and 3 h after injection, but no conclusion can be drawn for mouse 4. Taken together, this suggests that the nanotubes may accumulate more in the tumor hemisphere of the brain. This is consistent with literature reports that glioblastoma tumors can cause a leaky vasculature and disruption of the BBB, allowing for better overall nanoparticle accumulation in the tumor tissue.[149-151]

In conclusion, we have reported the development, characterization, *in vitro* delivery, and *in vivo* delivery of short nanotubes self-assembled from G-rich ssDNA-amphiphiles. These nanotubes are stable after exposure to both serum and nucleases, allowing for their potential use as a drug delivery vehicle. The nanotubes can internalize to GL261 mouse glioblastoma cells, while they do not internalize into healthy mouse astrocytes. Additionally, neither cell type showed internalization of the micelles, suggesting that shape may affect the internalization. This is consistent with literature reports that nanoparticles are most efficiently internalized when they are an intermediate size between 100 nm and 10.[190, 191] The nanotubes were shown to utilize all three major endocytosis pathways when internalizing to GL261 cells. Direct brain injections to mice bearing orthotopic tumors showed that the tumor tissue retained the nanotubes. The biodistribution of the nanotubes after systemic injection showed high brain accumulation of the nanotubes compared to literature reports of similar nanoparticles. Together, this demonstrates that ssDNA-amphiphile nanotubes are a promising nanoparticle for the delivery of therapeutics to glioblastoma tumors.

3.6 Acknowledgements

The C-rich nanotubes were synthesized by Huihui Kuang in the Kokkoli research group. The animal experiments performed for the work in this chapter were done in collaboration with Professor Walter Low and his lab at the University of Minnesota – Twin Cities in the Department of Neurosurgery, specifically Maple Shiao. This work could not have been completed without their expertise and assistance. μPET/CT images were recorded with the

assistance of Kristin Mathson and analyzed with the assistance of Thomas Pengo at the University of Minnesota Informatics Institute.

4 *In Vitro* Delivery of Chemotherapeutics to Glioblastoma Multiforme via Self-Assembled ssDNA-Amphiphile Nanotubes

4.1 Summary

Previous work has shown differential retention of self-assembled single stranded DNA (ssDNA)-amphiphile nanotubes into the tumor hemisphere of mice bearing orthotopic glioblastoma tumors. In this work we hypothesized that these nanotubes could be used to deliver the chemotherapeutic doxorubicin (DOX) *in vitro* to specifically inhibit the growth of GL261 mouse glioblastoma cells. We formed nanotubes, loaded them with DOX, and purified them using size exclusion chromatography. Release profile tests showed that minimal DOX was released from the nanotubes over an extended period of time in solution. *In vitro* tests with glioblastoma cells showed that ssDNA nanotubes alone were nontoxic. When delivered together, DOX-ssDNA nanotubes showed enhanced killing of glioblastoma cells compared to free DOX, demonstrating promise as a chemotherapeutic delivery vehicle.

4.2 Introduction

Glioblastoma multiforme (GBM) is one of the most malignant types of primary brain tumors, with a median survival time of less than one year, and targeted treatment options have not improved survival times. A significant barrier to delivery of therapeutics to the brain is the inability for small molecules to cross the blood-brain barrier. However, glioblastoma tumors have been shown to increase the permeability of the blood-brain barrier (BBB),[149-151] providing a potential pathway for drug delivery vehicle accumulation

in combination with the enhanced permeation and retention effect that aids general tumor targeting.[2] The most common clinical treatment for GBM is to surgically resect as much tumor mass as possible, followed by treatment with radiotherapy and the chemotherapeutic temozolomide (TMZ).[192] TMZ was approved for use by the FDA in 2005 following a Phase III clinical trial. This treatment method was shown to increase the median survival time by two months while showing minimal additional toxicity.[192]

The chemotherapeutic doxorubicin (DOX) has also been used extensively to treat GBM in combination with many different delivery mechanisms. It has been shown that DOX conjugated into polysorbate-80-coated poly(butyl cyanoacrylate) nanoparticles (DOX-NP + PS) does not cause mortality when delivered intravenously three times at concentrations below 2.5 mg/kg to either healthy rats or rats with intracranial glioblastoma tumors.[193] Further studies with the same nanoparticle system showed that the DOX-NP + PS formulation significantly increase the survival time of rats with intracranial glioblastoma tumors compared to all other tested groups when delivered intravenously, with significant differences observed when comparing free DOX and the nanoparticle-loaded DOX formulations.[194] A similar system using intravenously injected DOX loaded into poly(lactic-co-glycolic acid) nanoparticles coated with poloxamer 188 showed effective delivery of DOX across the BBB of rats with orthotopic glioblastomas.[195]

Stealth liposomal DOX formulations in combination with radiotherapy have also been used clinically, showing 7-13 times higher accumulation in primary and metastatic glioblastoma tumors compared to healthy brain tissue.[196] Additionally, four out of ten patients showed

complete response two months following the end of chemo-radiotherapy.[196] Peptide-targeted liposomes in conjunction with high-intensity focused ultrasound have been used to intravenously deliver DOX to orthotopic glioblastomas in mice and compared with free DOX delivery. Survival time of mice treated with peptide-targeted liposomal DOX was increased by 44% compared to untreated control and by an additional 22% when followed by high-intensity focused ultrasound directed at the tumor site.[197] DOX has also been approved by the FDA for treatment of several other types of cancer including bladder, breast, stomach, lung, ovarian, and thyroid cancers. We therefore selected DOX as a chemotherapeutic due to its flexibility in treatment for other types of cancer and its previous use in a wide variety of delivery vehicles.

We have previously used self-assembled ssDNA-amphiphile nanotubes that are capable of internalizing into mouse glioblastoma cells (Chapter 3). These ssDNA nanotubes were shown to internalize into GL261 mouse glioblastoma cells *in vitro*, with minimal internalization to C8-D1A healthy mouse astrocytes, while no internalization was observed for ssDNA micelles for either cell type. When delivered directly to both hemispheres of the brains of mice with orthotopic glioblastoma tumors in the right-side striatum, the ssDNA nanotubes were only strongly retained in the region immediately around the tumor, with no observed retention in the healthy hemisphere. When delivered intravenously to mice bearing orthotopic glioblastoma tumors in the right-side striatum, the ssDNA nanotubes accumulated in the whole brain at 0.4 ± 0.1 % injected dose per gram of tissue 24 h after injection. Additionally, we observed preferential uptake of the nanotubes into the tumor hemisphere of the brain 1 h and 3 h after injection for at least two of four mice

tested. We therefore hypothesized that these nanotubes could be used to deliver the chemotherapeutic DOX to glioblastoma cells *in vitro*. Additionally, based on previous work, we hypothesized that DOX delivered via ssDNA-nanotubes would have higher cytotoxicity as compared to free DOX.

In this work, we loaded ssDNA nanotubes with DOX to assess their efficacy as vehicles for *in vitro* delivery to GL261 mouse glioblastoma cells. The ssDNA nanotubes are self-assembled entirely from ssDNA-amphiphiles. The ssDNA used in this work is a 10 nucleotide (nt) sequence (5` – CTCTTGGGGG – AmMo – 3`), that was synthesized as an amphiphile by conjugating its 3' primary amine it to a dialkyl C_{16} tail with a C_{12} hydrocarbon spacer through a solution-phase reaction (Figure 4.1). This 10nt ssDNA-amphiphile has been shown to self-assemble into hollow nanotubes and spherical micelles.[24] Cryogenic transmission electron microscopy (cryo-TEM) Images showed that the micelle diameters were 10 ± 1 nm in major axis and 8 ± 1 nm in minor axis, and the nanotubes had a wall thickness of approximately 6 ± 1 nm, a diameter of 25 ± 2 nm, and length of 153 ± 105 nm (Chapter 3). Size exclusion chromatography was used to separate the micelles from the nanotubes into distinct samples (Figure 3.4).

4.3 Materials and Methods

4.3.1 Materials

All materials were purchased from Sigma Aldrich and used without further purification or modification unless otherwise stated. Buffers include 1X phosphate buffered saline (PBS) (137 mM sodium chloride, 2.7 mM potassium chloride, 10 mM disodium phosphate, 1.8

mM monopotassium sulfate in water, pH = 7.4). All ssDNA was purchased from IDT (Integrated DNA Technologies, Coralville, IA). The ssDNA sequence used in this work was (5` – CTCTTGGGGG – AmMo – 3`).

4.3.2 Synthesis of DNA-amphiphiles

ssDNA-amphiphiles were synthesized as described elsewhere.[93] Briefly, ssDNA was prepared at 500 µM in water. 100 mM cetyltrimethylammonium bromide was added in 1.2 times molar excess on a nucleotide basis to precipitate all ssDNA. This solution was then dried to remove all water, resuspended at 500 mM in 90%/10% (v/v) mixture of dimethyl formamide (DMF) and dimethyl sulfoxide (DMSO). N-hydroxysuccinimide-activated tails synthesized as described elsewhere[22] were added in 10 times molar excess and reacted for 16 h at 65 °C, reacting with the primary amine on the 3` end of the ssDNA. The organic solvent was then dried and removed via precipitation with lithium perchlorate dissolved in acetone (2.5% w/v). The solution was then rehydrated in water and filtered through a 0.45 µm polyether sulfone filter. The ssDNA-amphiphiles were then separated from the unreacted ssDNA via high performance liquid chromatography, dried under an airstream until reaching 500 µM, and placed in a -20°C freezer for storage. Successful synthesis was previously verified using liquid chromatography – mass spectroscopy (Table 3.1). The entire reaction scheme can be seen in Figure 4.1.

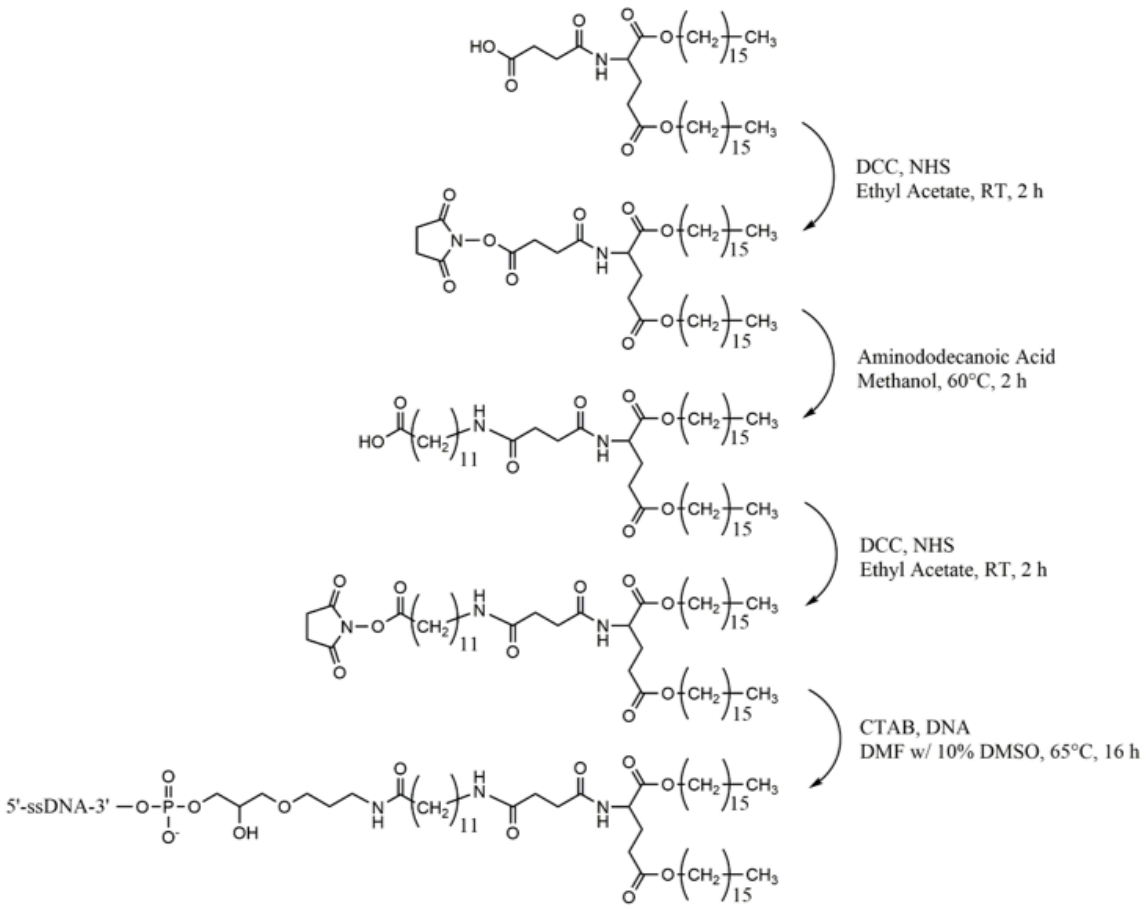

Figure 4.1 Reaction scheme of the ssDNA amphiphiles used in this work. The protocol for the first three reaction steps is described elsewhere.[22]

4.3.3 DOX – ssDNA-Amphiphile Mixing

Doxorubicin-hydrogen chloride (DOX) dissolved in water at 1 mg/mL was combined on an equimolar basis with ssDNA-amphiphiles in water at 500 µM. DMSO was added to the solution until the final DMSO concentration was 50% (v/v). The solution was stirred for 2 h. Over 4 additional h, water was slowly added until the final concentration was 90% water, 10 % DMSO (v/v) at the end of the 4 h. The mixture was dialyzed overnight in a Tube-O-DIALYZER Medi 1k MWCO dialysis membrane (G-Biosciences, St. Louis, MO) to remove the DMSO.

4.3.4 Nanotube Separation

Nanotubes, either empty or mixed with DOX, were separated from micelles using size exclusion chromatography on an Äkta fast protein liquid chromatographer (FPLC) (Amersham Biosciences, Piscataway, NJ). A C10/20 Column (GE Healthcare, Chicago, IL) loaded with Sepharose CL-4B chromatography matrix was used to separate the nanoparticles. 500 µM ssDNA-amphiphile mixtures were loaded 500 µL per run onto the column and separated using distilled water as an mobile phase. Fractions were collected based on UV absorbance of the eluent and then dried under an airstream to 500 µM as measured by UV-Vis absorbance.

4.3.5 UV-Vis Absorbance Concentration Measurements

DNA concentration can be calculated through the absorbance of light at 260 nm. However, DOX also absorbs light at this wavelength. Therefore, the absorbance of mixtures of ssDNA and DOX was measured at both 260 nm and 488 nm, the maximum absorbance wavelengths for DNA and DOX respectively. The extinction coefficient of the ssDNA at 260 nm was provided by IDT as 89300 $cm^{-1}M^{-1}$ and assumed to remain the same after the attachment of the hydrophobic tail. The extinction coefficient of the ssDNA at 488 nm was calculated by measuring the absorbance of a known amount of ssDNA at both 260 nm and 488 nm, providing an extinction coefficient at 488 nm of 135 $cm^{-1}M^{-1}$. Several known concentrations of DOX were prepared by weighing out solid DOX and suspending in known volumes of distilled water. The absorbance for each DOX sample was measured at both 260 nm and 488 nm, allowing for the calculation of the extinction coefficients for DOX as 14715 $cm^{-1}M^{-1}$ and 10200 $cm^{-1}M^{-1}$, respectively. With all four extinction

coefficients and the absorbance measurements at both 260 nm and 488 nm, the concentration of ssDNA-amphiphiles and DOX was calculated by solving the two coupled linear equations: the absorbance observed at 260 nm and 488 nm, each due to the absorbance of ssDNA and DOX. It was assumed that the absorbance of the nanotubes and DOX was additive with no interacting terms.

4.3.6 DOX – ssDNA Nanotube Release Profile

DOX – ssDNA nanotube mixtures were diluted to 50 µg/mL of DOX in 1X PBS. The mixture was then placed in a Tube-O-DIALYZER Micro 1k MWCO dialysis membrane (G-Biosciences, St. Louis, MO) and dialyzed against 2 L of 1X PBS for 2 weeks. At several time points during the dialysis, 2 µL samples were taken out of the dialysis membrane and the absorbance at 260 nm and 488 nm was measured to determine the DOX concentration. After 7 days of dialysis, 20 µL of the sample was taken out of the dialysis membrane for cryo-TEM imaging.

4.3.7 Cryogenic Transmission Electron Microscopy

Lacey Formvar/Carbon 200 mesh copper grids were purchased from Ted Pella (Redding, CA) and glow-discharged for 1 min to make the grids more hydrophilic. Samples of 250 µM DOX – ssDNA nanotubes prior to PBS dialysis were in distilled water, while samples taken 7 days after the start of dialysis were in 1X PBS and were at approximately 50 µM. 4.5 µL of the samples were deposited onto the grid and vitrified in liquid ethane using a Vitrobot (Vitrobot parameters: 4 sec blot time, 3 sec wait time, 3 sec relax time, 0 offset, 95% humidity, 25 °C). The grids were transferred to and kept under liquid nitrogen until

imaged on a Tecnai G2 Spirit TWIN 20-120 kV/LaB6 TEM operated at an accelerating voltage of 120 kV using an Eagle 2k CCD camera at the University of Minnesota Characterization Facility. Size analysis of 50 nanotubes from each formulation was performed using ImageJ software.

4.3.8 Cell Culture

GL261 mouse glioblastoma cells, originally from NIH, were cultured at 37 °C and 5% CO_2 using Dulbecco's Modified Eagle Medium (DMEM) (Thermo Fisher Scientific, Rockford, IL) supplemented with 10% (v/v) fetal bovine serum (FBS) (Thermo Fisher Scientific, Rockford, IL) and 100 units/mL penicillin, 0.1 mg/mL streptomycin (Thermo Fisher Scientific, Rockford, IL). Cells were passaged when they reached 80% confluence by treatment with TrypLE Express Cell dissociation agent (Thermo Fisher Scientific, Rockford, IL).

4.3.9 Cell Viability Assays

The effect of free DOX, empty ssDNA nanotubes, and DOX – ssDNA nanotubes on cell viability was assessed using the Cell Titer Glo 2.0 Assay (Promega Corporation, Madison, WI). 10,000 GL261 were deposited into black 96-well tissue culture treated plates with 100 µL of media and allowed to adhere for 24 h at 37 °C. The next day, media was removed, 95 µL of new media was added and 5 µL of each test sample dissolved in distilled water was added so that each well received the same concentration of media.

To measure nanotube toxicity, empty ssDNA nanotubes with final concentrations between 0 and 8 µM were delivered to the cells. The empty nanotubes were incubated with cells for

24 h at 37 °C to give ample time for the nanotubes to influence cell viability. To test the efficacy of DOX – ssDNA nanotube mixtures compared to free DOX, four samples were delivered to plated cells: distilled water, empty nanotubes in distilled water (5 μM of ssDNA-amphiphile), free DOX in distilled water (5 μg/mL) and DOX – ssDNA nanotube mixtures in distilled water (5 μg/mL DOX, 5 μM ssDNA-amphiphile). The four samples were incubated with cells for 12 h at 37 °C. This was followed by a single wash with 1X PBS, replenishment with 100 μL of media, and additional incubation at 37 °C for 36 h.

Following the incubation with each of the four formulations, the cells were taken out of the 37 °C incubator and allowed to equilibrate to room temperature, while the Cell Titer Glo 2.0 solution was placed in a room temperature water bath. 100 μL of the Cell Titer Glo 2.0 solution was added to each well of cells simultaneously and the entire plate was placed on an orbital shaker for 2 min and then allowed to rest for 10 min. The luminescence signal of each well was measured, and the luminescence of each group was normalized to the luminescence of the untreated cells. All results were compared using an ANOVA with a post-hoc Tukey's HSD test.

4.4 Results and Discussion

4.4.1 DOX – DNA Nanotube Release Profile

The retention of DOX by the nanotubes was investigated by dialyzing a sample of the DOX – ssDNA Nanotube mixture against 1X PBS for 2 weeks. 1X PBS was used as a dialysis medium, both inside and outside the dialysis membrane, because it closely mimics the salt concentration of cell media and serum. As shown in Figure 4.2, DOX was slow to release

from the dialysis membrane over the course of 2 weeks, with 88 ± 3 % retention of DOX over 1 week and 80 ± 5 % retention of DOX over 2 weeks.

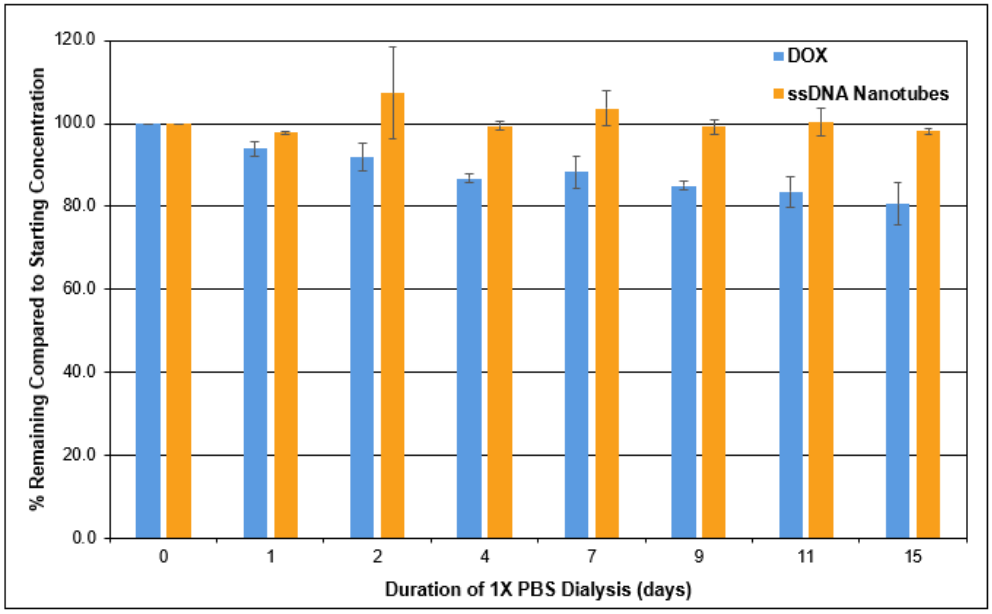

Figure 4.2 Release Profile of DOX – ssDNA nanotubes over time as a percentage of the starting concentration. Reported as average ± standard error of N=2 measurements.

Because DOX acts as a chemotherapeutic by intercalating into the DNA double-helix, thereby preventing DNA replication,[86-89] it was hypothesized that the DOX may bind to the ssDNA-amphiphiles in the nanotube structure, thus making its release in solution slow. Any DOX not associated with the ssDNA-amphiphiles should have quickly diffused out of the membrane, as DOX has a molecular weight of 543.52 Da, is water soluble, and the dialysis membrane used had a 1 kDa molecular weight cut-off. Therefore, this graph suggests that the release of DOX from the nanotubes is minimal in PBS solution on the timescales used for chemotherapeutic delivery. However, this experiment is not capable of capturing the complexity of the cellular environment, as it has been shown that

nanoparticles that do no degrade in solution will degrade and release their payload when exposed to the cellular environment.[198]

4.4.2 Evolution of Nanotube Structure

Seven days after the start of the PBS dialysis, a small sample of the nanotubes was taken for cryogenic transmission electron microscopy (cryo-TEM) imaging. This sample, shown in Figure 4.3, indicates that there is little to no change in the structure of the nanotubes over 1 week. The size of the nanotubes is shown in Table 4.1.

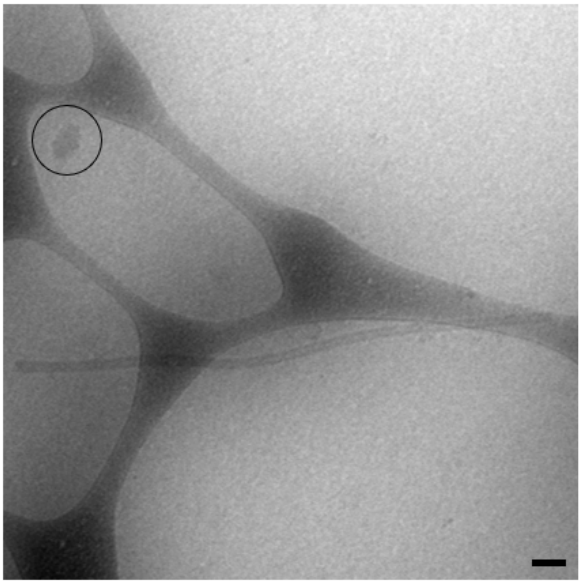

Figure 4.3 TEM image of DOX – ssDNA nanotube mixture after 7 days of dialysis in 1X PBS. Circled in black is surface water ice. Scale bars is 100 nm.

Table 4.1 Size characterization of DOX – ssDNA nanotubes before the start of dialysis and after 7 days of dialysis against 1X PBS. 50 nanotubes from cryo-TEM images of each sample were analyzed using ImageJ software.

Before Dialysis	**Length (nm)**	**Diameter (nm)**	**Wall Thickness (nm)**
Average	864	27	7
Standard Deviation	917	4	1
Median	532	27	7
7 Day Dialysis	**Length (nm)**	**Diameter (nm)**	**Wall Thickness (nm)**
Average	1232	27	7
Standard Deviation	839	3	1
Median	1090	27	7

We observe no change in the diameter or wall thickness of the nanotubes over the first seven days of dialysis, but there does seem to be a slight increase in the length of the nanotubes over this period. Box plots for each measurement are shown in Figure 4.4. The width and wall thickness of these nanotubes is slightly higher than we previously reported for the nanotubes on their own (Chapter 3), but within statistical error.

The length of these nanotubes in the presence of DOX is significantly longer than we previously reported for empty nanotubes. However, because the median length of both the pre-dialysis DOX – ssDNA nanotube sample and the 7-day dialysis DOX – ssDNA nanotube sample is smaller than the average of the sample, as shown in Figure 4.4, the distribution of lengths is not truly gaussian and is instead skewed to shorter lengths. It is unclear why the incorporated DOX affects the length of the nanotubes. Slight differences in preparation protocol, such as the mixing of with dimethyl sulfoxide and the subsequent dialysis, may cause differences in the assembly mechanism. It is also possible that the

incorporation of DOX affects the intermolecular forces of both the hydrophobic tail and the ssDNA headgroup, leading to changes in the assembled structure.

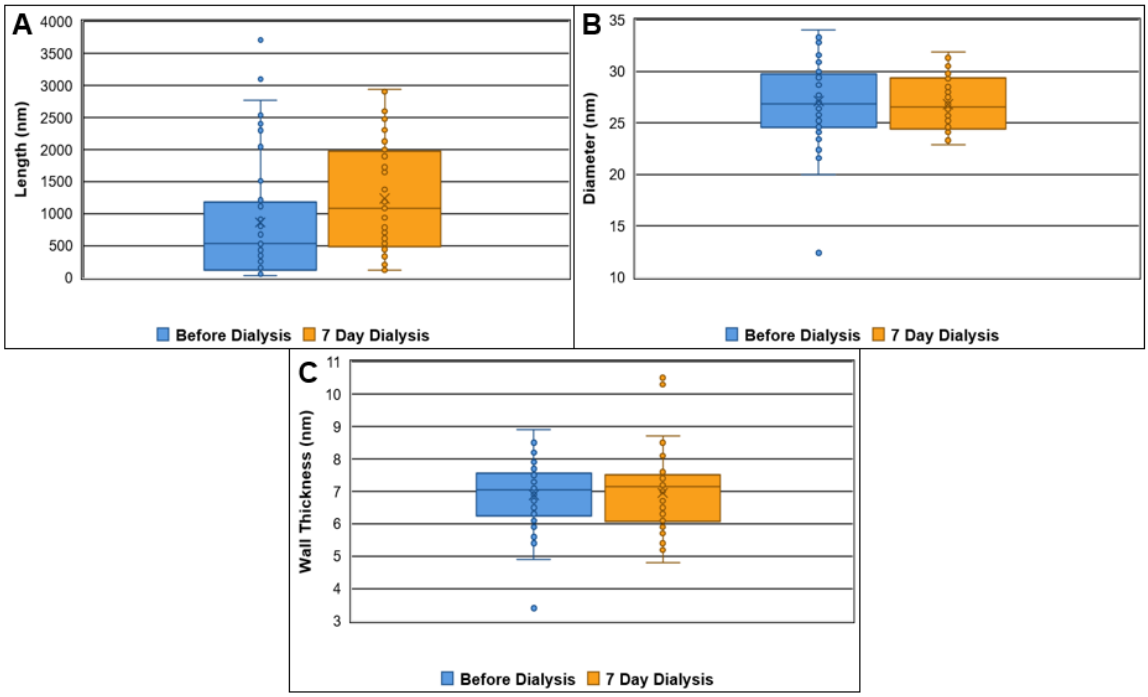

Figure 4.4 Box plots of DOX – ssDNA nanotubes dimensions as measured by Cryo-TEM imaging before dialysis and after 7 days of dialysis in 1X PBS. (A) Distribution of lengths. (B) Distribution of diameters. (C) Distribution of wall thicknesses.

4.4.3 Cytotoxicity of Unloaded Nanotubes

The effect of empty DNA nanotubes on the viability of the GL261 mouse glioblastoma cells after incubation of the nanotubes with the cells for 24 h was also assessed. For all concentrations of ssDNA nanotubes between 0.25 and 8 µM, there was no significant decrease in cell viability compared to the untreated control (Figure 4.5). Additionally, no statistical differences were observed between any given pair of concentrations, where significance was assessed using ANOVA with a post-hoc Tukey's HSD test and P-values

are shown in Table 4.2. This result is not surprising, as the ssDNA nanotubes are composed of an effectively random sequence of DNA.[24]

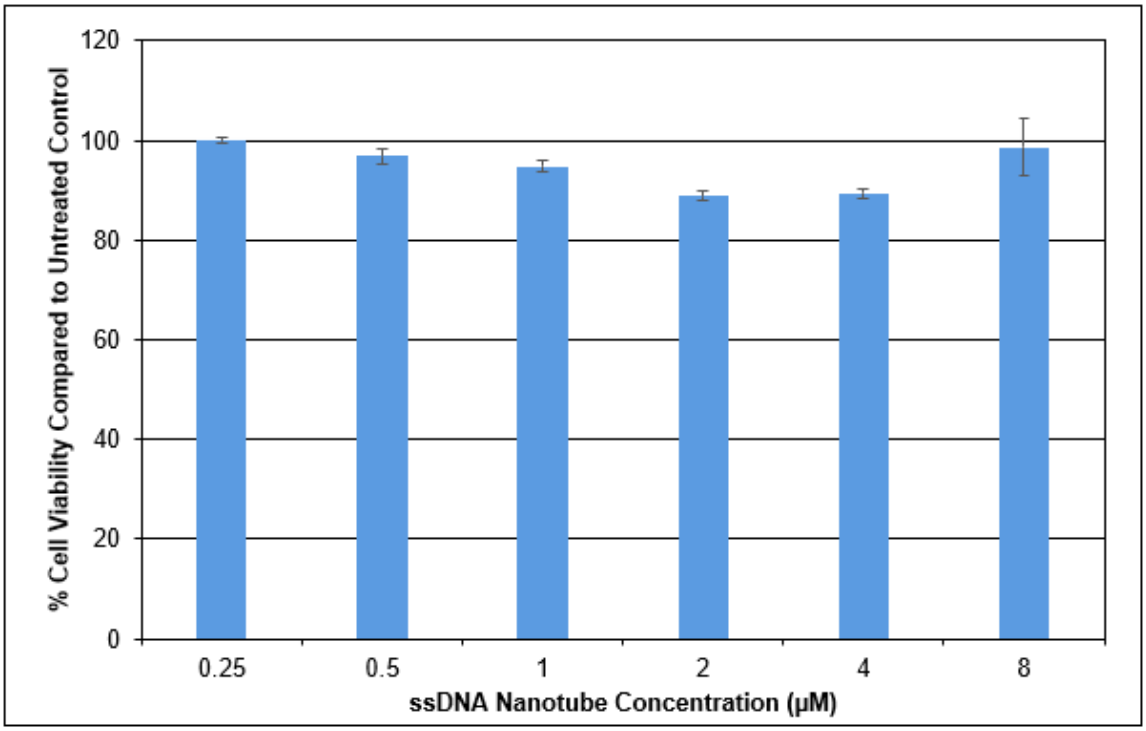

Figure 4.5 Cell Viability of GL261 cells incubated for 24 hours with ssDNA nanotubes compared to untreated control. Error bars show standard error. N=3, measured in triplicate.

Table 4.2 Pairwise P-Value comparisons between ssDNA nanotube concentrations using an ANOVA and post-hoc Tukey's HSD test.

Tukey HSD P-Value Comparisons Between Concentrations						
0.25	0.5	1	2	4	8	
1.000	0.967	0.706	0.064	0.079	0.999	0
	0.967	0.706	0.064	0.079	0.999	0.25
		0.993	0.274	0.326	0.999	0.5
			0.613	0.685	0.908	1
				1.000	0.132	2
					0.162	4

4.4.4 Efficacy of DOX – DNA Nanotube Mixtures

In this work, we have chosen to use 5 µg/mL as the final DOX concentration for cell viability assays. Most cancer cells have IC_{50} values of less than 0.2 µM (0.11 µg/mL) [199, 200]. However, some GBM cell lines have IC_{50} values exceeding 20 µM (10.8 µg/mL) [200]. Therefore, to ensure an appropriate response to DOX delivery would be observed for the GL261 cells, DOX was delivered at 5 µg/mL (9.2 µM). The efficacy of DOX – ssDNA nanotube mixtures was assessed by comparing the cell viability of GL261 glioblastoma cells when incubated with a control solution, empty ssDNA nanotubes, free DOX, and the DOX – ssDNA Nanotubes. The results of this experiment are shown in Figure 4.6. P-values from an ANOVA with post-hoc Tukey's HSD test are shown in Table 4.3 comparing the GL261 cell response to different treatments. The empty ssDNA nanotubes were shown to have no effect on cell viability, consistent with the results from Figure 4.5. However, there is a significant improvement between free DOX and DOX – ssDNA nanotubes for the GL261 cell viability. This suggests that the nanotubes are more effective in the delivery of DOX than free DOX on its own, a promising result for the use of these nanotubes as a delivery vehicle.

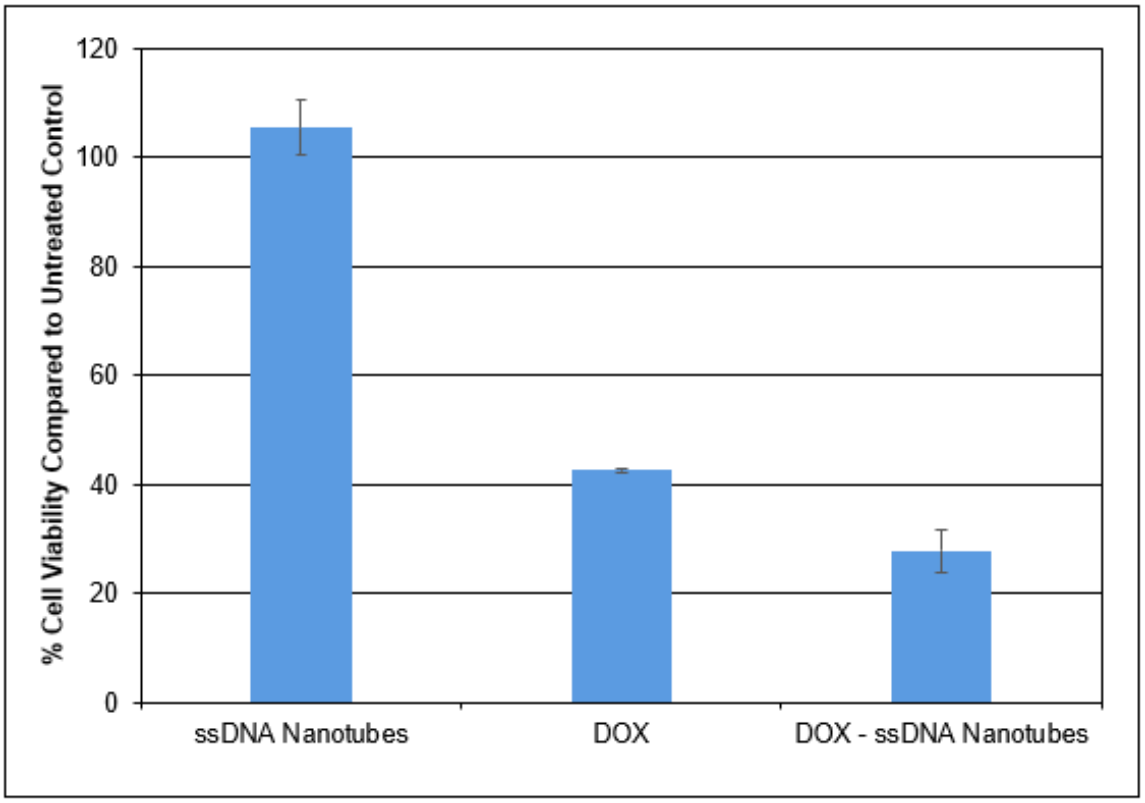

Figure 4.6 Cell Viability of GL261 cells incubated for 12 hours with ssDNA nanotubes (5 µM), Free DOX (5 µg/mL), or DOX – ssDNA nanotubes (5 µM ssDNA nanotubes + 5 µg/mL DOX). Error bars show standard error. N=3, measured in triplicate.

Table 4.3 P-values from ANOVA with post-hoc Tukey's HSD test comparing GL261 cell response to different treatments.

GL261 Tukey HSD P-Values			
ssDNA Nanotubes	DOX	DOX – ssDNA Nanotubes	
0.639	**0.003**	**0.003**	Control
	0.003	**0.003**	ssDNA Nanotubes
		0.049	DOX

4.5 Conclusions

In this report, we have demonstrated that ssDNA nanotubes can associate with DOX to act as a chemotherapeutic delivery vehicle. The presence of DOX increases the length of the nanotubes but does not change their diameter or wall thickness. When incubated in 1X PBS

for 2 weeks, some of the DOX is released by the nanotube structure, with 88 ± 3 % retention of DOX over 1 week and 80 ± 5 % retention of DOX over 2 weeks. We have shown that the incorporation of DOX into the ssDNA nanotube structure significantly improves the therapeutic effect when delivered to glioblastoma cells *in vitro* compared to the delivery of free DOX. We believe this makes the nanotubes a promising delivery vehicle for chemotherapy applications, as a larger percentage of cancer cells can be killed for a given drug dosage.

Further studies need to be performed to investigate several aspects of this delivery mechanism. First the effect of DOX on the length of the ssDNA nanotubes should be investigated further. Additionally, the DOX : DNA nanotube ratio on cell viability must be investigated. It is possible that the ratio used in this work may not be the most effective ratio for achieving cell death. Additionally, the side-effects of off-targeting must be investigated. This should consist of both *in vitro* testing of the DOX – ssDNA nanotube mixture when delivered to healthy astrocyte cells, but the most reliable method for assessing the side-effects of this therapeutic – nanoparticle delivery will be through delivery to a mouse glioblastoma model, whereby tumor size can be tracked alongside animal weight, response times, and histological staining of other tissues, all of which can indicate the presence of healthy tissue damage due to off-targeting.

5 Conclusion

Targeted delivery is an extremely promising contribution to the field of medicine. The design of novel targeting molecules and mechanisms has led to improved drug delivery in many disease types. The use of DNA in targeted delivery is a relatively novel concept. DNA nanotechnology as a field has existed for some time, with creations such as DNA origami and DNA tile assembly.[168, 201] However, the use of ssDNA-amphiphiles for targeted delivery has not been widely reported. This thesis describes how ssDNA-amphiphiles and their self-assembled structures can be used as targeted drug delivery vehicles.

The direct targeting capability of ssDNA-amphiphile micelles was investigated by using a DNA aptamer sequence as the headgroup of the ssDNA-amphiphile. As PEGylation of nanoparticles can be important in prolonging the blood circulation lifetime when delivered intravenously, the effect of PEGylation on binding was investigated. Although the inclusion of a PEG corona on the micelles decreased binding with the target protein, the effect was not entirely lost, as the micelles were still able to bind significantly more to the target cells than to a control cell line. We showed that the targeted aptamer-amphiphile micelles were able to internalize into cancer cells expressing the aptamer target and were localized in the cytosol after 24 hours. At the same time, there was no internalization of the aptamer-amphiphile micelles to cells that did not express the aptamer target. *In vivo* studies showed that targeted and non-targeted ssDNA-amphiphile micelles accumulate in the tumor tissue at equal levels. However, only the targeted micelles that use the aptamer ssDNA sequence are capable of internalizing into the tumor cells. The non-targeted

micelles were only present in the extracellular space of the tumor tissue. Together, this shows that the targeted micelle system requires that the target molecule be present at the cell surface and that the targeting aptamer must be present for internalization.

The passive targeting of cancer cells based on nanoparticle shape and size was investigated using ssDNA-amphiphile nanotubes. It has been shown in the literature that cells have preferential internalization of nanoparticles of different sizes and aspect ratios. We therefore used the ssDNA-amphiphile nanotubes, which self-assemble from ssDNA-amphiphiles due to the sequence of ssDNA used and the types of lipid tails used, to target glioblastoma multiform. These nanotubes were shown to have preferential internalization to glioblastoma multiform cells and no internalization, with only minimal surface binding, to healthy astrocytes. Additionally, they are able to localize in the cytosol 24 h after internalization. When delivered directly to the brains of mice bearing glioblastoma tumors in only one hemisphere, the nanotubes showed retention in the tumor hemisphere, with minimal binding in the healthy tissue. This observation was conserved when delivered systemically. Additionally, the brain accumulation of the nanotubes was approximately 0.40% injected dose per gram of tissue 24 hours after systemic injections, significantly higher than reported literature for other non-targeted nanoparticles.

Following the promising results of nanotubes showing high brain accumulation in orthotopic glioblastoma mouse models, initial *in vitro* chemotherapy studies were performed using the same ssDNA-amphiphile nanotubes. The DOX – ssDNA nanotube mixtures showed slow release of the chemotherapeutic over the course of two weeks,

indicating that DOX bound directly to the nanotube structure. Additionally, cryo-TEM imaging showed no significant changes in the DOX – ssDNA nanotube structure over the same period. The nanotubes were shown to have no impact on cell viability when delivered on their own. However, when delivered mixed with DOX, the nanotubes showed increased cell death for the glioblastoma cells as compared to free DOX. Together, this is a promising result for the future uses of ssDNA nanotubes as a drug delivery vehicle.

A follow-up project for this thesis would include the *in vivo* investigation of chemotherapeutic delivery by the ssDNA-amphiphile nanotubes. The promising *in vivo* biodistribution results and the *in vitro* chemotherapeutic efficacy results indicate that these ssDNA nanotubes may be able to significantly prolong the lives of animals compared to free doxorubicin delivery. Overall, the flexibility of ssDNA sequences and amphiphile structures show huge promise in the improvement of targeted drug delivery vehicles, through both active and passive targeting.

References

1. Nanomedicine Market Analysis By Products, By Application, By Nanomolecule, & Segment Forecasts, 2018 - 2025. www.grandviewresearch.com/industry-analysis/nanomedicine-market May 24, 2018.

2. Maeda, H., *et al. Journal of Controlled Release.* **2000,** 65, (1-2), 271-284.

3. Alley, S. C., *et al. Current Opinion in Chemical Biology.* **2010,** 14, (4), 529-537.

4. Galvin, P., *et al. Cellular and Molecular Life Sciences.* **2012,** 69, (3), 389-404.

5. Lee, J. F., *et al. Current Opinion in Chemical Biology.* **2006,** 10, (3), 282-289.

6. Blume, G., *et al. Biochimica et Biophysica Acta - Biomembranes.* **1990,** 1029, (1), 91-97.

7. Barenholz, Y. *Journal of Controlled Release.* **2012,** 160, (2), 117-134.

8. Ionescu, L. G., *et al.*, Formation of Micelles of Cetyltrimethylammonium Bromide in Water-Dimethyl Sulfoxide Solutions. Mittal, K. L., Ed. Springer New York: Boston, MA, 1979; pp 487-496.

9. Tanford, C. *Science.* **1978,** 200, (4345), 1012 LP-1018.

10. Tanford, C., *The hydrophobic effect: formation of micelles and biological membranes*. 2nd Edition ed.; J. Wiley.: 1980.

11. Israelachvili, J. N., *Intermolecular and Surface Forces*. Third Edit ed.; Academic Press: 2011.

12. Castelletto, V., *et al. Soft Matter.* **2012,** 8, (1), 217-226.

13. Gao, C., *et al. Journal of Physical Chemistry B.* **2017,** 121, (7), 1623-1628.

14. Hartgerink, J. D., *et al. Science.* **2001,** 294, (5547), 1684-1688.

15. Chattopadhyay, A., *et al. FEBS Letters.* **1996,** 391, (1-2), 199-202.

16. Williams, R. J., *et al. Trans. Faraday Soc.* **1955,** 51, (0), 728-737.

17. Dehsorkhi, A., *et al. Soft Matter.* **2013,** 9, 6033-6033.

18. Simard, M., *et al. Journal of the American Chemical Society.* **1991,** 113, (12), 4696-4698.

19. Behanna, H. A., *et al. Journal of the American Chemical Society.* **2005,** 127, (4), 1193-1200.

20. Zhang, J., *et al. Progress in Polymer Science.* **2012,** 37, (8), 1130-1176.

21. Chien, M.-P., *et al. Angewandte Chemie International Edition.* **2010,** 49, (30), 5076-5080.

22. Waybrant, B., *et al. Langmuir : the ACS journal of surfaces and colloids.* **2014,** 30, 7465-7474.

23. Pearce, T. R., *et al. Chem. Commun.* **2014,** 50, (2), 210-212.

24. Pearce, T. R., *et al. Soft Matter.* **2015,** 11, (1), 109-117.

25. Nagarajan, R. *Langmuir : the ACS journal of surfaces and colloids.* **2002,** 18, (1), 31-38.

26. Zhang, J., *et al. Science China Chemistry.* **2014**, 1-12.

27. Hamley, I. W. *Soft Matter.* **2011,** 7, (9), 4122-4122.

28. Lehrman, J. a., *et al. Chemical communications (Cambridge, England).* **2012,** 48, (78), 9711-9713.

29. Paramonov, S. E., *et al. Biomacromolecules.* **2006**, 24-26.

30. Pashuck, E. T., *et al. Journal of the American Chemical Society.* **2010,** 132, (26), 8819-8821.

31. Zhao, X., *et al. Chemical Society Reviews.* **2010,** 39, (9), 3480-3498.

32. Largy, E., *et al.*, Role of Alkali Metal Ions in G-Quadruplex Nucleic Acid Structure and Stability. Sigel, A.; Sigel, H.; Sigel, R. K. O., Eds. Springer International Publishing: Cham, 2016; pp 203-258.

33. Sundquist, W. I., *et al. Nature.* **1989,** 342, (6251), 825-829.

34. Sen, D., *et al. Nature.* **1988,** 334, (6180), 364-366.

35. Bochman, M. L., *et al. Nature Reviews Genetics.* **2012,** 13, (11), 770-780.

36. Gray, D. M., *et al. Chirality.* **2008,** 20, 431-440.

37. Kypr, J., *et al. Nucleic Acids Research.* **2009,** 37, (6), 1713-1725.

38. Hanahan, D., *et al. Cell.* **2000,** 100, (1), 57-70.

39. Hanahan, D., *et al. Cell.* **2011,** 144, (5), 646-674.

40. Torchilin, V. P., Passive and Active Drug Targeting: Drug Delivery to Tumors as an Example. Schäfer-Korting, M., Ed. Springer Berlin Heidelberg: Berlin, Heidelberg, 2010; pp 3-53.

41. Maeda, H. *Journal of Controlled Release.* **2012,** 164, (2), 138-144.

42. Matsumura, Y., *et al. Cancer research.* **1986,** 46, (12 Pt 1), 6387-6392.

43. Sagnella, S., *et al. Australian Biochemist.* **2012,** 43, (3), 5-9.

44. Klibanov, A. L., *et al. FEBS Letters.* **1990,** 268, (1), 235-237.

45. Allen, T. M., *et al. Biochimica et biophysica acta.* **1991,** 1068, 133-141.

46. Van Vlerken, L. E., *et al. Pharmaceutical Research.* **2007,** 24, (8), 1405-1414.

47. He, Q., *et al. Small.* **2011,** 7, (2), 271-280.

48. Gullotti, E., *et al. Molecular pharmaceutics.* **2009,** 6, (4), 1041-1051.

49. Decuzzi, P., *et al. Journal of Controlled Release.* **2010,** 141, (3), 320-327.

50. Moghimi, S. M. *The FASEB Journal.* **2005,** 19, (3), 311-330.

51. Alexis, F., *et al. Molecular Pharmaceutics.* **2008,** 5, (4), 505-515.

52. Caliceti, P., *et al. Advanced drug delivery reviews.* **2003,** 55, (10), 1261-1277.

53. Senger, D. R., *et al. Science.* **1983,** 219, (4587), 983 LP-985.

54. Ferrara, N., *et al. Nature Medicine.* **2003,** 9, (6), 669-676.

55. Neufeld, G., *et al. The FASEB journal : official publication of the Federation of American Societies for Experimental Biology.* **1999,** 13, (1), 9-22.

56. Ellis, L. M., *et al. Nature Reviews Cancer.* **2008,** 8, (8), 579-591.

57. Jain, R. K., *et al. Nature Clinical Practice Oncology.* **2006,** 3, 24-24.

58. Kamba, T., *et al. British Journal of Cancer.* **2007,** 96, (12), 1788-1795.

59. Scott, A. M., *et al. Nature Reviews Cancer.* **2012,** 12, (4), 278-287.

60. Adams, G. P., *et al. Nature Biotechnology.* **2005,** 23, (9), 1147-1157.

61. Bang, Y. J., *et al. The Lancet.* **2010,** 376, (9742), 687-697.

62. Romond, E. H., *et al. N Engl J Med.* **2005,** 353, (16), 1673-1684.

63. Vogel, C. L., *et al. Journal of Clinical Oncology.* **2002,** 20, (3), 719-726.

64. Slamon, D. J., *et al. N Engl J Med.* **2001,** 344, (11), 783-792.

65. Arap, W., *et al. Science.* **1998,** 279, (5349), 377-380.

66. Ellerby, H. M., *et al. Nature Medicine.* **1999,** 5, (9), 1032-1038.

67. Mas-Moruno, C., *et al. Anti-Cancer Agents in Medicinal Chemistry.* **2010,** 10, (10), 753-768.

68. Tuerk, C., *et al. Science.* **1990,** 249, (4968), 505 LP-510.

69. Ellington, A. D., *et al. Nature.* **1990,** 346, 818-818.

70. Waybrant, B., *et al. Chemical communications.* **2012,** 48, (80), 10043-10045.

71. Kolhar, P., *et al. Proceedings of the National Academy of Sciences of the United States of America.* **2013,** 110, (26), 10753-10758.

72. Agarwal, R., *et al. Proceedings of the National Academy of Sciences.* **2013,** 110, (43), 17247-17252.

73. Lind, M. J. **2007**, 19-23.

74. Goodman, L. S., *et al. Journal of the American Medical Association.* **1946,** 132, (3), 126-132.

75. Corrie, P. G. *Medicine.* **2008,** 36, (1), 24-28.

76. Weiss, R. B. *Seminars in Oncology.* **1992,** 19, (6), 670-686.

77. Peng, X. *Molecular Interventions.* **2005,** 5, (3), 163-171.

78. Rowinsky, E. K., *et al. Pharmacology and Therapeutics.* **1991,** 52, (1), 35-84.

79. Coates, A., *et al. European journal of cancer & clinical oncology.* **1983,** 19, (2), 203-208.

80. Wagner, A. D., *et al. Journal of Clinical Oncology.* **2006,** 24, (18), 2903-2909.

81. Stewart, L. A. *Lancet (London, England).* **2002,** 359, (9311), 1011-1018.

82. Vale, C. L. *European Urology.* **2005,** 48, (2), 202-206.

83. Kettenbach, J., *et al. CardioVascular and Interventional Radiology.* **2008,** 31, (3), 468-476.

84. Green, J. A., *et al. Lancet.* **2001,** 358, (9284), 781-786.

85. Organization, W. H. *Essential medicines and health products.* **2017**, (August), 1-39.

86. Frederick, C. A., *et al. Biochemistry.* **1990,** 29, (10), 2538-2549.

87. Tacar, O., *et al. Journal of Pharmacy and Pharmacology.* **2013,** 65, (2), 157-170.

88. Momparler, R. L., *et al.* **1976**, (August), 2891-2895.

89. Pigram, W. J., *et al. Nature New Biology.* **1972,** 235, (53), 17-19.

90. Pommier, Y., *et al. Chemistry and Biology.* **2010,** 17, (5), 421-433.

91. Minotti, G., *et al. Pharmacological Reviews.* **2004,** 56, (2), 185-229.

92. Gewirtz, D. A. *Biochemical Pharmacology.* **1999,** 57, (7), 727-741.

93. Harris, M. A., *et al. Nanomedicine: Nanotechnology, Biology and Medicine.* **2018,** 14, (1), 85-96.

94. Champion, J. A., *et al. Journal of Controlled Release.* **2007,** 121, (1-2), 3-9.

95. Muro, S., *et al. Molecular therapy : the journal of the American Society of Gene Therapy.* **2008,** 16, (8), 1450-1458.

96. Chithrani, B. D., *et al. Nano Letters.* **2006,** 6, (4), 662-668.

97. Jiang, W., *et al. Nat Nanotechnol.* **2008,** 3, (3), 145-150.

98. Albanese, A., *et al. Annual review of biomedical engineering.* **2012,** 14, (1), 1-16.

99. Cho, E. C., *et al. Nano Lett.* **2009,** 9, (3), 1080-1084.

100. Byrne, J. D., *et al. Adv Drug Deliv Rev.* **2008,** 60, (15), 1615-1626.

101. Moghimi, S. M., *et al. Progress in Lipid Research.* **2003,** 42, (6), 463-478.

102. Catuogno, S., *et al. Pharmaceuticals.* **2016,** 9, (4), 69.

103. Waybrant, B., *et al. Chem. Commun.* **2012,** 48, (80), 10043-10045.

104. Bazan, F. J., *et al. Nature.* **1997,** 385, (6617), 640-644.

105. Matloubian, M., *et al. Nature immunology.* **2000,** 1, (4), 298-304.

106. Garton, K. J., *et al. J. Biol. Chem.* **2001,** 276, (41), 37993-38001.

107. Hundhausen, C., *et al. Blood.* **2003,** 102, (4), 1186-1195.

108. Haskell, C. A., *et al. J. Biol. Chem.* **1999,** 274, (15), 10053-10058.

109. Liu, G. Y., *et al. J. Biol. Chem.* **2005,** 280, (20), 19858-19866.

110. Fong, A. M., *et al. Journal of Biological Chemistry.* **2000,** 275, (6), 3781-3786.

111. Mishima, K., *et al. Cancer research.* **2001,** 61, (14), 5349-5354.

112. Cockwell, P., *et al. Journal of Pathology.* **2002,** 196, (1), 85-90.

113. Chakravorty, S. J., *et al. Clinical and Experimental Immunology.* **2002,** 129, (1), 150-159.

114. Wong, B. W. C., *et al. Cardiovasc. Pathol.* **2002,** 11, (6), 332-338.

115. Nebiker, C. A., *et al. Clinical Cancer Research.* **2014,** 20, (12), 3094-3106.

116. Efsen, E., *et al. Journal of Hepatology.* **2002,** 37, (1), 39-47.

117. Herbst, R. S., *et al. Cancer.* **2002,** 94, (5), 1593-1611.

118. Christensen, M. E., *et al. Br. J. Cancer.* **1995,** 72, (6), 1487-1493.

119. Karlstrom, S., *et al. J. Med. Chem.* **2013,** 56, (8), 3177-3190.

120. Wollberg, A. R., *et al. Proc. Natl. Acad. Sci. USA.* **2014,** 111, (14), 5409-5414.

121. Waybrant, B., *et al. Langmuir.* **2014,** 30, (25), 7465-7474.

122. Gu, F., *et al. Proc. Natl. Acad. Sci. USA.* **2008,** 105, (7), 2586-2591.

123. Zagorovskya, K., *et al. Proc. Natl. Acad. Sci. USA.* **2016,** 113, (48), 13600-13605.

124. Wu, Y., *et al. Proc. Natl. Acad. Sci. USA.* **2010,** 107, (1), 5-10.

125. Jensen, A. I., *et al. Biomacromolecules.* **2014,** 15, (5), 1625-1633.

126. Dogdas, B., *et al. Phys Med Biol.* **2007,** 52, (3), 577-587.

127. Xie, T., *et al. Physics in medicine and biology.* **2013,** 58, (1), 169-169.

128. Coxson, H. O., *et al. American Journal of Respiratory and Critical Care Medicine.* **1999,** 159, (3), 851-856.

129. Pearce, T. R., *et al. Adv. Mater.* **2012,** 24, (28), 3803-3822.

130. Kuang, H., *et al. Advanced drug delivery reviews.* **2017,** 110-111, 80-101.

131. Bartlett, D. W., *et al. Proc. Natl. Acad. Sci. USA.* **2007,** 104, (39), 15549-15554.

132. Schluep, T., *et al. Proc. Natl. Acad. Sci. USA.* **2009,** 106, (27), 11394-11399.

133. Harris, J. M., *et al. Nat. Rev. Drug Discov.* **2003,** 2, (3), 214-221.

134. Gabizon, A., *et al. Clin Pharmacokinet.* **2003,** 42, (5), 419-436.

135. Wilner, S. E., *et al. Journal of the American Chemical Society.* **2015,** 137, (6), 2171-2174.

136. Regev, O., *et al. Colloid. Polym. Sci.* **2004,** 282, (4), 407-411.

137. Zetterberg, M. M., *et al. J. Colloid Interface Sci.* **2016,** 484, 86-96.

138. Chinen, A. B., *et al. Angew. Chem. Int. Ed.* **2015,** 54, (2), 527-531.

139. Rush, A. M., *et al. ACS Nano.* **2013,** 7, (2), 1379-1387.

140. Tamkovich, S. N., *et al. Ann. N.Y. Acad. Sci.* **2006,** 1075, 191-196.

141. Willmann, J. K., *et al. Radiology.* **2008,** 249, (1), 212-219.

142. Owens, D. E., *et al. Int. J. Pharm.* **2006,** 307, (1), 93-102.

143. Choi, C. H. J., *et al. Proceedings of the National Academy of Sciences.* **2011,** 108, (16), 6656-6661.

144. Dearling, J. L. J., *et al. Nucl. Med. Biol.* **2011,** 38, (1), 29-38.

145. Guo, J., *et al. ACS Applied Materials and Interfaces.* **2014,** 6, (24), 21769-21779.

146. Park, J. W., *et al. Clinical Cancer Research.* **2002,** 8, (4), 1172-1181.

147. Kirpotin, D. B., *et al. Cancer research.* **2006,** 66, (13), 6732-6740.

148. Abbott, N. J., *et al. Nature Reviews Neuroscience.* **2006,** 7, (1), 41-53.

149. Wolburg, H., *et al. Acta neuropathologica.* **2003,** 105, (2003), 586-592.

150. Schneider, S. W., *et al. Acta Neuropathologica.* **2004,** 107, (3), 272-276.

151. Liebner, S., *et al. Acta Neuropathologica.* **2000,** 100, (3), 323-331.

152. Lockman, P. R., *et al. Drug Development and Industrial Pharmacy.* **2002,** 28, (1), 1-13.

153. Huwyler, J., *et al. Proceedings of the National Academy of Sciences.* **1996,** 96, (24), 14164-14169.

154. van Rooy, I., *et al. Journal of Controlled Release.* **2011,** 150, (1), 30-36.

155. Ko, Y. T., *et al. Journal of Controlled Release.* **2009,** 133, (3), 230-237.

156. Miura, Y., *et al. ACS Nano.* **2013,** 7, 8583-8592.

157. Zhan, C., *et al. Journal of Controlled Release.* **2010,** 143, (1), 136-142.

158. Reardon, D. A., *et al. Journal of Clinical Oncology.* **2008,** 26, (34), 5610-5617.

159. Hadjipanayis, C. G., *et al. Cancer research.* **2010,** 70, (15), 6303-6312.

160. Sampson, J. H., *et al. Molecular Cancer Therapeutics.* **2009,** 8, (10), 2773-2779.

161. Chen, X.-C., *et al. Nanotechnology.* **2008,** 19, (23), 235105-235105.

162. Guo, J., *et al. Biomaterials.* **2011,** 32, (31), 8010-8020.

163. Pearce, T. R., *et al. Advanced Materials.* **2012,** 24, (28), 3803-3822.

164. Gratton, S. E. A., *et al. Proc. Natl. Acad. Sci. USA.* **2008,** 105, (33), 11613-11618.

165. Liu, Z., *et al. Nature nanotechnology.* **2007,** 2, (1), 47-52.

166. Wang, C. H., *et al. Nanomedicine: Nanotechnology, Biology, and Medicine.* **2011,** 7, (1), 69-79.

167. Ren, J., *et al. Biomaterials.* **2012,** 33, (11), 3324-3333.

168. Rothemund, P. W. K. *Nature.* **2006,** 440, (7082), 297-302.

169. Yan, H. *Science.* **2003,** 301, (5641), 1882-1884.

170. Sellner, S., *et al. Biomaterials.* **2015,** 53, 453-463.

171. Kocabey, S., *et al. Nanomaterials.* **2015,** 5, (1), 47-60.

172. Ko, S., *et al. Biomacromolecules.* **2008,** 9, 3039-3043.

173. Hamblin, G. D., *et al. Journal of the American Chemical Society.* **2012,** 134, (6), 2888-2891.

174. Zhao, Y.-X., *et al. ACS Nano.* **2012,** 6, (10), 8684-8691.

175. Kirchhausen, T., *et al. Methods in Enzymology.* **2008,** 438, 77-93.

176. Adil, M., *et al. Langmuir : the ACS journal of surfaces and colloids.* **2014,** 30, (13), 3802-3810.

177. Bartlett, D. W., *et al. Bioconjugate Chemistry.* **2007,** 18, (2), 456-468.

178. Schluep, T., *et al. Proceedings of the National Academy of Sciences of the United States of America.* **2009,** 106, (27), 11394-11399.

179. Zagorovsky, K., *et al. Proceedings of the National Academy of Sciences.* **2016,** 113, (48), 13600-13605.

180. Emlen, W. *Journal of Experimental Medicine.* **1978,** 147, (3), 684-699.

181. Tamkovich, S. N., *et al. Annals of the New York Academy of Sciences.* **2006,** 1075, (1), 191-196.

182. Cherepanova, A. V., *et al. Annals of the New York Academy of Sciences.* **2008,** 1137, (1), 218-221.

183. Platt, N., *et al. Chemistry & Biology.* **1998,** 5, (8), R193-R203.

184. Cho, E. C., *et al. Nano Letters.* **2009,** 9, (3), 1080-1084.

185. Bujold, K. E., *et al. Chem. Sci.* **2014,** 5, (6), 2449-2455.

186. Liang, L., *et al. Angewandte Chemie - International Edition.* **2014,** 53, (30), 7745-7750.

187. Walsh, A. S., *et al. ACS Nano.* **2011,** 5, (7), 5427-5432.

188. Li, J., *et al. Biomaterials.* **2011,** 32, (21), 4943-4950.

189. Gulyaev, A. E., *et al. Pharmaceutical Research.* **1999,** 16, (10), 1564-1569.

190. Osaki, F., *et al. Journal of the American Chemical Society.* **2004,** 126, (21), 6520-6521.

191. Sykes, E. A., *et al. ACS Nano.* **2014,** 8, (6), 5696-5706.

192. Stupp, R., *et al. N Engl J Med.* **2005,** 352, 987-996.

193. Gelperina, S. E., *et al. Toxicology Letters.* **2002,** 126, (2), 131-141.

194. Steiniger, S. C. J., *et al. International Journal of Cancer.* **2004,** 109, (5), 759-767.

195. Wohlfart, S., *et al. PLoS ONE.* **2011,** 6, (5).

196. Koukourakis, M. I., *et al. British journal of cancer.* **2000,** 83, (10), 1281-1286.

197. Yang, F. Y., *et al. Journal of Controlled Release.* **2012,** 160, (3), 652-658.

198. Petersen, M. A., *et al. Bioconjugate Chemistry.* **2013,** 24, 533-543.

199. Padilla De Jesus, O. L., *et al. Bioconjugate Chemistry.* **2002,** 13, (3), 453-461.

200. Doxorubicin GBM IC50 Values. www.cancerrxgene.org/translation/Drug/133 May 30, 2018.

201. Lin, C., *et al. Biochemistry.* **2009,** 48, (8), 1663-1674.